FHWA Contract No. DTFH70-12-E-00032

Improving the Quality of Inertial Profiler Measurements at Low Speed, During Braking, and Through Stops

Submitted to:

U.S. Department of Transportation

Federal Highway Administration

Office of Acquisition and Grants Management

1200 New Jersey Avenue, SE, Room E62-204

Washington, DC 20590

Submitted by:

Steven M. Karamihas

University of Michigan Transportation Research Institute

Ann Arbor, MI

July 29, 2021

FOREWORD

The FHWA managed pooled fund study, TPF-5(063) Improving the Quality of Pavement Profile Measurement, was established to assemble State Departments of Transportation (DOTs) and the Federal Highway Administration, alongside industry and academia to meet five main goals: (1) Identify data integrity and quality issues with inertial profilers; (2) Suggest approaches to addressing identified issues and provide solutions; (3) Initiate and monitor pilot projects intended to address identified issues; (4) Disseminate results; and (5) Assist in the deployment of research findings and recommendations. TPF-5(063) participants identified a need to improve the quality of pavement profile measurement at low speed, during braking, and at stops. This report presents the results of a study designed to address that need. The project was conducted simultaneous to the NCHRP 10-93 project "*Measuring, Characterizing, and Reporting Pavement Roughness of Low-Speed and Urban Roads,*" which resulted in the NCHRP Report 914. The main goal of that report is to provide successful practices for DOTs and industry to implement in collecting quality ride data on low volume and urban roads that result in increased data accuracy, precision, and reliability while maintaining a cost-effective data collection process. This report will be useful for agencies, industry, and personnel involved in network-level pavement surface condition data collection and analysis.

Shay Burrows, Director,

FHWA Resource Center

Technical Report Documentation Page

1. Report No. FHWA-RC-21-0001	2. Government Accession No.	3. Recipient's Catalog No.	
4. Title and Subtitle Improving the Quality of Inertial Profiler Measurements at Low Speed, During Braking, and Through Stops		5. Report Date April 2020	
		6. Performing Organization Code	
7. Author(s) Karamihas, Steven M. (ORCID: 0000-0002-7480-3952)		8. Performing Organization Report No.	
9. Performing Organization Name and Address University of Michigan Transportation Research Institute 2901 Baxter Rd. Ann Arbor MI 48109		10. Work Unit No. (TRAIS)	
		11. Contract or Grant No. DTFH70-12-E-00032	
12. Sponsoring Agency Name and Address Western Federal Lands Highway Division Federal Highway Administration 610 East 5th Street Vancouver, WA 98661		13. Type of Report and Period Covered July 2012-October 2019	
		14. Sponsoring Agency Code	
15. Supplementary Notes The FHWA Contracting Officer's Technical Representative (COTR) was Megan Chatfield.			

16. Abstract

Inertial profilers can produce valid measurements of longitudinal road profile when they are operated under favorable conditions. However, their performance deteriorates when the host vehicle travels at low speed, decelerates, or comes to a stop. These limitations have hindered the application of inertial profilers for measurement of roughness on low-speed roadways and within urban road networks.

This research developed and tested short-term and long-term solutions for addressing errors in profile measurement caused by adverse operational conditions. The proposed short-term solution combines custom numerical procedures with standard filtering techniques to reduce errors in profile measured during stops using only the nominal set of sensors found on a production inertial profiler.

The long-term solution augments the nominal inertial profiler design with additional sensors to eliminate errors caused by accelerometer misalignment and bias. The augmented system includes body-fixed measurement of profiler acceleration and rotation rate in three dimensions. The system also includes GPS measurement of profiler host vehicle height, vertical velocity, pitch inclination, and roll inclination. A multi-rate extended Kalman filter with smoothing combines the inertial sensors with the GPS outputs to eliminate drift and alignment errors.

17. Key Word Road roughness, Longitudinal profile, International Roughness Index, Inertial profilers, Kalman filter		18. Distribution Statement No restrictions. This document is available to the public through the National Technical Information Service, Springfield, VA22161. http://www.ntis.gov	
19. Security Classif. (of this report) Unclassified	20. Security Classif. (of this page) Unclassified	21. No. of Pages 153	22. Price N/A

Form DOT F 1700.7 (8-72)   Reproduction of completed page authorized

SI* (MODERN METRIC) CONVERSION FACTORS

APPROXIMATE CONVERSIONS TO SI UNITS

Symbol	When You Know	Multiply By	To Find	Symbol
LENGTH				
in	inches	25.4	millimeters	mm
ft	feet	0.305	meters	m
yd	yards	0.914	meters	m
mi	miles	1.61	kilometers	km
AREA				
in^2	square inches	645.2	square millimeters	mm^2
ft^2	square feet	0.093	square meters	m^2
yd^2	square yard	0.836	square meters	m^2
ac	acres	0.405	hectares	ha
mi^2	square miles	2.59	square kilometers	km^2
VOLUME				
fl oz	fluid ounces	29.57	milliliters	mL
qal	gallons	3.785	liters	L
ft^3	cubic feet	0.028	cubic meters	m^3
yd^3	cubic yards	0.765	cubic meters	m^3
NOTE: volumes greater than 1000 L shall be shown in m^3				
MASS				
oz	ounces	28.35	grams	g
lb	pounds	0.454	kilograms	kg
T	short tons (2000 lb)	0.907	megagrams (or "metric ton")	Mg (or "t")
TEMPERATURE (exact degrees)				
°F	Fahrenheit	5 (F-32)/9 or (F-32)/1.8	Celsius	°C
ILLUMINATION				
fc	foot-candles	10.76	lux	lx
fl	foot-Lamberts	3.426	candela/m^2	cd/m^2
FORCE and PRESSURE or STRESS				
lbf	poundforce	4.45	newtons	N
lbf/in^2	poundforce per square inch	6.89	kilopascals	kPa

APPROXIMATE CONVERSIONS FROM SI UNITS

Symbol	When You Know	Multiply By	To Find	Symbol
LENGTH				
mm	millimeters	0.039	inches	in
m	meters	3.28	feet	ft
m	meters	1.09	yards	yd
km	kilometers	0.621	miles	mi
AREA				
mm^2	square millimeters	0.0016	square inches	in^2
m^2	square meters	10.764	square feet	ft^2
m^2	square meters	1.195	square yards	yd^2
ha	hectares	2.47	acres	ac
km^2	square kilometers	0.386	square miles	mi^2
VOLUME				
mL	milliliters	0.034	fluid ounces	fl oz
L	liters	0.264	gallons	gal
m^3	cubic meters	35.314	cubic feet	ft^3
m^3	cubic meters	1.307	cubic yards	yd^3
MASS				
g	grams	0.035	ounces	oz
kg	kilograms	2.202	pounds	lb
Mg (or "t")	megagrams (or "metric ton")	1.103	short tons (2000 lb)	T
TEMPERATURE (exact degrees)				
°C	Celsius	1.8C+32	Fahrenheit	°F
ILLUMINATION				
lx	lux	0.0929	foot-candles	fc
cd/m^2	candela/m^2	0.2919	foot-Lamberts	fl
FORCE and PRESSURE or STRESS				
N	newtons	0.225	poundforce	lbf
kPa	kilopascals	0.145	poundforce per square inch	lbf/in^2

* SI is the symbol for the International System of Units. Appropriate rounding should be made to comply with Section 4 of ASTM E380.

(Revised March 2003)

TABLE OF CONTENTS

LIST OF FIGURES

LIST OF TABLES

LIST OF ABBREVIATIONS

AASHTO   American Association of State Highway and Transportation Officials

CAN   Controller Area Network

CPU   Central Processing Unit

DAS   Data Acquisition System

DOF   Degree of Freedom

DOT   Department of Transportation

FHWA   Federal Highway Administration

FLHP   Federal Lands Highway Program

GCARS   Golden-Car Average Rectified Slope

GM   General Motors

GPS   Global Positioning System

HPF   High Pass Filter

HPMS   Highway Performance Monitoring System

IIR   Infinite Impulse Response

IMU   Inertial Measurement Unit

INS   Inertial Navigation System

IRI   International Roughness Index

ISO   International Organization for Standardization

LPF   Low Pass Filter

MAP-21   Moving Ahead for Progress in the 21st Century

NHS   National Highway System

PI   Proportional Integral

PSD   Power Spectral Density

PTRN   Pre-Transform Ride Number

RMS   Root Mean Square

RN   Ride Number

RTCM   Radio Technical Commission for Maritime

RTK   Real Time Kinematic

RTS   Rauch-Tung-Striebel

SAE   Society of Automotive Engineers

TPM   Transportation Performance Management

NOTATION

α	exponential constant for adaptive filtering
β	sharpness coefficient
γ	cross correlation amplitude adjustment
δ	slowly time-varying bias
θ_{gps}	GPS pitch inclination
λ	wavelength, longitude
λ_{-3dB}	wavelength for 3 dB reduction in cascaded filter
λ_0	reference longitude
λ_c	cut-off wavelength
μ	Golden-Car Model normalized unsprung mass
μ_p	mean value for filtered profile p
ν	wave number
ν_0	reference wave number
ρ_{pq}	normalized cross correlation for profiles p and q
σ	standard deviation
σ_A	Allan deviation
τ	time constant
ϕ	latitude
ϕ_0	reference latitude
ϕ_{gps}	GPS roll inclination
ψ	heading angle change
ω	angular frequency
ω_a	analog (angular) cut-off frequency
ω_n	angular natural frequency
Δt	time interval
Δt_0	reference (maximum) time interval
Δt_{Adj}	adjusted time interval
Δx	distance interval
Ω	raw sensor output for Allan variance analysis
$\bar{\Omega}$	cluster average for Allan variance analysis
c_r	rotational damping

d	disturbance signal
dE	movement eastward
dF	displacement forward
dL	displacement leftward
dN	movement northward
e	error signal
f_{-3dB}	frequency for 3 dB reduction in cascaded filter
f_c	cut-off frequency
f_{ls}	low-speed cut-off frequency
h_{rc}	rotation center height
h_p	profiler height relative to the rotation center
k	sample number
k_r	rotational stiffness
l_p	profiler longitudinal position relative to the rotation center
l_y	GPS antenna lateral offset
l_z	GPS antenna vertical offset
m	mass
p,q	profiles stored at a constant distance interval
t	time
t_s	start time
v_0	reference speed
v_{set}	PI controller set speed
w	road elevation spectral model exponent
x_{off}	distance offset
B	moving average base length
B_A	bias instability
C	Golden-Car Model normalized suspension damping
D	denominator
$G(v)$	road elevation spectrum
$G'(v)$	road slope spectrum
G_0	reference road spectrum elevation coefficient
G_a	road spectrum spatial acceleration coefficient
G_e	road spectrum elevation coefficient
G_s	road spectrum slope coefficient

$H(v)$	transfer function for spatial frequency
$H(s)$	transfer function, s domain
H_0	reference height above sea level
K_1	Golden-Car Model normalized tire stiffness
K_2	Golden-Car Model normalized suspension stiffness
K_A	rate random walk
K_I	integral gain
K_P	proportional gain
L	pavement section length
L_{cm}	center of mass height in relation to the rotation center
N	number of samples
N_A	angle random walk
Q_A	quantization
$R(\phi_0)$	Earth radius at the reference latitude
R_A	ramp instability
R_{pq}	cross correlation for profiles p and q
S	spectral density function
T	duration, total time
V	Golden-Car Model forward speed

KINEMATICS

Superscripts on scalar and vector quantities denote the reference frame.

θ	Euler pitch angle
ϕ	Euler roll angle
ψ	Euler yaw angle
$\vec{\omega}_{a/b}$	angular rate vector, frame a relative to frame b
ω_x	angular rate about the longitudinal axis
ω_y	angular rate about the lateral axis
ω_z	angular rate about the vertical axis
$\mathbf{\Omega}_{b/n}$	skew symmetric matrix corresponding to the angular rate vector
$\vec{a}_{a/b}$	acceleration vector, frame a relative to frame b
$\vec{a}_p$	acceleration vector, profiler reference point
a_{xp}	profiler reference point longitudinal acceleration
a_{yp}	profiler reference point lateral acceleration

a_{zp}, a_{zref}	profiler reference point longitudinal acceleration
a_{xpeak}	peak longitudinal acceleration
$\vec{f}$	specific force vector, expressed in frame a
f_z	specific force vertical component
$\vec{g}^a$	gravity vector, expressed in frame a
g	acceleration due to gravity
h	height sensor reading
$\vec{p}_{a/b}$	profiler reference point position, frame a relative to frame b
$\vec{r}_{a/b}$	position vector, point a relative to point b
r_{xp}	profiler reference point longitudinal position
r_{zp}, r_{zref}	profiler reference point vertical position
r_{zr}, r_{zroad}	road surface vertical position
$\vec{v}_{a/b}$	velocity vector, point a relative to point b
v_h	horizontal speed
v_x, v_{xp}	profiler reference point longitudinal speed
v_{zp}	profiler reference point vertical speed
x	longitudinal distance
C^{nb}	direction cosine matrix, frame b to frame n
C_{ij}^{nb}	direction cosine matrix element, row i, column j, frame b to frame n

KALMAN FILTERING NOTATION

k	time step
nm	number of measurements
ni	number of inputs
nn	number of process noise terms
ns	number of state variables
u_k	input vector
v_k	measurement noise vector
w_k	process noise vector
x_k	state vector
$\hat{x}_{j|k}$	state estimate at time step j, given information up to time step k
y_k	measurement vector
A_k	state transition matrix, linearized state transition matrix
B_k	input matrix

H_k	observation matrix, linearized observation matrix
I	identity matrix
K_k	Kalman gain matrix
L_k	RTS fixed-interval smoother blending matrix
N	number of time steps
$P_{j/k}$	state covariance estimate at time step j, given information up to time step k
Q_k	process noise covariance matrix
R_k	measurement noise covariance matrix
V_k	linearized measurement noise matrix
W_k	linearized process noise matrix

CHAPTER 1. INTRODUCTION

MOTIVATION

Federal, State, and local transportation agencies collectively manage a network of roads that represents a huge public investment. The U.S. public road system comprises more than 4 million centerline miles of road, which supported 3 trillion vehicle-miles of travel in 2019.[1] In 2018, Federal, State, and local highway funding was $235.0 billion, and it has exceeded $190 billion each year since 2010.[1,2]

Most State and Federal highway agencies use pavement roughness as a measure of the quality of roads. Roughness measurements are used to monitor the ride quality of their road networks, prioritize pavement rehabilitation and reconstruction projects, and to select pavement preservation strategies.[3] Many agencies also use roughness measurements for construction quality control and assurance, and adjust the value of paving contracts based on the roughness of the finished surface.[4] In addition, the Federal Highway Administration (FHWA) Highway Performance Monitoring System (HPMS) requires States to submit roughness data for a large portion of their Federal aid highway network, including the National Highway System (NHS).[5] In turn, these data influence the allocation of billions of dollars in Federal funding for roads through the FHWA's Highway Economic Requirements System.[6,7]

Roughness is not measured directly for these applications. Instead, the roughness of a particular segment of road is calculated from a measurement of longitudinal elevation profile.[8] Longitudinal elevation profile is a record of road surface elevation relative to an arbitrary datum, which is stored as a function of distance along the pavement. Hereafter, longitudinal elevation profile is referred to as *profile*. By far, the most common scale for quantifying the roughness of a profile is the International Roughness Index (IRI), and the most common device for measuring profile is the inertial profiler.[3,9,10]

A greater emphasis on the quality of pavement roughness measurements has been provoked recently by the enactment of the Moving Ahead for Progress in the 21st Century (MAP-21), Public Law 112-141 (2012). The Act requires an asset management plan for the entire NHS, and requires states to meet minimum standards for pavement performance or lose flexibility in the use of their Federal highway funds.[11,12] The IRI was selected as a "tier 1" measurement of pavement condition, and, therefore, was immediately implemented as the primary indicator of pavement performance.[10,13] States are now required to report the IRI on an expanded NHS network under the National Highway Performance Program.[5]

Under ideal conditions, inertial profilers have demonstrated the capability to measure profile with sufficient accuracy and repeatability for the engineering applications described above. However, horizontal acceleration of the profiler host vehicle combined with changes in its orientation introduces artificial roughness into measured profiles.[14] This occurs when profilers operate on curves, or when safe piloting of the profiler host vehicle requires rapid changes in speed or stop-and-go driving.[15]

Urban pavements pose a particular challenge to inertial profilers, because they include signal lights, stop signs, railroad crossings, and heavy traffic. Obtaining valid measurement of roughness in urban areas is particularly important, since MAP-21 expanded the 164,000-mile NHS by more than 60,000 miles, and most of the newly designated roads are in urban areas.[16] Further, more than two-thirds of the 3-trillion vehicle miles traveled on the U.S. road system in 2018 occurred on urban roadways.[17]

Many low-speed rural roads also pose a challenge to inertial profilers. For example, the Federal Lands Highway Program (FLHP) includes 172,000 miles of road built within parks, forests, wildlife refuges, Indian reservations, and other locations with difficult terrain.[18] The FHWA's design guidance for roads built under the FLHP calls for "context sensitive" road design, which requires respect for the land, preservation of wildlife, and minimization of the effect of the road system on existing features.[19] As such, these roads often include tight horizontal curves and aggressive grade changes.

This research will systematically define the limitations of current inertial profiling technology and develop and validate improvements to the technology needed for obtaining valid profile measurements that are not sensitive to horizontal acceleration or pitch and roll of the profiler host vehicle. Since several hundred, and possibly more than one thousand, inertial profilers are already in service in the United States for measurement of profile and road roughness, the technology improvements should be cost effective and augment the design of conventional inertial profilers.

PROBLEM DESCRIPTION

Background

The inertial profiler was invented in the early 1960s at the General Motors (GM) Corporation. A research laboratory within GM created the "Profilometer," shown in figure 1, to measure road profiles with "reasonable flexibility and speed" for use as realistic vertical disturbance inputs to vehicles on a driving simulator.[20,21] Previous devices that measured road roughness efficiently produced output based on measurement of vehicle response or relative measurements from the device chassis to the road.[22] These devices did not offer a flat frequency response to the true profile.[23] Engineers interested in undistorted profiles obtained them using high-precision rod and level surveys, because the level provides a consistent reference from which to measure the relative elevation of the road.[24–26] However, the measurement process was "very time consuming and requires painstaking care."[22]
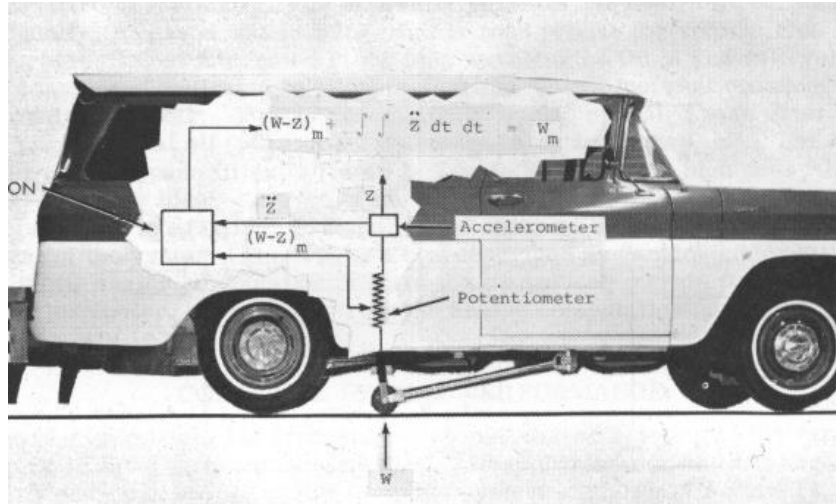
Figure 1. Schematic. GM Research Road Profilometer.[a][27]

Shortly after GM introduced the first inertial profiler to the pavement community, the Bureau of Public Roads initiated a research project with the Michigan Department of Transportation (DOT) to duplicate the GM design and evaluate the technology for measurement of "bridge and pavement roughness."[28] In parallel, a number of state DOTs began to evaluate the technology and adapt it for pavement management applications.[29–32] Early study showed that inertial profilers could efficiently reproduce profiles measured by high-precision rod and level surveys over a broad waveband, although they could not detect road grade or gradual grade changes.[27,28] Users did not find the measurement principle of inertial profilers intuitive, and the need to cover large road networks safely and efficiently challenged inertial profilers' ability to establish a valid inertial reference with difficult operational conditions.[33] Nevertheless, the relative efficiency of inertial profilers and their ability to reproduce the true profile over a broad waveband under favorable operational conditions led to their widespread use for monitoring road roughness.

Measurement Principle

Inertial profiles measure the elevation of the road surface along a given wheel path (or multiple wheel paths) as a function of longitudinal distance. To do so, they combine the same three ingredients that make up a profile measured by a surveyor's rod and level: (1) a reference elevation, (2) the height of the road relative to the reference elevation, and (3) a measure of longitudinal distance.[34] Figure 2 illustrates this measurement concept for a rod and level. The level establishes a constant reference elevation (r_{zref}). At each location along a given segment of road, the reading on the rod ($r_{zref} - r_{zroad}$) indicates the vertical distance to the road beneath the reference elevation. Longitudinal distance is measured independently, often with a graduated steel tape. When profile is measured for analysis of pavement roughness, both elevation and distance (x) are reported relative to an arbitrary origin, although the final profile is often offset vertically and horizontally to place the origin at the start of a road section of interest.

---

[a] From Spangler, E. B., and W. J. Kelly. GMR Road Profilometer–A Method for Measuring Road Profile. *Highway Research Record*, No. 121, 1966, Figure 12, p. 32. Copyright, National Academy of Sciences. Reproduced with permission of the Transportation Research Board.
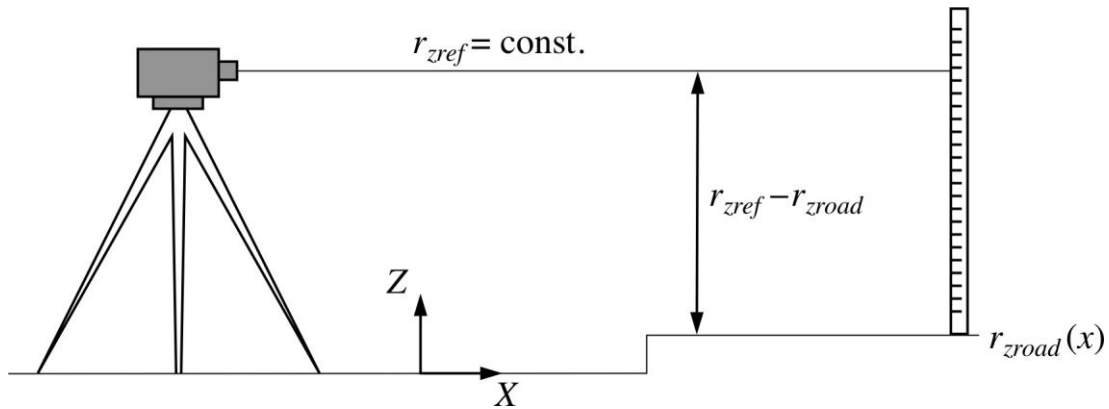
Figure 2. Schematic. Measurement of profile with a surveyor's rod and level.

The purpose of inertial profilers is to efficiently record profile, and they are often mounted to conventional over-the-road vehicles to facilitate safe operation in live traffic. An inertial profiler records the elevation of a reference point on a host-vehicle chassis and the height of the road surface relative to the reference point as the vehicle passes over a road section of interest. The profile is calculated as shown in figure 3.

$$r_{zroad}(x) = r_{zref}(x) - \left(r_{zref}(x) - r_{zroad}(x) \right)$$

Figure 3. Equation. Measurement of profile with a surveyor's rod and level.

Figure 4 illustrates the principle of operation for an inertial profiler with sensors mounted to a reference point forward of the front bumper of a vehicle. Unlike the rod and level, the elevation of the reference point fluctuates as the profiler host vehicle responds to the roughness of the road and to other disturbances. A vertically oriented accelerometer, mounted to the profiler's reference point, provides a record of its motion. Integrating twice produces a record of $r_{zref}(x)$. This "accelerometer-established inertial reference" is often called a *floating-reference-height* signal.[35]
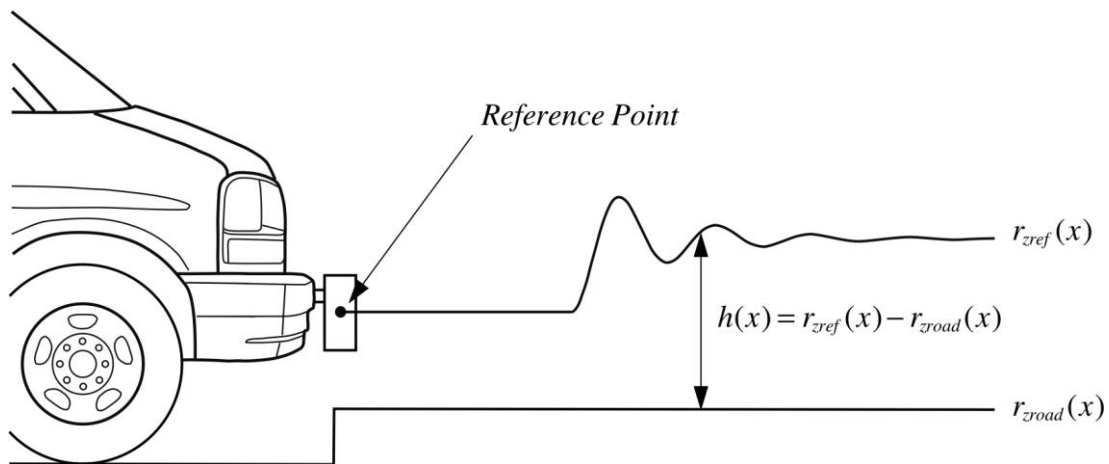
Figure 4. Schematic. Inertial measurement of longitudinal profile (after Huft).[36]

4

A ranging sensor, often called a *height sensor* in this context, provides the relative measurement $r_{zref}(x) - r_{zroad}(x)$ to the road surface. Unlike the original GM design shown in figure 1, which used a potentiometer connected to a road follower wheel, most inertial profilers sense the vertical distance from the (floating) profiler reference point to the road surface using laser triangulation sensors.

In some implementations the calculation of road profile is performed in the time domain, as shown if figure 5. In the figure, $a_{zref}(t)$ and $h(t)$ are the signals from the accelerometer and height sensor, respectively. The temporal profile is resolved to a spatial profile in a subsequent processing step using an independent measurement of distance versus time. In other implementations the sensor signals are digitized with a constant longitudinal spacing, or resolved to the spatial domain before the profile is calculated, as shown in figure 6.[37,38] In figure 6, v_x is the longitudinal speed of the host vehicle. The term in the integrand is the spatial vertical acceleration of the reference point.

$$r_{zroad}(t) = \iint a_{zref}(t)\,dt\,dt - h(t)$$

Figure 5. Equation. Temporal profile calculation.

$$r_{zroad}(x) = \iint \left(a_{zref}(x)/v_x^2\right)dx\,dx - h(x)$$

Figure 6. Equation. Spatial profile calculation.

Figure 7 presents a block diagram used to explain the principle of operation of the first inertial profiler.[27] The figure illustrates the signal flow from the actual profile, W (i.e., $r_{zroad}(x)$ in figure 4), to the measured profile. The figure also provides straight-line approximations of the temporal frequency content at each stage of the process for a simple model of the profiler host vehicle described as a mechanical filter with a "natural frequency of ω_n", and idealized sensor and filter performance.
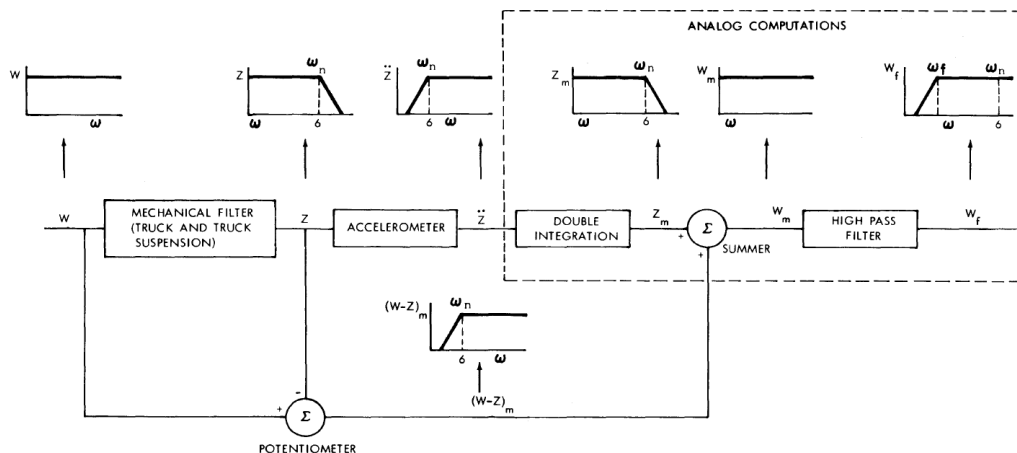
Figure 7. Block diagram. Inertial profiler signal flow.[b(27)]

As shown in figure 7, the profile serves as the excitation to the host vehicle. The time history of vertical position of the profiler reference point (r_{zref}) is determined by the dynamic response of the profiler host vehicle. The response is detected by a vertically oriented accelerometer, and the vertical position of the profiler reference point is recovered by integrating the accelerometer output twice. The height sensor, which is shown as the "potentiometer" in the figure, provides the vertical distance from the profiler reference point to the road. In theory, the profile is reproduced when the two signals are combined. In early profilers, a high-pass filter was applied to the measured profile to avoid exceeding the voltage capacity of the analog components.

Although figure 7 illustrates the measurement principle used by inertial profilers, it omits several details that are relevant to this research. For example, the functions enclosed within the box marked "analog computations" are performed digitally in most modern inertial profilers, and filtering is performed at multiple stages in the measurement process. In addition, the frequency content of the vehicle response is much more complex, and the frequency response of the height-sensor and accelerometer signal overlap. Chapter 2 examines these issues using field measurements.

Measurement Errors

Two mechanisms cause errors in the measurement of the floating-reference-height signal. These impose a limitation on the measurement of the very long-wavelength (i.e., low-frequency) portion of the profile. The first is system noise. At progressively lower frequencies, the actual vertical acceleration diminishes in relation to noise in the instrumentation and the resolution of the system.[39] Although grade changes and long-wavelength roughness typically correspond to large changes in elevation, their contribution to the vertical acceleration measured on a profiler host vehicle is very small relative to other disturbances.

Second, offsets caused by tilt of the accelerometer from true vertical and other sources of drift appear in the output signal.[20,31,36] In typical inertial profilers the accelerometers are rigidly mounted to the host-vehicle sprung mass. A combination of road grade, cross slope, imprecise mounting, and quasi-static inconsistency in vehicle attitude all cause accelerometer misalignment. When the error in the accelerometer readings is nearly constant over a long time interval, the error in the floating reference height after double integration grows in proportion to the square of time.[36]

Early inertial profilers applied analog high-pass filters to the accelerometer signals, in part to eliminate the waveband that was contaminated by these two error sources.[28,29] High-pass filtering also limited the output of profilers to the waveband of interest for vehicle dynamic response. In modern implementations profilers apply high-pass filtering with a specific spatial frequency response in mind, and the most common cut-off corresponds to a wavelength of 300 ft.[40] The 300-foot wavelength limit is a vestige from an early stage in the history of inertial profiler development, "which at 100-mph car velocity produce(s) input frequencies to the car below the natural frequencies of all current road vehicle suspensions." [20] Use of the 300-foot cut-off value has prevailed as a standard, since at practical travel speeds it retains content that affects ride comfort, suspension stroke, and dynamic tire load fluctuations. For typical combinations of road grade, cross slope, road roughness level, profiler host-vehicle properties, and host-vehicle speed, the high-pass filter eliminates the content that is contaminated by low

6

signal strength in the accelerometer and slowly fluctuating or constant accelerometer misalignment.

Some accelerometer misalignment occurs because of excessive rigid-body motion of the host-vehicle sprung mass (i.e., pitch and roll response to roughness) and errors caused by operator-induced disturbances (e.g., braking, steering corrections for lane keeping). These alignment errors are a serious source of drift for two reasons. First, since inertial profilers used for pavement management must operate in live traffic, they experience the road at speeds near the prevailing traffic speed. Therefore, misalignment errors caused by profiler host-vehicle dynamic responses map to the same range of wavelengths in the measured profile that affect the IRI. Second, the dynamic component of accelerometer tilt typically occurs in response to, or at least in conjunction with, horizontal acceleration that further contaminates the accelerometer readings.

Sayers and Karamihas described errors in accelerometer readings caused by braking, and Karamihas et al. expanded the discussion to include lateral acceleration and demonstrated the problem experimentally.[14,34] The discussions are summarized here using an example in the pitch plane. Figure 8 shows the side view of an accelerometer that is tilted due to braking. In the figure, the Z_w axis is aligned with gravity, and the X_w axis is perpendicular to gravity and parallel to the longitudinal plane of symmetry of the profiler host vehicle. These axes exist within a frame of reference called the *wander frame*. (See Chapter 6.)
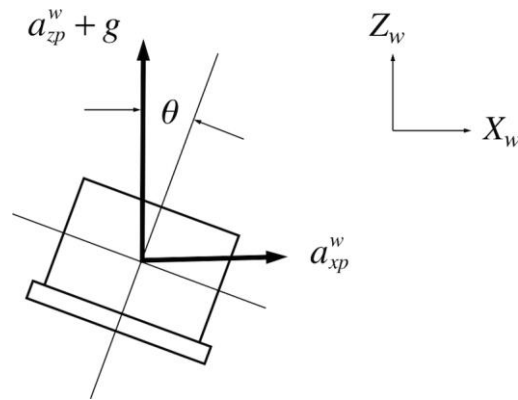
Figure 8. Schematic. Accelerometer tilted due to braking.

In this example, the accelerometer is "servo" type, and it reads vertical acceleration equal to 1 g when it is at rest. Typically, the 1 g offset is removed. As such, an ideal sensor would read a_{zp}^w, which is the vertical acceleration of the profiler reference point in the direction aligned with gravity. Figure 9 provides an expression for the reading obtained by the misaligned accelerometer, which is fixed in the vehicle body.

$$a_{zp}^b = a_{xp}^w \sin(\theta) + \left(a_{zp}^w + g\right)\cos(\theta) - g$$

Figure 9. Equation. Expression for body-fixed vertical acceleration.

In figure 9, g is the acceleration due to gravity, a_{xp}^w is the longitudinal acceleration (negative for braking), and θ is the pitch angle. The pitch angle defines the misalignment of the sensitive axis

of the accelerometer compared to true vertical. Figure 10 shows the expression for the error in the accelerometer reading.

$$a_{zp}^b - a_{zp}^w = a_{xp}^w \sin(\theta) + \left(a_{zp}^w + g\right)\left(\cos(\theta) - 1\right)$$

Figure 10. Equation. Expression for error in vertical acceleration.

Note that the projection of vertical acceleration onto the sensitive axis of the accelerometer (the second term) causes an error in proportion to $\cos(\theta) - 1$. This term grows very slowly with misalignment. In contrast, the projection of horizontal acceleration onto the sensitive axis of the accelerometer (the first term) grows in proportion to longitudinal acceleration magnitude and in approximate proportion to misalignment angle θ for practical situations. Since θ itself increases with longitudinal acceleration, this term is very sensitive.

The analysis by Karamihas et al. addressed accelerometer misalignment in pitch due to braking and accelerometer roll due to lateral acceleration.[14] However, it did not address higher-frequency variations in accelerometer misalignment and horizontal acceleration caused by road disturbances. In addition, the literature has not offered an analysis of the kinematics presented in figure 9 and figure 10 in light of dynamic vehicle response. That is, the effect of misalignment on profile depends on the time history of vertical and horizontal acceleration experienced by the system, the profiler host vehicle's misalignment in response to it (and the associated lag), and the manner in which the "error" signal maps to profile. This is addressed in Chapter 2.

LITERATURE REVIEW

The existing literature offers several options with the potential to reduce or eliminate the influence of host-vehicle misalignment on road profiles measured in live traffic. These fall into four categories:

1. Suppression of measurement errors in inertial profile computation and processing algorithms.

2. Augmentation of inertial profiler sensors with additional measurements, such as host-vehicle attitude.

3. Estimation of road profile from vehicle response measurements.

4. Measurement of profile without the use of an accelerometer-established floating reference.

This section presents a brief review of published work on each approach.

Error Suppression

Walker and Becker developed a method of suppressing profile measurement errors that occur when a profiler host vehicle slows below a given speed or comes to a complete stop.[15] When the speed is sufficiently low, the profile calculation algorithm is modified in two ways. First, the apparent progression of time is reduced over the interval of low-speed operation so that the

double-integrated accelerometer signal grows less rapidly. Second, the change in elevation between readings in the computed profile is limited to a preset value. This method did not completely eliminate profile measurement errors observed in areas of low-speed operation and stops, but it greatly reduced the severity of the artificial roughness that is typically observed.

Gagarin et al. studied operational conditions that affect the accelerometer-established floating reference height for inertial profilers, including alignment errors, cross-axis contamination by horizontal acceleration, and frequency response.[41] The research simulated errors in measured profile and roughness on roads with horizontal and vertical curvature using CarSim, and developed estimates of the expected error in IRI associated with various combinations of travel speed, horizontal road curvature, and vertical road curvature.

Sensor Augmentation

Direct correction of accelerometer alignment errors requires measurement of host-vehicle orientation and off-axis acceleration. Dembski et al. presented kinematic equations for errors to inertial profiler readings caused by pitch and roll in a description of a terrain severity measurement system.[42,43] The system was implemented using a gyroscopically enhanced rate sensor for measurement of orientation. Demić et al. presented the kinematic equations for a system that uses two body-mounted tri-axial accelerometers for indirect measurement of the change in body pitch, roll, and yaw on a trailer that would house an inertial profiler.[44] Gagarin et al. proposed the use of tri-axial accelerometers and gyroscopes for measurement of true vertical acceleration.[41] Past developers of inertial profiling systems have also suggested the use of gyroscopic stabilization to help avoid host-vehicle alignment errors, although the associated cost prevented the implementation of such a system.[31,45,46] In an effort to improve the low-frequency performance of inertial profilers by modulation, Pong mounted four accelerometers to a disk that rotated in the roll plane.[46]

Kern and Ferris and Wagner et al. incorporated an inertial measurement unit (IMU) and global positioning system (GPS) receiver into a road and terrain measurement system.[47,48] This system used Kalman filtering to estimate host-vehicle position and orientation from GPS and IMU signal, and fused the vehicle position estimate with the floating reference height from the inertial profiler using a weighted average. Liu et al. replaced the inertial reference in the system described by Dembski with an IMU and GPS receiver for estimation of host-vehicle position via Kalman filtering.[49] Liu et al. also demonstrated a "Kalman smoother", which post-processed the signals and considered readings collected fore and aft of a position of interest.[49] This improved the kinematic estimates and eliminated discontinuities.

Collectively, these references suggest that combining inertial and GPS measurement of profiler host-vehicle kinematics has the potential to improve the measurement of profile on paved roads.

Estimation Using Vehicle Response

Several authors have presented indirect methods of profile measurement by observing or estimating road profile from measured vehicle responses using linear models of vehicle vertical vibration response.

Qin et al. presented the transfer function for calculating the power spectral density (PSD) function for a road profile from the PSD function for unsprung-mass vertical acceleration using a linear quarter car model.[50] Wang et al. proposed calculation of road profile spectral density using the signal from a dynamic tire pressure sensor and linear transfer functions.[51] The method assumed a proportional relationship between tire vertical deflection and tire pressure, and the transfer function between tire pressure and axle acceleration was measured empirically. Outputs from an embodiment of the system were provided for various types of localized roughness. Tomiyama et al. back-calculated road profile from a linear quarter-car model using measured sprung-mass and unsprung-mass vertical acceleration.[52] The velocity and position associated with each degree of freedom were obtained by integrating the measured acceleration signals.

Nguyen used a Luenberger observer with a linear quarter-car model to infer the floating-reference-height signal from the signal provided by the height sensor.[53] Vehicle parameters were obtained with system identification using impulse response and step response tests, and observer parameters were obtained with system identification using testing on roads with known profile. Harris et al. presented the theoretical development and simulated examples for inferring road profiles from vertical accelerations measured above and below the suspensions on both sides at a given axle position.[54] The method proposed combinatorial optimization for obtaining parameters for a 4-degree-of-freedom (DOF) half-car model using measurements collected on roads with known profiles, and the same modeling framework to subsequently estimate profile on roads with unknown profiles in turn.

Yousefzadeh et al. and Solhmirzaei et al. presented methods of training neural networks for estimation of profiles using detailed vehicle dynamics models that were exercised over synthetic profiles.[55,56] The neural network used seven inputs, including vertical accelerations at each wheel, and "roll, bounce, and pitch" of the sprung mass. The results did not show sufficient promise for road monitoring applications. First, significant effort was required to populate the underlying vehicle model (ADAMS/CAR) with parameter values and tune its response using hydraulic shaker testing. Second, the demonstration produced correlation to the reference profile measurement in the range from 0.8 to 0.95 for the waveband from 3 ft to 30 ft, which is below the requirements for valid measurement of IRI and addresses only part of waveband of interest.

Imine et al. and Rabhi et al. offer multiple publications that describe the use of sliding mode observers for estimation of road profile.[57–63] The core vehicle model ranges from a 4 DOF roll plane model of a single axle position to a full three-dimensional vehicle model with longitudinal dynamics. In these publications road profile and other signals of interest are estimated based on measurements of sprung-mass vertical motion and axle relative vertical motion. The sensors used to obtain those signals are not specified. These publications present measured and observed cross plots of profile elevation versus travel distance. The plots demonstrate "fair agreement with local discrepancies." [58] These plots do not provide an objective basis for evaluation. Subjectively, they do not appear to meet the accuracy requirements for road-monitoring applications.

Rath et al. presented a simulation study of road profile and friction estimation in support of longitudinal control (anti-lock braking, traction control, etc.) and active suspension systems.[64] The mode at the core of the method combined a non-linear quarter car with a model of vehicle longitudinal dynamics. The quarter-car model included non-linear suspension elements; and the

longitudinal dynamics model included tire rolling losses, aerodynamic drag, tire-road friction, wheel spin dynamics, and driveline dynamics.

Non-Inertial Systems

Only one type of device used in practice for network pavement evaluation directly measures profile without an inertial reference and operates in live traffic. This is based on a concept proposed by Still and Jordan, in which several ranging sensors are mounted to a longitudinal beam that is mounted to a host vehicle or trailer.[65] The device used a 16.4-foot-long beam and four sensors. Relative to the leading sensor, the remaining three were 0.35 ft, 7.02 ft, and 14.04 ft rearward. In this system, sensor pairs provide measurements of slope relative to reference beam. For reference, the height and orientation of the beam is derived by dead reckoning.

The irregular spacing of the sensors was needed to increase the waveband of the final profile. Still presented results that showed reproduction of a survey profile in the wavelength range from 1.6 ft to 1280 ft. However, the existing commercial embodiment of this device uses modern ranging sensors and a different geometric layout. Yi and Rong-Gui presented the theoretical development of a similar system with five sensors.[66]

Assessment

The methods for obtaining profile reviewed here are very diverse, and many originate with terrain measurement or vehicle dynamic evaluation and control as the intended application. As such, the relative accuracy of each method or device is not presented in a way that addresses the specific requirements of road profiling for pavement evaluation. Chapter 2 addresses this issue.

A majority of the estimation approaches described in the literature have only been developed theoretically or tested using computer simulations. In addition, while many of them reproduce a portion of the profile spectrum or the visible content in a raw elevation trace, it is not clear whether the details of the profile are sufficiently captured to support the needs of the pavement community. Further, only two of the estimation methods addressed system performance during horizontal acceleration.

This research emphasizes sensor augmentation and improvements to profile computation algorithms. This approach was selected for two reasons: (1) the potential for application of the results to in-service profilers, given the large investment made in the existing fleet used for pavement evaluation in the U.S.; and (2) the potential to support other functions in pavement monitoring, such as the measurement of transverse profile, grade, and cross slope.

PROBLEM DEFINITION

Inertial profilers have demonstrated reproduction of the true longitudinal road elevation profile in the waveband of interest for vehicle dynamic response (i.e., roughness) when they are operated under favorable conditions. However, they are limited in their ability to measure aspects of the profile related to roughness when the host vehicle accelerates longitudinally, accelerates laterally, or comes to a stop. These weaknesses have hindered the application of inertial profilers on urban road networks and on ramps and other roads with aggressive changes in horizontal and

vertical alignment. This research developed and tested inertial profiler design modifications that address errors in profile measurement caused by adverse operational conditions.

This research investigated data processing algorithms that suppress measurement errors without the need for adding sensors to typical in-service profilers. These algorithms combine standard filtering techniques with an enhancement of the Walker and Becker error suppression algorithm.[15] The recommended algorithms mitigate errors in profile measured during stops using only the nominal set of sensors found on a typical production inertial profiler. However, the reduction in artificial roughness measured during a stop requires the elimination of valid profile content at low travel speed.

This research also investigated an inertial profiler design that incorporates additional sensors to eliminate errors in measured vertical acceleration caused by misalignment and drift in the floating-reference-height signal that appears after double integration. The augmented system includes body-fixed measurement of profiler acceleration and rotation rate in three dimensions (i.e., "inertial sensors"). This provides the means to resolve the component of profiler reference point acceleration into the direction aligned with gravity. The augmented system also includes GPS measurement of profiler host-vehicle height, vertical velocity, pitch inclination, and roll inclination. An extended Kalman filter with a backward pass for smoothing combines the inertial sensors with the GPS outputs to eliminate drift in the floating reference height. Special provisions are included for incorporating the height sensor into the estimate of floating reference height when the profiler host-vehicle forward speed is close to zero.

REPORT ORGANIZATION

Chapter 2 presents technical background in support of the engineering approach. This includes an introduction to the IRI and roughness profiles, a definition of the waveband of interest for roughness measurement, and a description of a method for assessing profile accuracy. The chapter also demonstrates the accelerometer alignment problem using a simple dynamic model, and presents kinematic equations in support of the approach taken to eliminate profile measurement errors.

Chapter 3 describes a custom-built inertial profiler that was designed and fabricated to support the experimental evaluation of profiler design modifications proposed for reducing measurement error. This system includes the nominal sensors that appear on a typical commercial profiler and several additional sensors to support the measurement of three-dimensional kinematics and drift removal via Kalman filtering.

Chapter 4 describes an experimental assessment of the accuracy and repeatability of profile measured by the system using the nominal sensors under ideal operational conditions (i.e., at constant speed).

Chapter 5 presents error suppression algorithms proposed in this research for application to inertial profilers without adding sensors to the typical commercial design. These algorithms emphasize the reduction of errors in measured roughness during stop-and-go operations, but do so at the expense of profile measurement accuracy at low travel speed. The chapter proposes error suppression algorithms designed for both temporal and spatial profile data collection

architectures. The performance of each algorithm is compared to the performance of baseline algorithms with no error suppression. Performance is also evaluated in terms of expectations for adequate profile measurement accuracy.

Chapter 6 proposes the use of an augmented sensor set to improve the measurement of the floating reference height. This design uses a multi-rate, extended Kalman smoother to derive an estimated floating-reference-height signal from inertial and GPS measurement of profiler host-vehicle kinematics. The chapter presents alternative versions of the proposed design to account for cases when GPS outputs are unavailable. The performance of each design is compared to the baseline system without additional sensors or error suppression algorithms. Performance is also evaluated in terms of expectations for adequate profile measurement accuracy.

Chapter 7 summarizes the results, presents conclusions and suggestions for future work, and reviews the contributions made by this research.

CHAPTER 2. TECHNICAL BACKGROUND

This chapter presents the technical background and describes preliminary analysis conducted to support the research. The first section reviews standard profile analysis methods and establishes techniques for quantifying profile measurement errors. The second section examines the signals that contribute to profiles measured by inertial systems, and demonstrates the role of high-pass filtering in the profile calculation process. The third section demonstrates the contamination of measured profile caused by accelerometer misalignment using a simple dynamic model. It presents three-dimensional kinematic equations for deriving true vertical acceleration from the output of body-fixed sensors.

PROFILE MEASUREMENT REQUIREMENTS

This research requires objective comparison of profiles measured in different passes by the same device, calculated using alternative algorithms from raw data obtained in the same pass, or measured by two different devices. This document reports differences in measured roughness in terms of changes to average IRI values over a pavement segment of standard length and the peak roughness within a pavement segment using roughness profiles. Agreement between profile traces is quantified using cross correlation of profiles that have been filtered to emphasize content that affects the IRI.

This section presents technical background needed to interpret the comparisons of measured profiles and roughness.

International Roughness Index

The IRI is a general pavement roughness indicator designed to estimate the relative level of vehicle vibration caused by the unevenness of the road.[34] The index is based on a 2-DOF quarter-car simulation of a broadly representative vehicle's response to the profile of the road surface.[67] The IRI is calculated using four steps.[68]

1. Convert the elevation profile to slope profile using a finite difference between adjacent points.

2. Apply a moving average with a base length of 9.84 inches. This step approximates the envelopment of short-duration profile features by the tire.

3. Pass the smoothened profile through the Golden-Car Model using a simulated forward speed of 49.7 mi/hr. The Golden-Car Model is a linear quarter-car simulation with standard vehicle properties. (See figure 11.) The Golden-Car Model predicts the spatial velocity across the suspension in units of slope.

4. Calculate the average rectified value from the Golden-Car Model output trace.
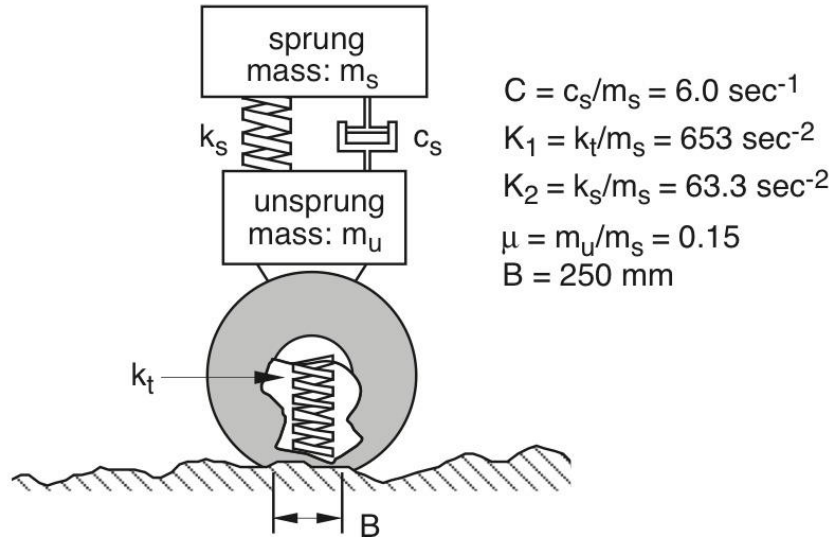
Figure 11. Schematic. Golden-Car Model.[c][(68)]

The figure includes the following parameters:

$$C = c_s/m_s = 6.0\ \text{sec}^{-1}$$
$$K_1 = k_t/m_s = 653\ \text{sec}^{-2}$$
$$K_2 = k_s/m_s = 63.3\ \text{sec}^{-2}$$
$$\mu = m_u/m_s = 0.15$$
$$B = 250\ \text{mm}$$

The IRI Scale

The calculation of IRI as described above can be performed for a section of road of any length. However, when profile is measured over long sections of roadway, an IRI value is often reported using 0.1-mile-long segments.[(3,13)] The FHWA Transportation Performance Management (TPM) system defines a *pavement section* as having a nominal length of 0.1 mi within their reporting requirements.[(5)] When it is appropriate, this research quantifies the effect of profile measurement errors by the bias they impose on the average IRI within a 0.1-mile-long segment of profile.

The IRI scale starts at 0 for a perfectly smooth road and increases with roughness of the road, with no limit at the upper end of the scale.[(69)] The IRI for a given length of profile is typically expressed in in/mi or m/km. This is often interpreted as the accumulated absolute suspension stroke normalized by travel distance, which is mathematically equivalent to the average absolute spatial velocity across the suspension. The FHWA TPM system assigns the following ratings to pavement sections based on their IRI value: (1) good (< 95 inches/mi), (2) fair (95 inches/mi to 170 inches/mi), and (3) poor (> 170 inches/mi).[(5)] Table 1 lists the IRI ranges for various qualitative categories used by the FHWA, including those used prior to the TPM.[(70)] In both eras, the poor category was considered "less than acceptable."[(70)]

---

[c] From Sayers, M. W. On the Calculation of International Roughness Index from Longitudinal Road Profile. *Transportation Research Record: Journal of the Transportation Research Board*, No. 1501, 1995, Figure 2, p. 3. Copyright, National Academy of Sciences. Reproduced with permission of the Transportation Research Board.

Table 1. FHWA IRI Ratings.[70]

Rating	TPM IRI Range (inches/mi)	Pre-TPM for Interstate (inches/mi)	Pre-TPM for non-Interstate (inches/mi)
Very Good	—	< 60	< 60
Good	< 95	60–94	60–94
Fair	95–170	95–119	95–170
Mediocre	—	120–170	171–220
Poor	> 170	> 170	> 220

Figure 12 shows the distribution of IRI values for NHS pavement sections that appeared within the 2018 FHWA HPMS submittal. The FHWA provided the data used to create this distribution. These data included IRI values, segment length, estimated traffic, and other items for 3,093,742 NHS pavement sections.

232,207 mi total
1,802 mi with IRI > 350 inches/mi
bins 5 inches/mi wide
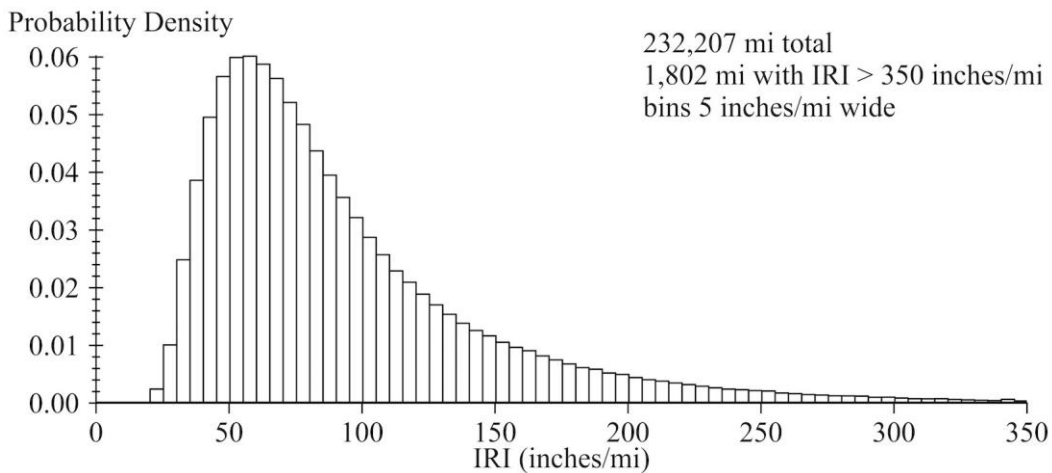
Figure 12. Graph. NHS IRI distribution, 2018.

The IRI values that contributed to the distribution in figure 12 were weighted by segment length, although a wide majority of pavement sections were 0.1 miles long. The IRI values were not weighted by traffic. The distribution includes IRI values from a total length of 232,207 miles, including 146,846 miles (63.24 percent) in the good category, 61,854 miles (26.64 percent) in the fair category, and 23,507 miles (10.12 percent) in the poor category.

Roughness Profiles

A short-interval roughness profile displays the spatial distribution of roughness within a pavement section, and provides a means to quantify the severity of localized roughness.[71] Typically, roughness profiles are used to identify localized roughness caused by construction defects, built-in features, and pavement distress.[72–74] Figure 13 through figure 16 provide examples.

Figure 13 shows profiles from the left and right wheel path on a State route in an urban area. The horizontal axis shows the distance along the route using the State's distance referencing system. The profile is high-pass filtered to make sources of roughness that affect the IRI more visible.

16

The range shown in figure 13 includes a utility cover in the left wheel path and a bridge. Figure 14 provides an image of the bridge. A joint in the center of the bridge is deteriorated, particularly in the right wheel path. (See figure 15.)
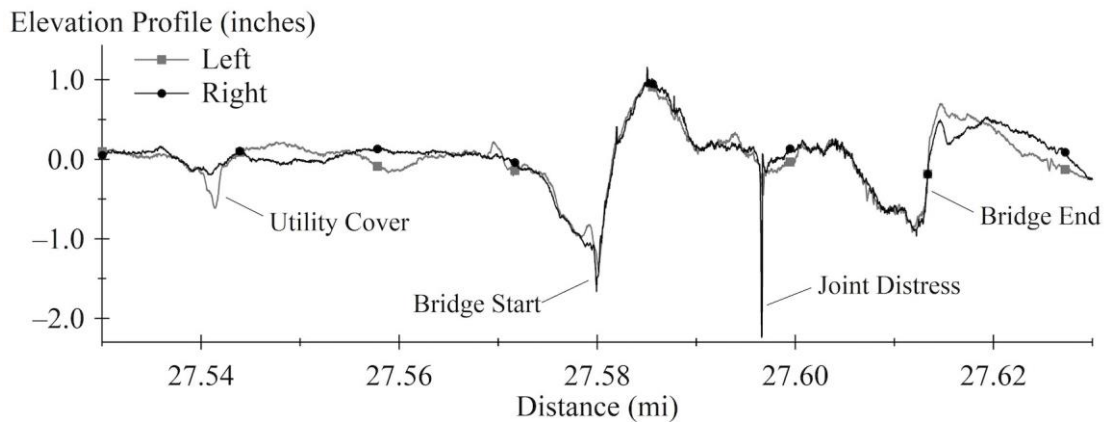
Figure 13. Graph. Elevation profiles, urban bridge encounter.
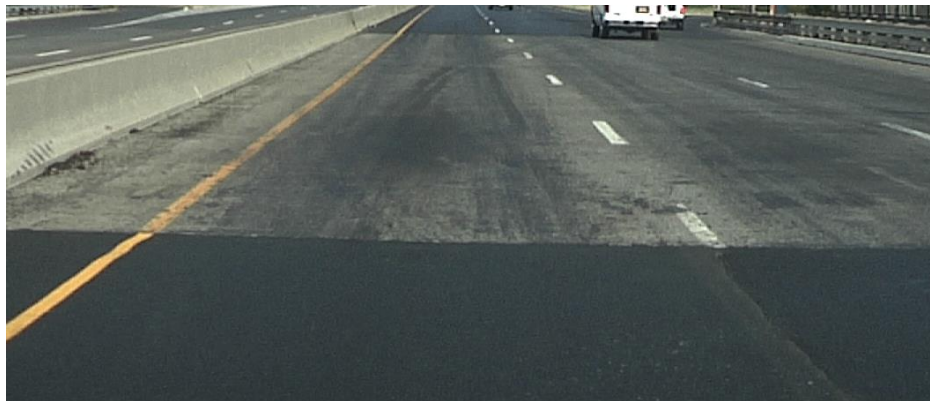
Figure 14. Image. Urban bridge encounter.

Figure 15. Image. Deteriorated bridge joint.

Figure 16 shows the short-interval roughness profile for both wheel paths using a base length of 25 ft. Each point in the roughness profiles represents the IRI averaged over a 25-ft pavement segment ranging from 12.5 ft upstream to 12.5 ft downstream. The roughness profiles are calculated as follows: (1) Scale the trace produced by Steps 1 through 3, above, of the IRI calculation procedure to the desired units (e.g., inches/mi); (2) Rectify the trace (i.e., take the absolute value of every point); and (3) Apply a moving average to the rectified trace with the desired base length.
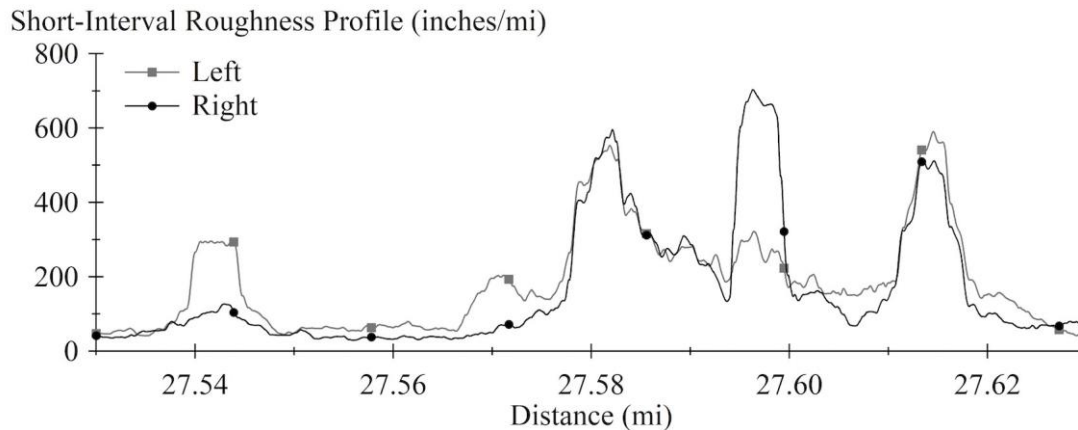
Figure 16. Graph. Roughness profiles, urban bridge encounter.

Over the 0.1-mile-long pavement section shown in figure 13, the left profile had an IRI of 185.9 inches/mi and the right profile had an IRI of 167.1 inches/mi. The short-interval roughness profile demonstrates that the utility cover, joint distress, and the interfaces between the bridge deck and the surrounding pavement contribute heavily to the average roughness. For example, the short-interval roughness profile from the right wheel path rises to a peak value of 707 inches/mi at the distressed joint. The sub-segment of profile corresponding to this point represents about 4.8 percent of the overall length shown. As such, it accounts for about 33.5 inches/mi of the average IRI for the 0.1-mile-long segment.

In many cases, such as stop-and-go operations, profile measurement errors appear as severe artificial roughness at a specific location. In this research, the peak value of the short-interval roughness profile is used to quantify the effects of localized measurement errors on overall measured roughness. In this document, *short-interval roughness profile* refers to a profile of roughness using the IRI, and averaged over a base length of 25 ft.

Waveband of Interest

This section establishes a frequency range of interest for profile measurement. A previous study established a waveband of interest for profile measurement with an emphasis on roads with high travel speeds.[75] This section presents an update of that work with consideration of unique spectral content that exists on low-speed, recreational roadways.

The calculations use linear analysis to combine idealized spectral density functions for a range of road types with the frequency response function for the IRI algorithm. The spectral density functions include limit cases for measured profiles, in which either long-wavelength content or short-wavelength content make up a large share of the roughness. To capture a broad range of vehicle responses, the analysis examines modifications to the IRI algorithm for a range of speeds, as well as sprung-mass acceleration and dynamic tire load variation from the underlying Golden-Car Model.

18

Spectral Models

Andrén reviewed several spectral models of single-track road profiles that have been proposed in the literature.[76] These models idealize measured road spectral density functions using simple functions with an assumed shape. For example, the International Organization for Standardization (ISO) recommends fitting the function shown in figure 17 to the profile elevation spectrum.[77]

$$G(v) = G(v_0)\left(\frac{v}{v_0}\right)^{-w}$$

Figure 17. Equation. ISO fitting function for profile elevation spectrum.

In figure 17, $G(v)$ is the fitted function, v is wave number, $G(v_0)$ is the spectral density at a reference wave number v_0, and w is an exponent that determines the function slope with logarithmic scaling. (ISO uses different symbols.) Fitting is done with a straight-line approximation to the spectrum with log-log scaling.

When the exponent w is equal to 2, the spectrum of slope, $G'(v)$, is constant as shown in figure 18.

$$G'(v) = \frac{G(v_0)}{(2\pi v_0)^2} = G_s$$

Figure 18. Equation. ISO profile slope spectrum with $w = 2$.

In this case, the road is approximated by white noise slope. However, Andrén and Kropáč and Múčka have observed that values in the range of 1.5 to 3.5 are common.[76,78] Others have split the spectrum and derived a straight-line approximation over each range (e.g., Dodds and Robson).[79] The split model accommodates a change in slope in the log-log spectrum using a unique value of w in each range.

To account for the change in characteristic slope over the log-log spectrum, some have proposed a spectral shape made up of a combination of white noise sources. La Barre proposed one such model for European roads, as shown in figure 19.[80]

$$G'(v) = G_0\left[1 + \left(\frac{v_0}{v}\right)^2\right]$$

Figure 19. Equation. Profile slope spectrum proposed by La Barre.

In figure 19, G_0 and v_0 are constants within the model. At low wave numbers, white noise spatial acceleration dominates this function, and at high wave numbers, white noise slope dominates this function. The break point between the two is determined by the value of v_0. The study of European roads found that the break point to be about 0.02 cycles/ft for "rigid constructions" and 0.05 cycles/ft for "flexible constructions." [80] In terms of wavelength, this is 50 ft and 20 ft, respectively.

This analysis uses a model proposed by Sayers that combines three sources of white noise, as shown in figure 20.[81] In figure 20, G_e represents the contribution of white noise elevation, G_s represents the contribution of white noise slope, and G_a represents the contribution of white noise spatial acceleration. This was selected with the expectation that the arithmetic combination of terms with exponents of 0, 2, and 4 would provide enough flexibility to capture the variations described above.

$$G(v) = G_e + \frac{G_s}{(2\pi v)^2} + \frac{G_a}{(2\pi v)^4}$$

Figure 20. Equation. Sayers model for elevation profile spectrum.

Sayers provided coefficients for several in-service roads that cover a diverse range of spectral shape, and recommended four representative cases as standard simulation inputs.[82] (See table 2.)

Table 2. Model coefficients for four sample roads.[82]

Description	G_a	G_s	G_e
	$1/(\text{ft}\cdot\text{cycle})\cdot 10^{-6}$	$\text{ft}/\text{cycle}\cdot 10^{-6}$	$\text{ft}^3/\text{cycle}\cdot 10^{-6}$
Normal	0	65.6	0
Asphalt with Long Waves	2.13	65.6	0
Rough (Short Waves)	0	328.1	35.3
Limit Roughness	0	984.3	282.5

"Limit roughness" represents the sample in which the largest proportion of content comes from the high wave-number (short-wavelength) range. "Asphalt with long waves" represents the sample in which the largest proportion of content comes from the low wave-number (long-wavelength) range, with a ratio of G_a to G_s of 0.033 ft^{-2}.

Figure 21 shows the expression for the spectral model by Sayers is the slope domain. Comparison of figure 21 to figure 19 (the La Barre model) yields the relationship shown in figure 22. For "flexible constructions" (i.e., wavy asphalt) this is a ratio of 0.099 ft^{-2}.

$$G'(v) = \frac{G_e}{(2\pi v)^{-2}} + G_s + \frac{G_a}{(2\pi v)^2}$$

Figure 21. Equation. Sayers model for elevation profile spectrum.

$$\frac{G_a}{G_s} = (2\pi v_0)^2$$

Figure 22. Equation. Relationship between Sayers and La Barre models.

For this research, a limited number of low-speed, recreational roadway profiles were analyzed to identify a new limit case. These roadways are built in areas with limited opportunity to select or alter road grade, and are meant for travel at low speed. These roads exhibited values of the ratio of G_a to G_s of 0.132 ft^{-2} to 1.033 ft^{-2}, with a quarter of the values above 0.743 ft^{-2}.

The linear analysis of wavelength sensitivity below examines the cases listed in table 3. "Very wavy" corresponds to low-speed, recreational roads; "standard" corresponds to La Barre's observations for flexible constructions; and "choppy" corresponds to an extreme among the observations made by Sayers.

Table 3. Sample cases for analysis.

Description	G_a/G_s (ft^{-2})	G_e/G_s (ft^2)
Very wavy	0.743	0
Standard	0.099	0
White noise slope	0	0
Choppy	0	0.861

Frequency Response

Figure 23 shows the temporal frequency response of the IRI algorithm in terms of slope (spatial velocity across the suspension) as a function of slope spectral density. Figure 23 presents an alternative axis showing wavelength, which corresponds to the standard Golden-Car simulation speed for the IRI of 49.7 mi/hr.
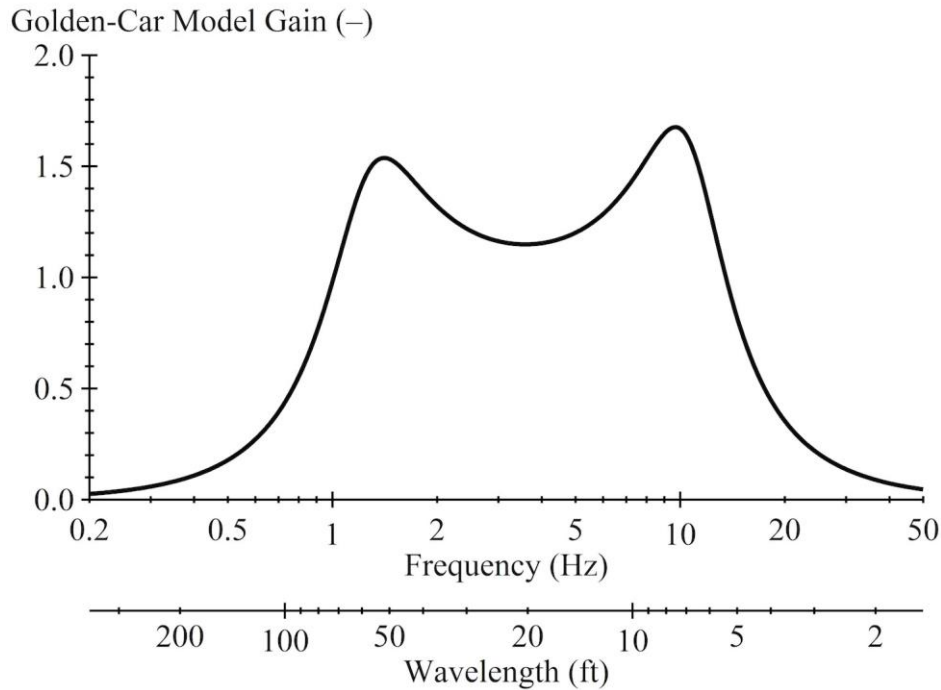
Figure 23. Graph. IRI gain for profile slope.

The frequency response function shown in figure 23 includes contributions from two linear filters. First, the moving average has a transfer function that is a fixed function of wavelength (λ). Figure 24 shows the transfer function in terms of wave number (ν), and figure 25 relates wave number to wavelength.

$$H_{MA}(v) = \frac{\sin(\pi B v)}{\pi B v}$$

Figure 24. Equation. Moving average transfer function

$$v = \frac{1}{\lambda}$$

Figure 25. Equation. Relationship between wave number and wavelength.

The second is the Golden-Car Model response transfer function for suspension stroke, as shown in figure 26. In figure 26, V is simulated travel speed, and ω is angular frequency. Figure 27 provides the expression for the denominator (D).

$$H_{GCSS}(\omega = 2\pi v V) = \frac{K_1 \omega^2}{D}$$

Figure 26. Equation. Golden-Car Model transfer function for suspension stroke.

$$D = \mu\omega^4 - (K_1 + K_2(1+\mu))\omega^2 + K_1 K_2 + jC\omega(K_1 + \omega^2(1+\mu))$$

Figure 27. Equation. Golden-Car Model transfer function denominator.

Figure 28 shows the signal used to calculate the IRI in the wave number domain. In figure 28, $G'(v)$ is slope spectral density from the road profile. For a Gaussian signal with zero mean, the average rectified value of the output signal is proportional to the standard deviation, which is the square root of integral of the output spectrum, G_{IRI}.

$$G_{IRI}(v) = |H_{MA}(v)|^2 |H_{GCSS}(v)|^2 G'(v)$$

Figure 28. Equation. IRI algorithm output in the wave number domain.

Figure 29 shows the normalized cumulative response of the IRI calculation for the "Standard" road identified in table 3. The range of wavelengths up to 66.06 ft produces an estimate of the IRI that is 95 percent of the value for the entire waveband, and wavelengths up to 119.10 ft capture 99.5 percent of the total. Figure 29 also shows an accumulation of the IRI running downward from the long-wavelength end of the spectrum. In this case, wavelengths down to 6.07 ft capture 95 percent of the overall IRI value and wavelengths down to 3.67 ft captures 99.5 percent.
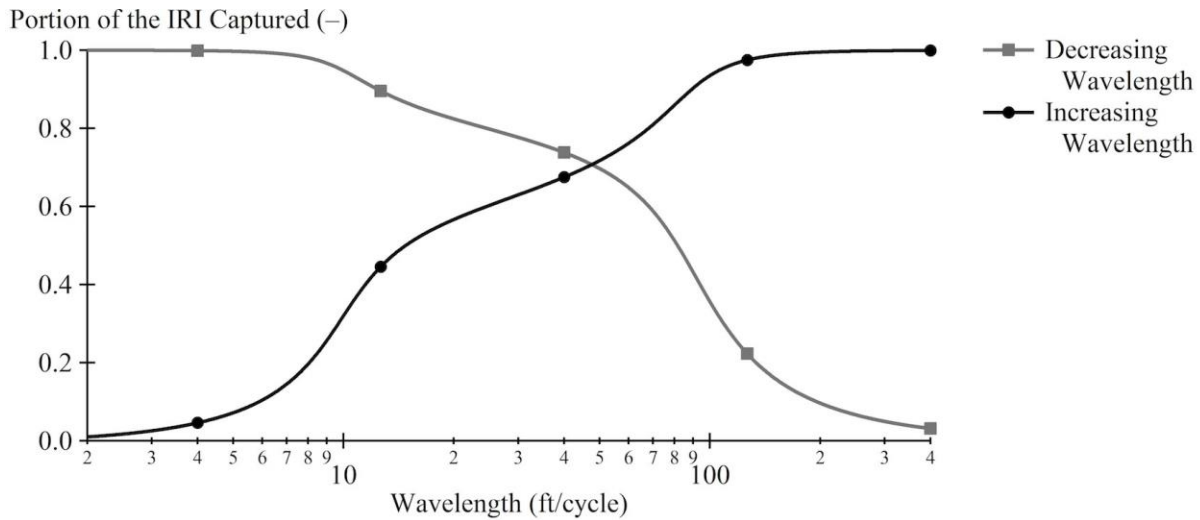
Figure 29. Graph. Portion of the IRI captured versus wavelength.

Wavelength Thresholds

Table 4 presents the wavelength thresholds that correspond to capture of 99.5 percent for the overall IRI value for the four sample roads listed in table 3. (The range defined by these thresholds corresponds to a total error of 1 percent.)

Table 4. Thresholds for 0.5 percent error in IRI.

Sample Case	Very Wavy	Standard	White Noise Slope	Choppy
Long Wavelength (ft)	140.69	119.10	67.04	61.65
Short Wavelength (ft)	4.81	3.67	3.16	2.00

Alternatives to the IRI using lower speeds are also currently under consideration, because roughness measurements based on profile are increasingly performed on low-speed and urban roadways. Alternatives at higher speeds are also under consideration, because prevailing speeds on limited access freeways are much higher than 49.7 mi/hr. When the Golden Car is simulated at other speeds, the temporal frequency axis in figure 23 remains unchanged, but the wavelength axis shifts (leftward) in proportion to speed. In terms of spectral content, a change in speed changes the features of the road that affect the response. Further, as speed decreases the moving average attenuates a progressively larger portion of the content that affects the Golden Car.[83]

To help ensure valid measurement of profile for the IRI and other indices tied to vehicle response, the analysis was extended to include: Golden-Car Average Rectified Slope (GCARS) at 24.9 mi/hr, GCARS at 74.6 mi/hr, and Ride Number (RN). RN is a profile-based index with an empirical link to panel ratings of user satisfaction with pavement ride quality.[84,85]

Table 5 and table 6 provide the results. Note that RN filters the profile in a manner similar to the IRI to emphasize the waveband of interest, and accumulates root mean square (RMS) of the resulting signal. The RN algorithm casts the RMS value into a 0-to-5 scale using a non-linear transformation. The results in table 5 and table 6 pertain to the pre-transform RN value (PTRN).

Table 5. Long-wavelength thresholds for 0.5 percent error in IRI.

Index	Very Wavy (ft)	Standard (ft)	White Noise Slope (ft)	Choppy (ft)
$GCARS_{120}$	215.17	195.64	100.16	95.91
$GCARS_{40}$	65.23	48.38	34.17	27.72
PTRN	54.29	38.77	28.37	19.02

Table 6. Short-wavelength thresholds for 0.5 percent error in IRI.

Index	Very Wavy (ft)	Standard (ft)	White Noise Slope (ft)	Choppy (ft)
$GCARS_{120}$	7.79	5.89	4.48	2.82
$GCARS_{40}$	2.23	1.94	1.87	1.37
PTRN	1.23	1.12	1.10	0.48

For measurement of IRI, the waveband of interest is 2 ft to 141 ft. The analysis above shows that accommodation of other applications of profile related to vehicle response (i.e., general roughness measurement) requires a waveband from 0.48 ft to 215 ft.

Objective Trace Comparison

This research quantifies agreement between profiles using a standard method that is based on cross correlation.[86,87] In this application, two profiles are cross-correlated after they are filtered to emphasize the frequency content of interest.

Cross Correlation

Figure 30 shows the estimate of the cross-correlation function for two measures of road profile over a finite length L. In figure 30, p and q are each measurements of road profile as a function of distance x. The cross correlation function, R, exists as a continuous function of the offset distance x_{off} between the profiles.

$$R_{pq}(x_{off}) \approx \frac{1}{L}\int_0^L p(x)q(x+x_{off})\,dx$$

Figure 30. Equation. Cross correlation for continuous spatial signals.

Since the profile is sampled at discrete intervals, the integral must be replaced by a summation shown in figure 31. In figure 31, the subscripts indicate discrete sample numbers, recorded at a distance interval of Δx. The number of samples, N, is the value needed to cover the overall length of interest.

$$R_{pq}(i\Delta x) \approx \frac{1}{N}\sum_{k=1}^{N} p(x_k)q(x_{k+i})$$

Figure 31. Equation. Cross correlation for discrete spatial signals.

The equation in figure 31 has two weaknesses when applied to road profiles. First, it yields a cross correlation function in units of elevation squared. Figure 32 provides a more desirable rating system that is normalized to produce a value of 1 for perfect correlation.

$$\rho_{pq}(i\Delta x) = \frac{1}{\sigma_p \sigma_q} \sum_{k=1}^{N} \left(p(x_k) - \mu_p \right) \left(q(x_{k+i}) - \mu_q \right) = \frac{1}{\sigma_p \sigma_q} \sum_{k=1}^{N} \hat{p}(x_k) \hat{q}(x_{k+i})$$

Figure 32. Equation. Normalized cross correlation for discrete spatial signals.

In figure 32, the hats over the symbols "p" and "q" indicate that the profiles are offset vertically to have a mean value of zero. The values σ_p and σ_q represent the standard deviation of profiles p and q, respectively. The equation in figure 32 produces a –1 to 1 rating of the correlation, and will only produce a value of 1 when the shape of both profiles are exactly the same and they are synchronized.

A second weakness of the equation in figure 31 is that differences in overall roughness are not penalized by the standard cross correlation function. Two profiles that have the exact same shape but very different amplitudes would be rewarded with a perfect rating by the equation in figure 32. To compensate for this, the factor shown in figure 33 is applied to the normalized cross correlation function. This adjustment factor diminishes the value of correlation when the standard deviations of the profiles are not equal.

$$\gamma = \frac{\min(\sigma_p, \sigma_q)}{\max(\sigma_p, \sigma_q)}$$

Figure 33. Equation. Amplitude adjustment for cross correlation.

This research quantifies the agreement between profiles for a given waveband as shown in figure 34.

$$\text{Agreement score} = \rho_{\max} \cdot \gamma$$

Figure 34. Equation. Amplitude adjustment for cross correlation.

In figure 34, $\rho_{\max}$ is the maximum correlation coefficient over the range of offsets included in the calculations.

Filtering

Repeatability and agreement to a reference measurement are quantified by cross correlating the output of the IRI filter. That is, the IRI algorithm (Steps 1 through 3 under "International Roughness Index," above) is applied to each profile, and the resulting signals are cross-correlated. A minimum threshold value for cross correlation of 0.92 is adopted from American Association of State Highway and Transportation Officials (AASHTO) R56-14.[d][(87)] This threshold corresponds to adequate roughness measurement accuracy in production applications. AASHTO R56-14 also requires repeatability of 0.98 for systems used to make reference

---

[d] Compliance is not required under Federal law. AASHTO R56-14 serves as a guide specification.

measurements.[87] Similarly, Karamihas recommended a threshold value of 0.98 for a "research class" profiler.[86]

For diagnostic purposes, profiles are cross-correlated using slope in three additional wavebands: (1) a long waveband, (2) a medium waveband, and (3) a short waveband. The profiles are converted to slope using a finite difference, then are filtered to pass content in the wavelength ranges from 0.46 ft to 5.25 ft, 5.25 ft to 26.2 ft, and 26.2 ft to 215 ft for the short, medium, and long wavebands, respectively. Collectively, these three bands cover the range of interest identified above. The range was split into three bands for their diagnostic value, and to avoid cases in which a portion of the waveband dominates the mean square of the slope profile. Appendix A describes the high-pass (HPF_{B3x2}) and low-pass (LPF_{B3x2}) filters used to isolate the long, medium, and short wavebands. Cut-off wavelength settings (λ_c) correspond to the limits for each range provided above.

SIGNAL FLOW

This section examines sensor signals from a long profile measurement collected under favorable conditions. The discussion shows the relative contribution of the height-sensor signal and the floating-reference-height signal to the overall profile, and that they interact heavily over a portion of the frequency range of interest. The discussion also explains why high-pass filtering is a necessary part of the profile measurement process, and presents an example of the effect of filter type on the profile.

Signal Interaction

Figure 35 shows the spectral content of a profiler accelerometer signal measured at 67 mi/hr over 2.5 mi of limited-access highway. These data were collected on I-94 eastbound starting near milepost post 161 (near Chelsea, Michigan) by a profiler mounted near the center of the wheelbase on a minivan. The test section included several patched transverse cracks and patched potholes. The influence of vehicle dynamic response is apparent in the signal. For example, the spectral density includes elevated content due to sprung-mass resonant response at near 1 Hz to 2.5 Hz and elevated content due to unsprung-mass resonant response at 10 Hz to 20 Hz.
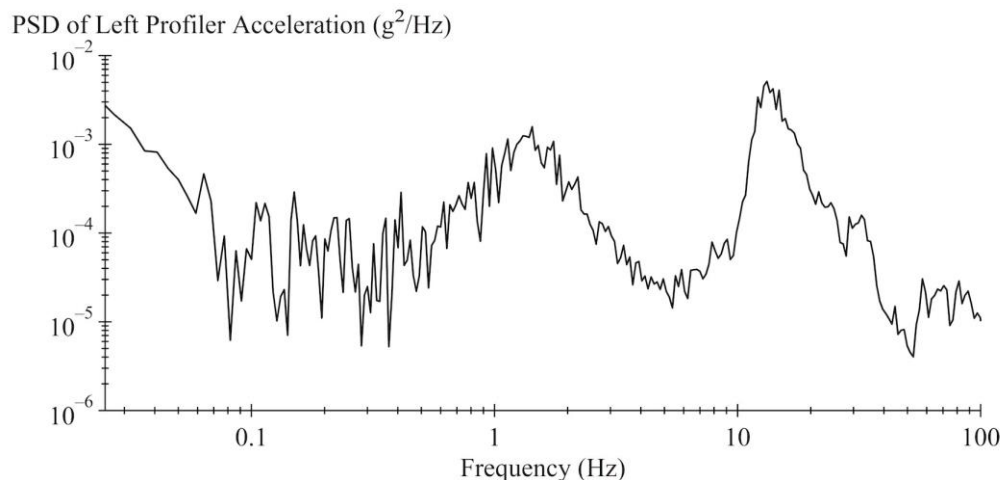
Figure 35. Graph. Accelerometer spectral content.

26

As described in Chapter 1, the raw accelerometer signal is transformed to the floating-reference-height signal using the following steps:

1. Resample the signal as a function of travel distance with a constant distance interval.

2. Divide each value in the signal by the square of forward speed to convert temporal acceleration to spatial acceleration.

3. Integrate the spatial acceleration twice in the distance domain.

The floating-reference-height signal is a record of the fluctuations in vertical position of the profiler reference point as it progressed along the pavement section. The height sensor records changes in relative vertical distance between the floating reference height and the road. Subtracting the height-sensor signal from the floating-reference-height signal produces the profile. Figure 36 shows the spectral content of the two signals for the 2.5-mile-long pavement section. The figure shows that when these signals are combined, the contribution from the accelerometer will dominate the low-frequency (i.e., long-wavelength) portion of the profile and the height sensor will contribute the most heavily to the high-frequency (i.e., short-wavelength) portion of the profile.
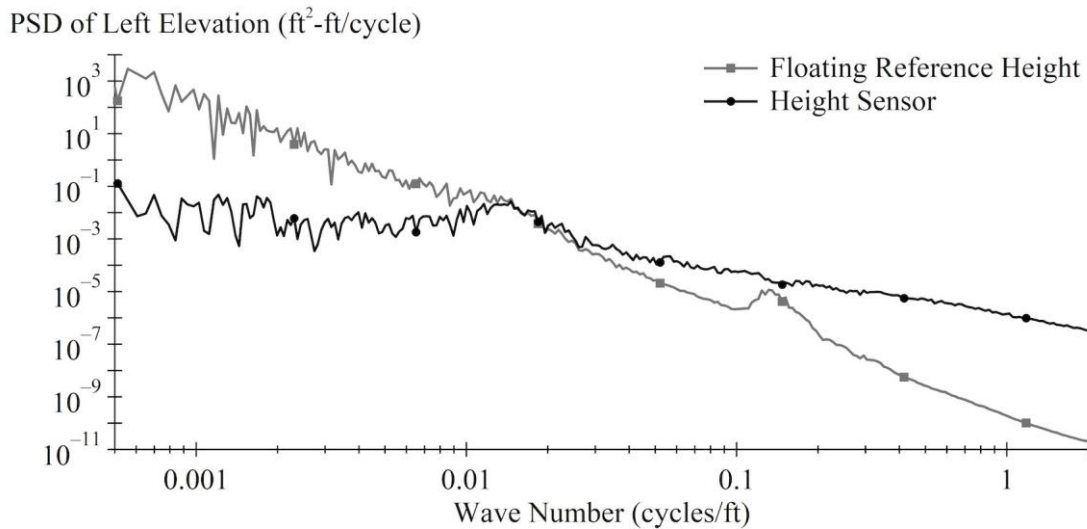
Figure 36. Graph. Spectral density of floating-reference-height and height-sensor signals.

To help illustrate this further, figure 37 provides the spectral content of the two signals and the final profile in terms of slope. The profile slope spectrum is often used in lieu of elevation spectrum to reduce the vertical range on the ordinate axis, so that more details are visible.[81,88] The floating-reference-height signal contributes most of the content to the final road profile for wavelengths greater than 164 ft, whereas the height sensor contributes most to the road profile for wavelengths below 5.3 ft.
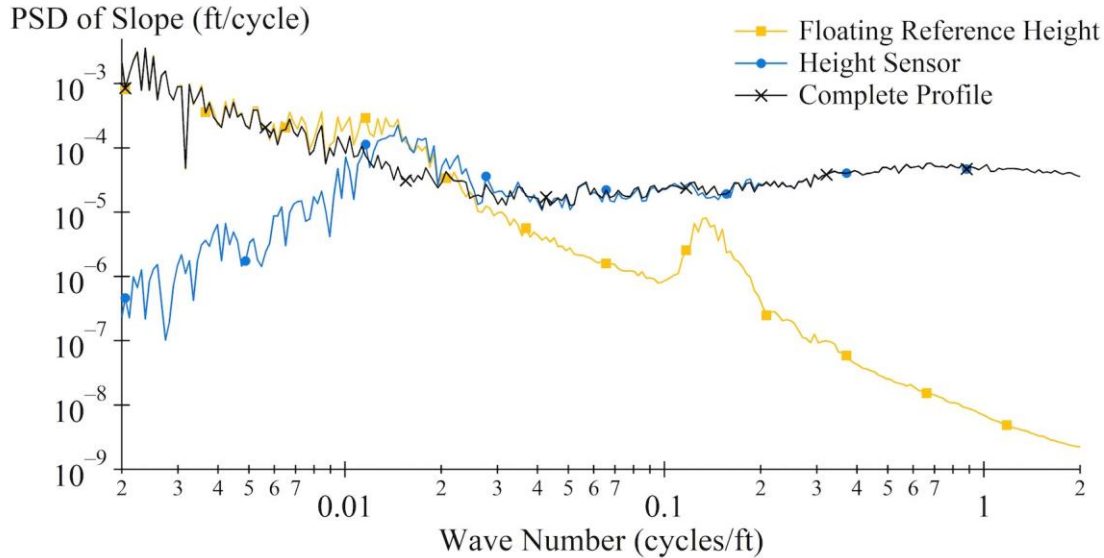
Figure 37. Graph. Slope spectral density of profile and its components.

At the host-vehicle travel speed, 10 Hz to 20 Hz corresponds to the range of wave numbers from 0.10 cycles/ft to 0.21 cycles/ft. In this range, the amplitude of the height-sensor signal and floating-reference-height signal are the same order of magnitude, although the fluctuations in the floating-reference-height signal are larger. In this frequency range, the host-vehicle reference point's motion is in phase with the changes in road profile elevation. The height-sensor signal is out of phase. As a result, the final road profile has more content in this range than either of the component signals.

The range of wave numbers from 0.010 cycles/ft to 0.026 cycles/ft corresponds to frequencies of 1 Hz to 2.5 Hz at the host-vehicle travel speed. In this range, the profiler reference point's motion is out of phase with changes in profile elevation. Due to resonant response of the host vehicle associated primarily with sprung-mass motion, the amplitudes of the floating-reference-height and height-sensor signals are much larger than the complete profile. When they are combined to compute the complete profile, much of the content within the two sensors is cancelled. In this frequency range, small errors in either of the sensor signals relative to their amplitude may appear as very large errors in the resulting profile. As such, an error in one sensor signal associated with host-vehicle sprung-mass dynamics, such as accelerometer misalignment, may affect profile measurement accuracy disproportionately.

High-Pass Filtering

The accelerometer signal that produced figure 35 through figure 37 included a small overall bias, and its average value was 0.000834 g. This may have been caused by a legitimate net vertical acceleration over the 2.5 mi of travel. However, the average acceleration may also have been caused by a slight error in calibration (once the 1 g offset was removed), slight errors in the orientation of the accelerometer on the host-vehicle chassis, or a prevailing level of tilt from true vertical caused by the overall grade or cross slope of the road. In this measurement, the average acceleration was less than 0.55 percent as large as the variance. When the signal is integrated twice to establish the elevation time history of the accelerometer, the presence of the net

acceleration will superimpose a parabolic rise in elevation of more than 240 ft. This did not exist on the test section.

Figure 38 shows the floating-reference-height signal established by integrating the raw accelerometer signal twice. In addition to the artificial parabolic rise in vertical position, the signal includes very long wavelength fluctuations. At sufficiently low frequencies the dynamic response of the vehicle diminishes, and the accelerometer follows a path that is parallel to the road surface. Under ideal conditions, this portion of the signal would approximate the second rate of change of road elevation under the accelerometer. Instead, this portion of the signal is often contaminated by operator-induced disturbances, such steering corrections for lane keeping and adjustment to the throttle for regulating speed. In addition, very long wavelength changes in road elevation associated with road geometric design and the prevailing land topography (i.e., grade changes) cause slow changes in accelerometer alignment.
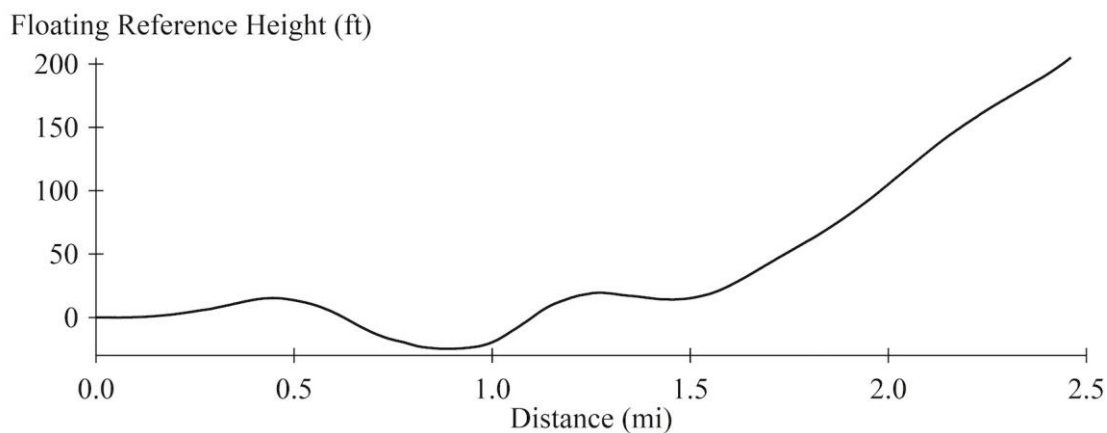
Figure 38. Graph. Floating reference from the raw accelerometer signal.

Profilers typically apply high-pass filters to suppress the contaminated portion of the floating-reference-height signal. Figure 39 shows the floating-reference-height signal that results when a third-order Butterworth filter is applied with a cut-off wavelength of 300 ft. (See HPF_{B3} in Appendix A.) The figure shows the accompanying height-sensor signal and the complete profile. Note that the high-pass filter determines the long-wavelength content within the floating-reference-height signal, which in turn strongly affects the long-wavelength content in the computed profile.
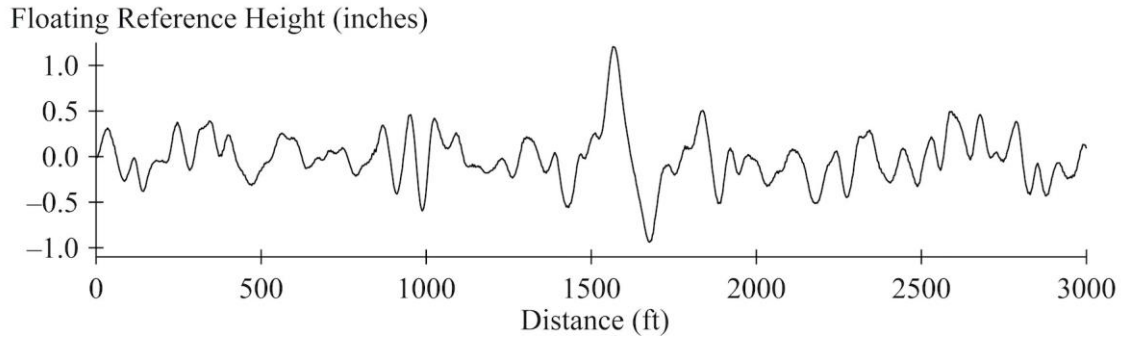
A. Floating reference height
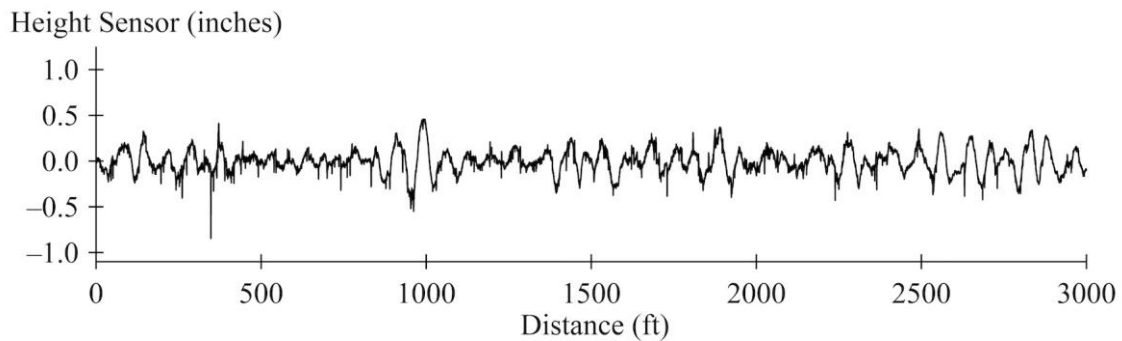
B. Height sensor
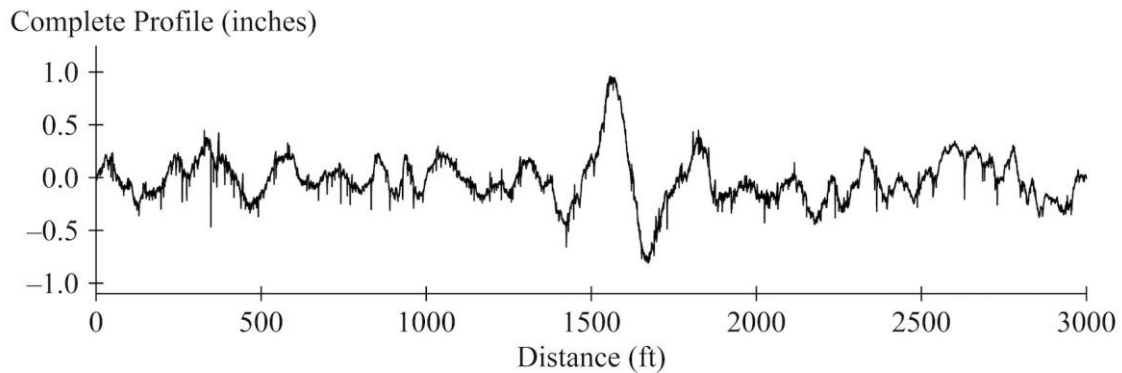
C. Complete profile

Figure 39. Graph. Floating reference height, height sensor, and complete profile traces.

Many inertial profilers apply the high-pass filter to sensor signals in real time using a recursive algorithm.[89,90] In most cases, recursive digital filters impose a non-linear phase shift. Typically, the phase shift is greatest near the cut-off wavelength. This was the case for the complete profile shown in figure 39. Figure 40 compares the complete profile to a profile processed from the same sensor signals with a bi-directional high-pass filter. The bi-directional filter applies equivalent filtering in the forward and reverse direction to cancel phase shift. (See Appendix A, HPF_{B3x2}.) The deep cracks and short-duration features are aligned in the two profiles. However, the conventional filter distorts the long-wavelength content. For example, the dip near the center

of the profile produced without phase shift by the bi-directional filter appears as a bump using the conventional filter.
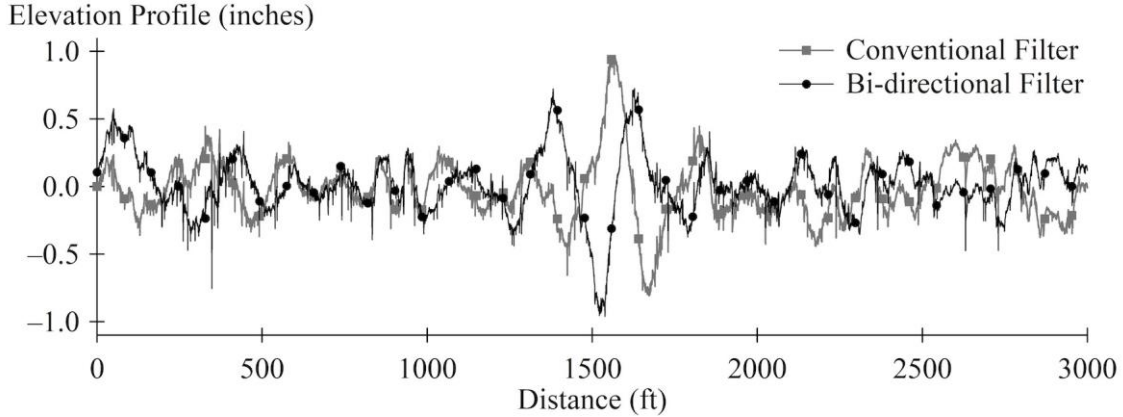
Figure 40. Graph. Effect of filter type on a raw profile trace.

SYSTEM KINEMATICS AND DYNAMICS

Three Dimensional Kinematics

Chapter 1 presented expressions for the errors in vertical acceleration measured on-board a typical inertial profiler due to misalignment of the host-vehicle body in two dimensions. Figure 41 presents the full expressions for vehicle-fixed accelerations that would be measured by servo-type accelerometers fixed on the profiler as it experiences rotations about the vehicle-fixed axes in pitch (θ) then roll (ϕ).

$$a_{xp}^b = a_{xp}^w c_\theta - (a_{zp}^w + g)s_\theta$$
$$a_{yp}^b = a_{xp}^w s_\theta s_\phi + a_{yp}^w c_\phi + (a_{zp}^w + g)c_\theta s_\phi$$
$$a_{zp}^b = a_{xp}^w s_\theta c_\phi - a_{yp}^w s_\phi + (a_{zp}^w + g)c_\theta c_\phi - g$$

Figure 41. Equations. Body-fixed accelerations.

In figure 41 (and others), s and c represent sine and cosine functions, respectively, of the angle that appears in the subscript. The equations in figure 41 express vehicle body-fixed vertical (a_{zp}^b), longitudinal (a_{xp}^b), and lateral (a_{yp}^b) acceleration in terms of vertical acceleration along an axis system aligned with gravity (a_{zp}^w) and horizontal components in a plane perpendicular to gravity (a_{xp}^w and a_{yp}^w). The equations in figure 41 include removal of a 1-g offset from the recorded value of a_{zp}^b.

As shown in figure 42, pitch is represented as a rotation about the host-vehicle lateral axis (Y_w). The subscript "w" denotes the wander axis system, which corresponds to the Society of Automotive Engineers (SAE) intermediate axis system.[91] The alignment of the Y_w axis follows the vehicle's yaw motion, but remains perpendicular to a vertical axis aligned with gravity. Roll is represented by a subsequent rotation about the body-fixed longitudinal axis (X_b). True vertical acceleration along the axis aligned with gravity is a_{zp}^w.

31
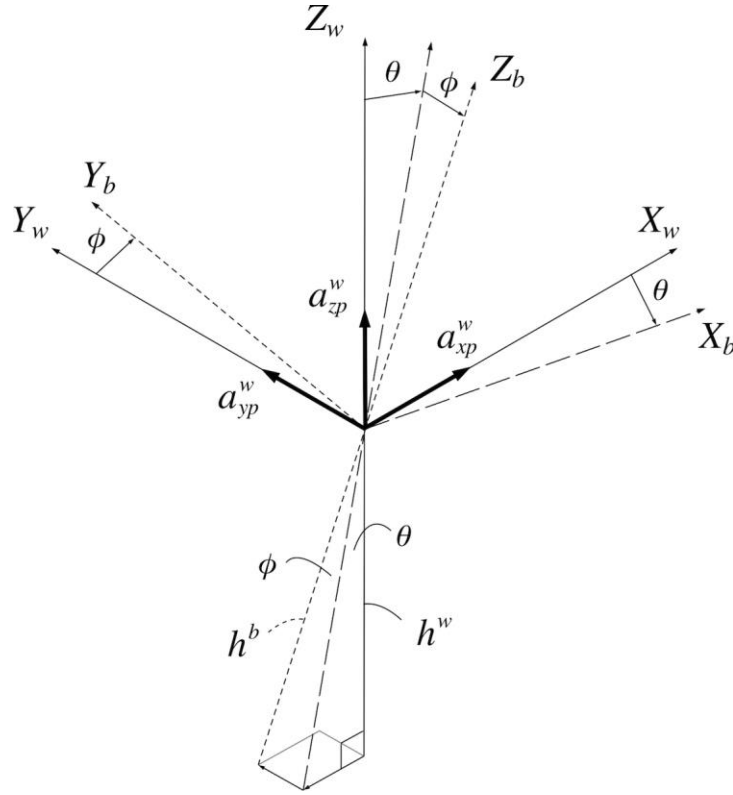
Figure 42. Schematic. Body-fixed rotations in pitch and roll.

Figure 42 also demonstrates the effect of changes in host-vehicle orientation on the range to ground measured by the height sensor. For a perfectly flat, smooth ground plane the measured range to ground along the body-fixed vertical axis (h^b) increases relative to the vertical projection along a truly vertical axis (h^w), as shown in figure 43.

$$h^b = \frac{h^w}{c_\theta c_\phi}$$

Figure 43. Equation. Body-fixed height-sensor reading.

When the road surface is not flat and smooth, lateral and longitudinal translation of the height-sensor footprint introduces additional spurious content into the height-sensor signal. In practice, the lateral and longitudinal translation is more important than the cosine error.

The signal a_{zp}^w, rather than a_{zp}^b, is required to accurately establish the floating reference height. Two strategies for obtaining this are possible:

1. Correction of a_{zp}^b to a_{zp}^w using measurements of a_{xp}^w and a_{yp}^w, as shown in figure 44.

$$a_{zp}^w = \frac{a_{zp}^b + g - a_{xp}^w s_\theta c_\phi + a_{yp}^w s_\phi}{c_\theta c_\phi} - g$$

Figure 44. Equation. Correction using wander-frame horizontal acceleration.

2. Correction of a_{zp}^b to a_{zp}^w using measurements of a_{xp}^b and a_{yp}^b, as shown in figure 45.

$$a_{zp}^w = -a_{xp}^b s_\theta + a_{yp}^b c_\theta s_\phi + (a_{zp}^b + g)c_\theta c_\phi - g$$

Figure 45. Equation. Correction using body-fixed acceleration.

Either approach requires measurement of profiler orientation (pitch and roll). Estimates of horizontal acceleration may be obtained by observing changes in wheel rotation (for a_{xp}^w) and a combination of forward speed and yaw rate or steering angle (a_{yp}^w). Since the profiler is mounted on the sprung mass of the host vehicle, horizontal acceleration measured or estimated at the vehicle's footprint (i.e., the wander frame) may not be sufficient. Measurement of body-fixed lateral and longitudinal acceleration requires additional sensors that are not commonly available on existing profilers. However, the approach shown in figure 45 was selected, because direct measurement of the acceleration inputs was possible and orientation could be derived in a manner similar to a common strap-down navigation system.

Theoretical Demonstration

Figure 46 shows a planar inverted pendulum model with 1 DOF that demonstrates the errors caused by accelerometer misalignment. The model represents the host vehicle as an inverted pendulum attached to a trolley with prescribed longitudinal motion $x(t)$. Although this model is very simple, it includes a DOF that permits the body on which the profiler is mounted to change its alignment in response to horizontal acceleration. Collectively, the host-vehicle properties m (mass), h_{rc} (rotation center height), L_{cm} (center of mass height in relation to the rotation center), k_r (rotational stiffness resisting rotation), and c_r (rotational damping) define the host vehicle's dynamic response to horizontal acceleration. The dimensions h_p and l_p describe the profiler's position on the host vehicle in relation to the rotation center.
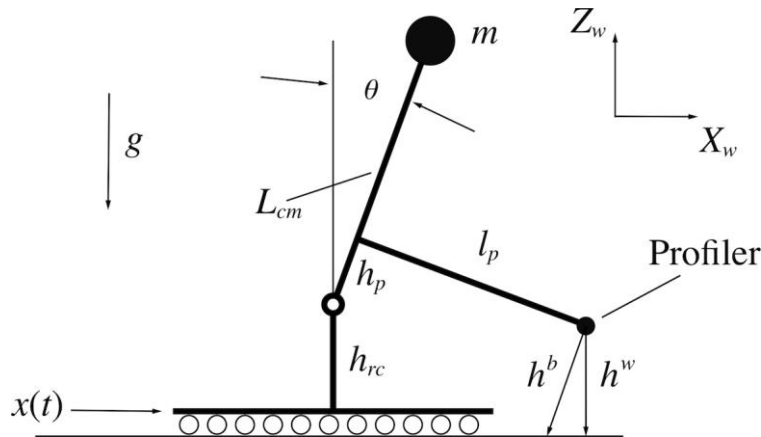
Figure 46. Schematic. Inverted pendulum model.

When the trolley experiences deceleration, the pendulum (i.e., the host-vehicle body) changes its orientation and changes its alignment by an angle θ. This has two consequences. First, the relative height of the profiler compared to the road surface measured by the misaligned height sensor is slightly larger than the true value. This affects the reading as shown in figure 47.

$$h^b = \frac{h^w}{c_\theta}$$

Figure 47. Equation. Body-fixed height-sensor reading during pitch.

Second, as shown in figure 48, the measured components of vertical and horizontal acceleration are cross-contaminated. The true acceleration magnitude of the profiler, a_p, includes a contribution from an absolute vertical component a_{zp}^w, which is desired for robust measurement of the inertial platform, and an absolute horizontal component a_{xp}^w. The same vector also breaks down into a "body-fixed" vertical component a_{zp}^b, which is measured by a typical profiler, and a body-fixed horizontal component a_{xp}^b. Figure 48 illustrates the equations above visually and shows the difficulty in applying corrections to vertical acceleration using on-board measurements of horizontal acceleration.
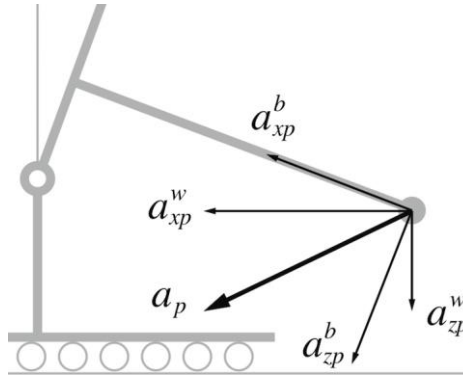
Figure 48. Schematic. Acceleration components.

Figure 49 shows the equation of motion for the pendulum alignment angle is, and figure 50 through figure 52 provide equations for relevant outputs.

$$\ddot{\theta} - \frac{g}{L_{cm}} s_\theta + \frac{k_r}{mL_{cm}^2}\theta + \frac{c_r}{mL_{cm}^2}\dot{\theta} + \frac{\ddot{x}(t)}{L_{cm}}c_\theta = 0$$

Figure 49. Equation. Equation of motion for the inverted pendulum.

$$a_{xp}^b = \ddot{x}c_\theta + h_p\ddot{\theta} - l_p\dot{\theta}^2$$

Figure 50. Equation. Body-fixed vertical acceleration output.

$$a_{zp}^b = \ddot{x}s_\theta - h_p\dot{\theta}^2 - l_p\ddot{\theta}$$

Figure 51. Equation. Output, vertical acceleration in the wander frame.

$$h^b = \left(h_{rc} + h_p c_\theta - l_p s_\theta\right) \Big/ c_\theta$$

Figure 52. Equation. Body-fixed height-sensor output.

Kinematic transformations of the same type shown in figure 41 and figure 43 provide expressions for a_{zp}^w, a_{xp}^w, and h^w.

For the deceleration pulse defined in figure 53, figure 54 through figure 57 show the response of the trolley operating on a perfectly flat, smooth surface.

$$\ddot{x}(t) = -a_{xpeak}\sin\left(2\pi(t - t_s)/T\right);\ 2 \le t \le 3 \text{ sec}$$
$$\ddot{x}(t) = 0;\ t < 2 \text{ sec},\ t > 3 \text{ sec}$$

Figure 53. Equations. Deceleration pulse.

In figure 53, a_{xpeak} is the peak deceleration value of 0.4 g, T is the duration of the pulse (1 second), and t_s is the start time (2 seconds). Figure 54 shows the pulse and the measurement of longitudinal acceleration that would be obtained by an accelerometer fixed in the profiler host-vehicle body, which includes the influence of changes in orientation and the projection of gravity and true vertical acceleration onto its measurement axis.
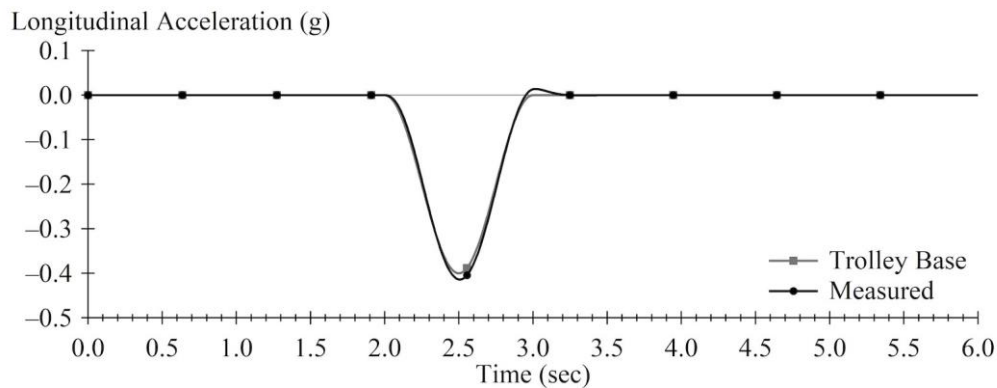
Figure 54. Graph. Deceleration pulse.

Figure 55 shows the ideal measurement of vertical acceleration and the measurement that would be obtained by an accelerometer fixed in the profiler host-vehicle body. Again, the measurement by the sensor fixed in the profiler host vehicle is affected by its change in orientation. Both signals include the initial downward acceleration at the onset of the pulse, followed by a rebound and damped oscillation. However, the accelerometer fixed to the profiler host-vehicle body includes a downward bias due to the projection of longitudinal deceleration onto its sensitive axis.
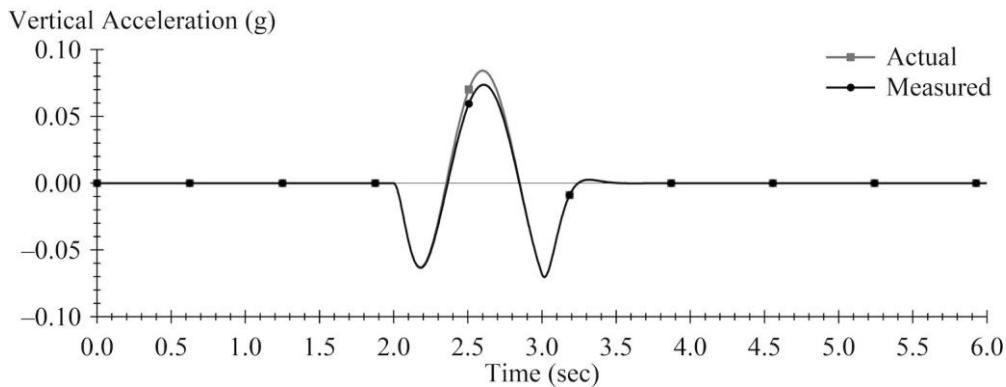
Figure 55. Graph. Measured and actual vertical acceleration.

Figure 56 shows the floating reference height derived from the accelerometer and the signal measured by the height sensor for the sensors fixed to the profiler. The error in the height-sensor signal is very small, because the change in orientation (θ) is so small that the cosine term is very close to 1. This trace correctly shows that as the profiler pitches forward the simulated profiler height sensor drew about 2 inches closer to the road surface and subsequently recovered to its nominal position.
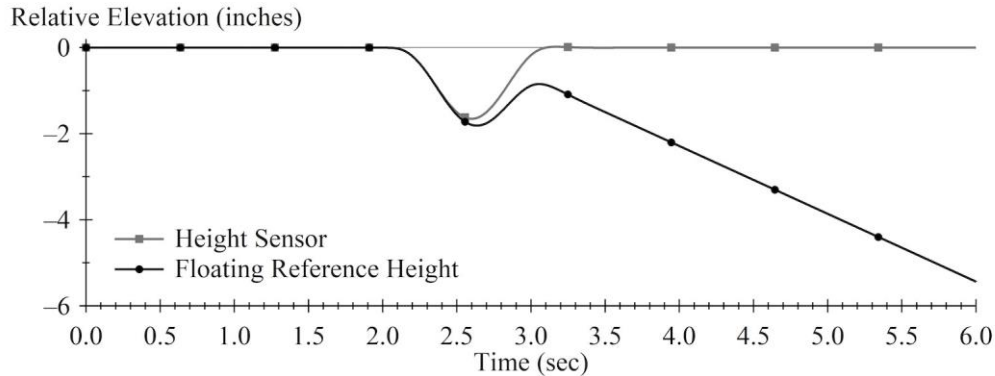
Figure 56. Graph. Height-sensor and floating-reference-height signals.

In figure 56, the floating-reference-height signal is obtained by double-integrating the accelerometer signal. It should show downward motion of the profiler followed by a recovery to its nominal position. Since the simulated road is perfectly flat, the floating-reference-height signal and the height-sensor signal should cancel. They do not, because the floating-reference-height signal includes downward curvature during the deceleration pulse. The curvature is the result of the downward bias in the accelerometer signal after double integration. Since the bias was caused by contamination of the vertical acceleration measurement, it is not canceled by the height-sensor signal.

Figure 57 shows the profile calculated using sensors fixed in the profiler host-vehicle body. The final profile is calculated by: (1) subtracting the height-sensor signal from the floating-reference-height signal, and (2) applying a high-pass filter. Misalignment of the accelerometer and cross contamination of its readings caused the profile to include an artificial bump over 0.2 inches high. The severity of the bump depends on the severity of the deceleration pulse, but its width depends on travel speed. Figure 57 shows the profile for deceleration from 49.2 mi/hr to 44.8 mi/hr, which is a small net speed change. A profiler with ideal sensors that provide true vertical acceleration and true vertical range between the profiler and the road would produce a flat profile.

Profile (inches)
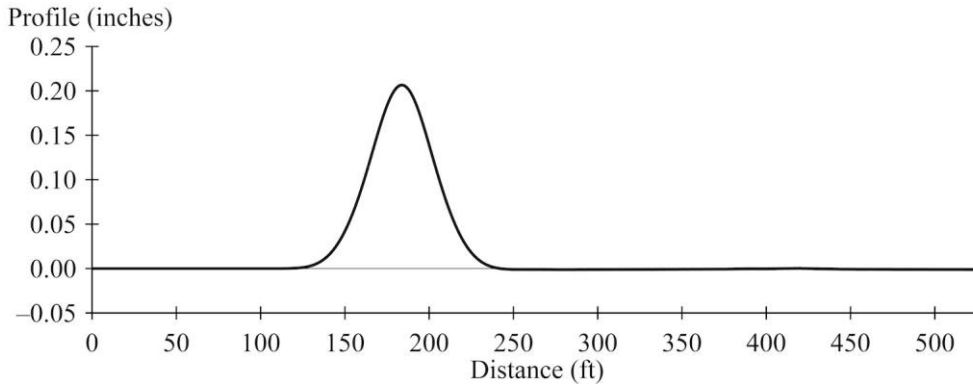
Figure 57. Graph. Simulated profile measurement.

The severity (and shape) of the bump also depends on a combination of the dynamic properties of the profiler host vehicle and the duration of the pulse. This is because the error in vertical acceleration is equal to the product of the sine of the orientation angle and the longitudinal acceleration at every instant. Therefore, a lag between the application of longitudinal acceleration and the response may reduce the error.

For the specific conditions illustrated in figure 54 through figure 57, the artificial bump causes the 0.1-mile-section that contains it to have an IRI value of 2.4 inches/mi, rather than the correct value of 0. This is not a large value, but the deceleration pulse was very short, and the net speed change was low. Further, the erroneous roughness is localized. Figure 58 shows the short-interval roughness profile.

Short-Interval Roughness Profile (inches/mi)
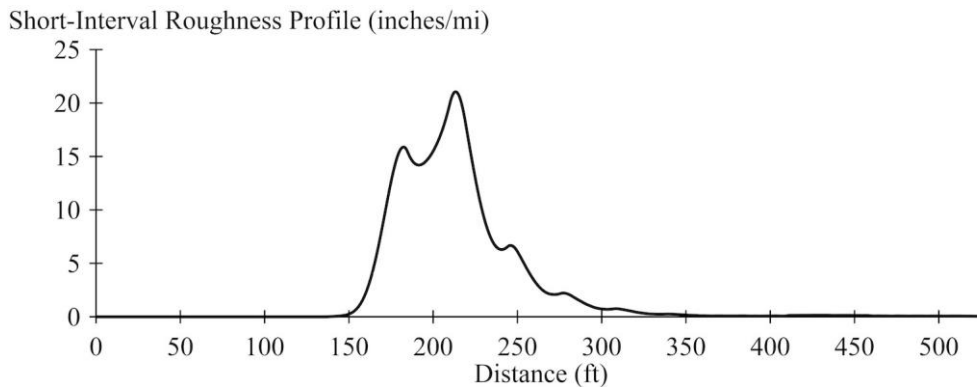
Figure 58. Graph. Short-interval roughness profile, simulated braking.

An upward bias in roughness of 2.4 inches/mi does not necessarily occur when the artificial bump is superimposed on a profile with actual roughness. The artificial bump may cancel if some negative content (i.e., a dip) appears in the location where the deceleration occurred.

Forward acceleration of the host vehicle also superimposes an artificial bump onto the measured profile. During forward acceleration, the vehicle pitches rearward. The combination of positive longitudinal acceleration (a_{xp}^{w}) and negative pitch (θ) causes a temporary negative bias in the measured vertical acceleration. (See the first term after the equal sign for a_{zp}^{b} in figure 41.) After double integration, this appears in the profile as a bump.

37

Figure 59 shows a pair of field profile measurements from a previous research project that illustrates the introduction of an artificial bump into the profile when the host vehicle experiences a deceleration pulse.[14] The figure shows a profile measured at constant speed and another profile that included deceleration with the speed profile shown in figure 60. The vehicle decelerates from about 49 mi/hr to about 23 mi/hr, including about 3.75 seconds of deceleration over 0.25 g. This type of deceleration event may occur in an urban environment if the profiler is cut off or suddenly encounters slower moving traffic.
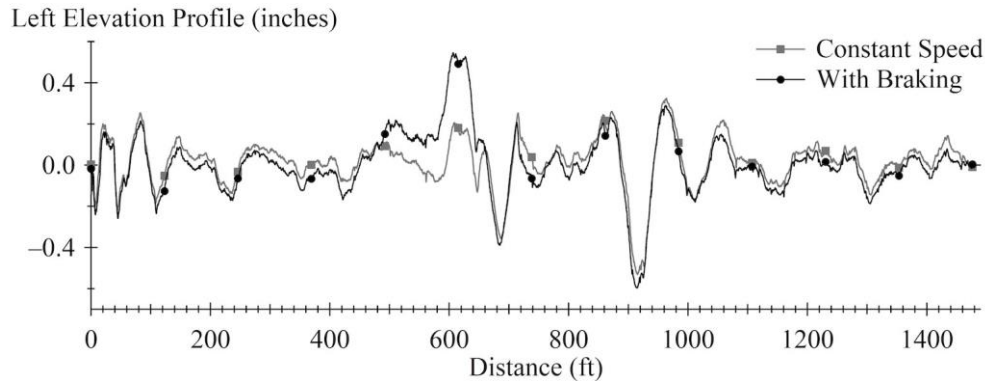
Figure 59. Graph. Profile measurement with and without braking.
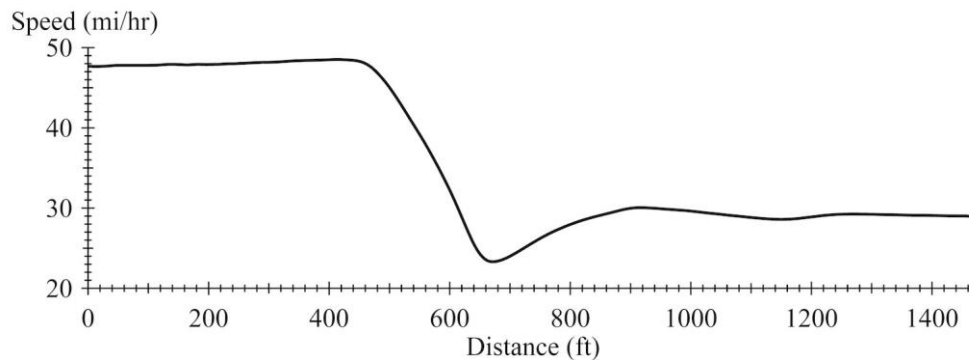
Figure 60. Graph. Test speed profile.

The deceleration causes the same qualitative erroneous profile content predicted by the kinematic analysis and modeling described above. In particular, the projection of rearward longitudinal acceleration onto the sensitive axis of the accelerometer causes a temporary downward bias in measured vertical acceleration. This in turn causes localized downward curvature in the floating-reference-height signal after double integration, which appears in the final profile. Once the profile is high-pass filtered, the localized downward curvature appears as an artificial bump.

Figure 61 shows the profile produced by the trolley simulation for a deceleration pulse similar to that shown in figure 60. (Note that, while the vehicle properties used are realistic, they are merely estimates.) The measured roughness induced by misalignment in the simulated profiler during deceleration is similar in shape and magnitude to the additional roughness that appears in the test data during deceleration. The range of deceleration appears from 150 ft to 400 ft in figure 61, and from 440 ft to 670 ft in figure 59.
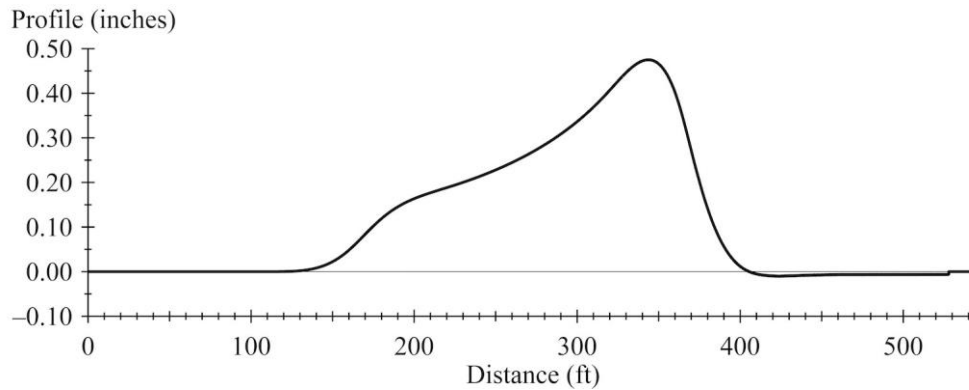
Figure 61. Graph. Simulated profile measurement error, long braking pulse.

In the simulation, the braking event adds 3.48 inches/mi of roughness to a perfectly smooth 0.1-mile-long section. At lower initial speeds, the severity of the roughness for the same deceleration history is much larger. For example, with an initial speed of 25 mi/hr, the artificial bump is more than 8 inches high and adds roughness of 116 inches/mi to a 0.1-mile segment. The increase occurs because: (1) at lower speed, the artificial roughness is more localized, and (2) the erroneous content maps to a range of wavelengths that affect the IRI to a greater extent.

Chapter Summary

The standard inertial profiler design uses body-fixed measurement of vertical acceleration to establish the floating reference height. Errors in the floating reference height occur during longitudinal and lateral acceleration, because the pitch and roll response of the host vehicle cause the sensitive axis of the accelerometer to tilt. As a result, the measured vertical acceleration is contaminated by acceleration along the other axes. This is a powerful source of error because it occurs in the frequency range where the height-sensor signal and accelerometer signal interact to cancel the effect of host-vehicle vertical vibration on the computed profile. Since this frequency range is linked to vehicle vertical dynamic response, it is also in the frequency range that affects the IRI. This chapter demonstrated this error source and the resulting error in profile and the IRI analytically and provided an experimental example. Chapter 5 proposes algorithms that suppress the error caused by accelerometer tilt by removing drift in integrated accelerometer signals.

This chapter recommends the use of vertical acceleration in the direction aligned with gravity in place of body-fixed vertical acceleration to eliminate the errors caused by accelerometer tilt. The chapter presents kinematic equations for using body-fixed measurements of acceleration and orientation of the host vehicle in three dimensions to derive the true vertical acceleration. This is the motivation for the design and fabrication of the measurement system described in Chapter 3, which includes the sensors needed to support the approach. This is the core of the proposed design solutions examined experimentally in Chapter 6.

This chapter establishes 2 ft to 141 ft as the wavelength range of interest for the IRI, and 0.48 ft to 215 ft as the wavelength range of interest for general roughness measurement. These ranges serve as engineering requirement for the design solutions proposed in this research. The chapter recommends profile and roughness comparison as the means to assess the relative success of each design. Roughness values are compared using the average IRI over a 0.1-mile-long road

section, and peak values from short-interval roughness profiles. Profiles are compared by cross correlating the output of the algorithm used to calculate IRI. Cross correlation of 0.92 is required for adequate profile agreement, and 0.98 is required to demonstrate reference-grade performance.

CHAPTER 3. SYSTEM DESCRIPTION

This chapter describes a custom measurement system that was designed and built for this research. The system was designed to enable an experimental demonstration of profile measurement errors that occur at low speed, during braking, and at stops; and an investigation of the efficacy of methods proposed in this research to eliminate those errors. The measurement system was designed to support the research in three ways.

First, the system included, at its core, the sensors that appear in a typical inertial profiler. Profiles produced using only the those sensors and the standard processing algorithms provided a basis for comparison to profiles produced using additional sensors and the methods proposed in this research.

Second, the system stored output signals from each sensor for post-processing, which is not typical for inertial profilers. Detailed sensor signals were needed to assess sources of measurement error systematically. Storage of sensor signals was also needed to support the development and evaluation of novel processing algorithms proposed in this research for reducing measurement errors, particularly those that could not be applied in real time.

Third, the system included additional sensors that provided three-dimensional measurement of profiler host-vehicle kinematics. The sensors included body-fixed measurement of acceleration and rotation rate in three dimensions, and GPS measurement of height, vertical velocity, pitch attitude, and roll attitude. These sensors provided the means to resolve the component of profiler reference point acceleration into a truly vertical direction, which was needed to eliminate the primary source of measurement error that occurs at low speed, during braking, and at stops.

The system description includes: an overview of the system, a description of its physical layout, a list of the sensors and their specifications, and a short explanation of the way signals are recorded and synchronized.

SYSTEM OVERVIEW

This section provides an overview of the measurement system, and explains the rationale behind specific design specifications described in the following sections.

Nominal Inertial Profiler

A nominal set of inertial profiler sensors are installed on each side of the vehicle. Each set of sensors includes servo-type accelerometers, ranging lasers, and a rotational encoder. The accelerometers and height sensors are aligned laterally with the host-vehicle wheels on each side. These are design elements that appear on commercial inertial profilers.

This research is concerned with measurement errors related to operation at low travel speed, during braking, and at stops. As such, the nominal system is designed to reduce other common sources of measurement error that might confound the results. For example, the accelerometers and lasers are mounted rigidly to the host vehicle to avoid excessive vibration. A rigid plate

mounted directly to the frame at the rear of the host vehicle provides a system backbone, and rigid sensor pods are attached to it on each side.

The nominal profiler uses aviation-grade accelerometers, which were selected for their accuracy, precision, and low noise floor. The nominal profiler on each side also includes a line laser for measurement of the range to ground. Line lasers detect the road surface using a wide footprint, which helps distinguish changes in elevation of the road surface that occur over a wide area from road surface texture, narrow longitudinal cracks and joints, and other narrow gaps in the road surface.[75]

A typical production profiler measures travel distance using a rotational encoder mounted to one wheel. The nominal profiler designed for this research includes rotational encoders mounted to the rear wheels on each side. This provides a specific longitudinal distance measurement to the profiler on each side without the bias associated with driving on a curve.

Three-Dimensional Kinematics

This research proposes using profiler vertical acceleration in a direction aligned with gravity in place of body-fixed vertical acceleration as a way to reduce errors in profile measurement that occur in typical inertial profilers. To do that, the system combines body-fixed measurements of acceleration and rotation.

Resolving readings from the profiler accelerometers into an axis system fixed in the Earth requires measurement of horizontal acceleration. Servo-type accelerometers fixed in each sensor pod provide body-fixed longitudinal acceleration of the left and right side profilers. An inertial navigation system (INS) fixed to a central pod between the two profilers provides body-fixed lateral acceleration.

The system obtains body-fixed yaw rate using the INS, and it obtains pitch and roll rotation rate using fiber-optic gyroscopes mounted to the center pod. The fiber-optic gyroscopes are needed have better accuracy and time stability than the microelectromechanical angular rate sensors in the INS.

The system also includes measurement of pitch and roll attitude of the host vehicle by a GPS-based system. This system measures pitch and roll by comparing the height of a GPS antenna placed at the rear of the vehicle on the left side to the height of antennas placed forward and rightward of it, respectively. These antennas were placed as far apart as possible to reduce the influence of errors in height on the derived attitude angles.

The GPS-based system is included to provide valid absolute measurements of orientation as a check on the drift that occurs when integrating measured rotation rate. In particular, this research proposes the use of the gyroscopes for measuring high-frequency content, and the GPS-based attitude measurements for low-frequency content. The GPS-based attitude measurements also provide a way to initialize the estimates of pitch and roll that are produced by integrating measurements of rotation rate.

Longitudinal Distance Measurement

Typical inertial profilers measure longitudinal travel distance using a rotational encoder mounted to a host-vehicle wheel. This method of distance measurement is prone to bias caused by changes in tire rotation speed, tire temperature, and tire inflation pressure.[14] Further, the calibration factor that relates travel distance to wheel rotation during constant-speed operation is not valid when application of the brakes or the throttle cause a change in longitudinal slip. An optical fifth wheel is installed in the center pod to provide a measurement of longitudinal distance that is not prone to these error sources.

As a check on the encoder-based and optical distance measurements, travel distance was also monitored using wheel speeds from Controller Area Network (CAN) bus messages and derived from latitude and longitude measured by a differential GPS system.

Diagnostics

The system includes several elements intended to help explain observations from the subsystems described above, and to help ensure that critical sensors are providing valid readings. This includes: (1) a video-based lane tracking system, (2) a forward-looking camera, (3) a downward-looking camera, (4) a laser for range to the road from the left front corner of the vehicle, and (5) comprehensive outputs from the inertial navigation system (e.g., angular rates, velocity, heading, etc.).

The system also includes point lasers in parallel with each line laser. The point lasers have a very small footprint relative to the line lasers, and are more prone to high-frequency noise on pavements with coarse surface texture. However, point lasers of this type have a longer history in road profiling applications and are less prone to errors caused by variations in surface reflectivity. As such, the point lasers are included for redundancy.

Signal Timing

The accuracy of profiles produced by the processing algorithms proposed in this research depends on accurate signal timing. This is true of the nominal inertial profiler sensors, because the accelerometer signals and height-sensor signals are combined to cancel the influence of host-vehicle vibration. This is equally critical in the augmented sensor configuration proposed in this research, because a Kalman filter combines outputs from the accelerometers, rate gyroscopes, and GPS to estimate the signals needed to obtain valid profile.

PHYSICAL LAYOUT

Figure 62 and figure 63 show the system in the side and rear view, respectively. The system host vehicle is a 2008 GMC Savanna Cargo Van, VIN number 1GTGG25C481234303. The host vehicle has a wheelbase of 135 inches, a track width (front and rear) of 67.8 inches, an overall length of 224.1 inches, and a height of 81.6 inches. With the instrumentation installed, the vehicle's rear overhang is increased by 9.5 inches and the overall height of the system is 100 inches. The interior rearward of the front seats was stripped to accommodate the data acquisition system (DAS), the power supply, tools, and racks for storage of the rear sensors and

mounting racks during transport. When the vehicle is fully instrumented, but unoccupied, it weighs 7080 lbs.

Figure 62. Image. Measurement system, side view.

Figure 63. Image. Measurement system, rear view.

Figure 64 and figure 65 provide schematics of the system. Figure 64 shows the top view of the hardware mounted at the lower rear of the vehicle. At the lower rear, three sensor pods are attached to a silver mounting plate, which serves as their "backbone." This assembly remains intact when the system is disassembled for storage. The silver plate attached to a black mounting plate, which is in turn attached directly to the host-vehicle frame rails. The rear bumper is removed. Figure 65 shows the front point laser, the windshield cameras, the rear wheel encoders,

and the upper rack for mounting GPS antennas. Appendix B provides several photographs of the hardware.

left pod:
    accelerometers (X and Z)
    point laser
    line laser

right pod:
    accelerometers (X and Z)
    point laser
    line laser

mounting plate (to frame)

mounting plate
(pod backbone)

center pod:
    rate gyroscopes (pitch and roll)
    optical fifth wheel
    INS

upper rack support

upper rack support
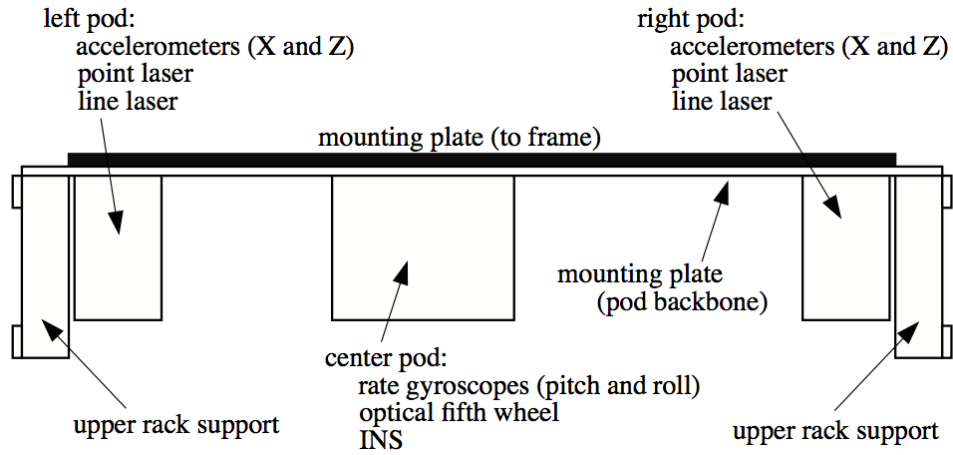
Figure 64. Schematic. Lower sensor rack, top view.
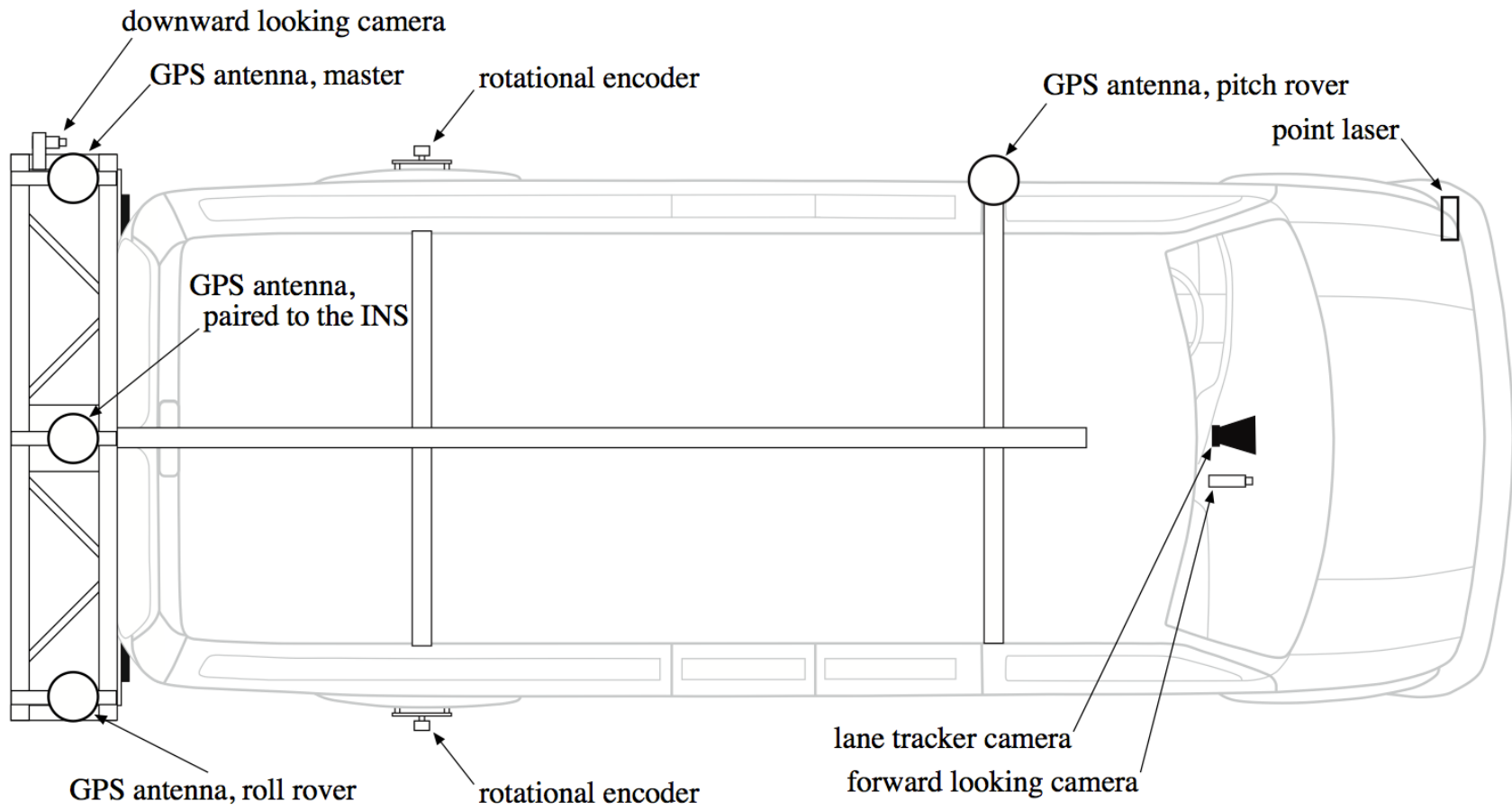
Figure 65. Schematic. System top view.

Outer Pods

Each of the left and right sensor pods carries a point laser, a line laser, a vertically oriented servo-type accelerometer, and a longitudinally oriented servo-type accelerometer. The pods are symmetric about the longitudinal centerline of the vehicle, and the sensors are mounted so that the left and right side profilers are 67.75 inches apart, which aligns them with the center of contact of the rear tires. Figure 66 shows the layout of the right pod in the rear and side view. The side view is shown without the right enclosure plate.
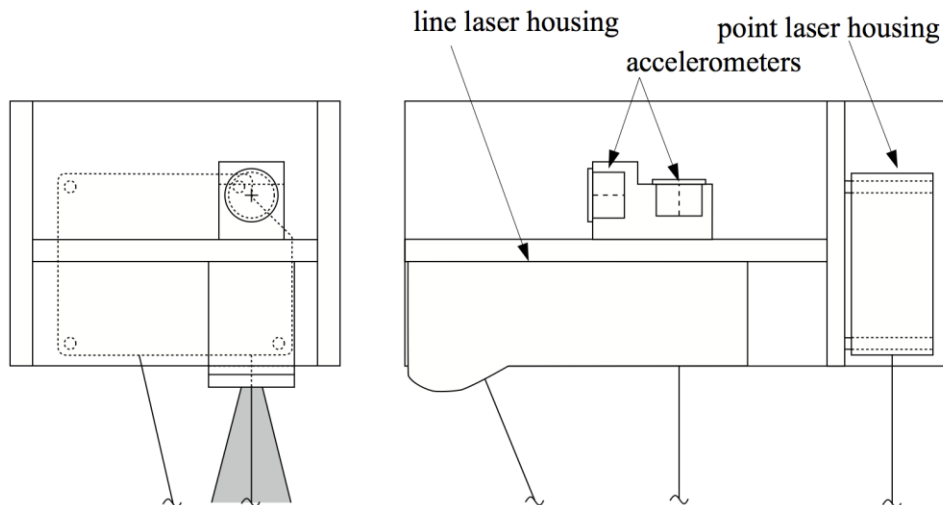
Figure 66. Schematic. Right sensor pod.

The line lasers project light over a transversely oriented line more than 4 inches wide, with the detector rearward of the projected light source. Each line laser is mounted so that the center of the light that it projects is aligned with the sensitive axis of its companion accelerometer. The point lasers project light onto the ground over a diameter of 0.012 inches. The point lasers are aligned transversely with the line laser and accelerometers. Their footprint is 4.12 inches forward of the line lasers, and they are mounted with the detectors inboard of the light source. When the vehicle is at rest, the line lasers have an approximate range to ground of 11.1 inches and a triangulation angle of 22 degrees. The point lasers have an approximate range to ground of 11.4 inches and a triangulation angle of 13 degrees.

The longitudinal accelerometers are installed just rearward of the vertical accelerometers within the same mounting blocks.

Center Pod

The center pod carries two rate gyroscopes, an INS, and an optical fifth wheel. Figure 67 shows the layout of the center pod in the rear and side view. The side view is shown without the right enclosure plate.
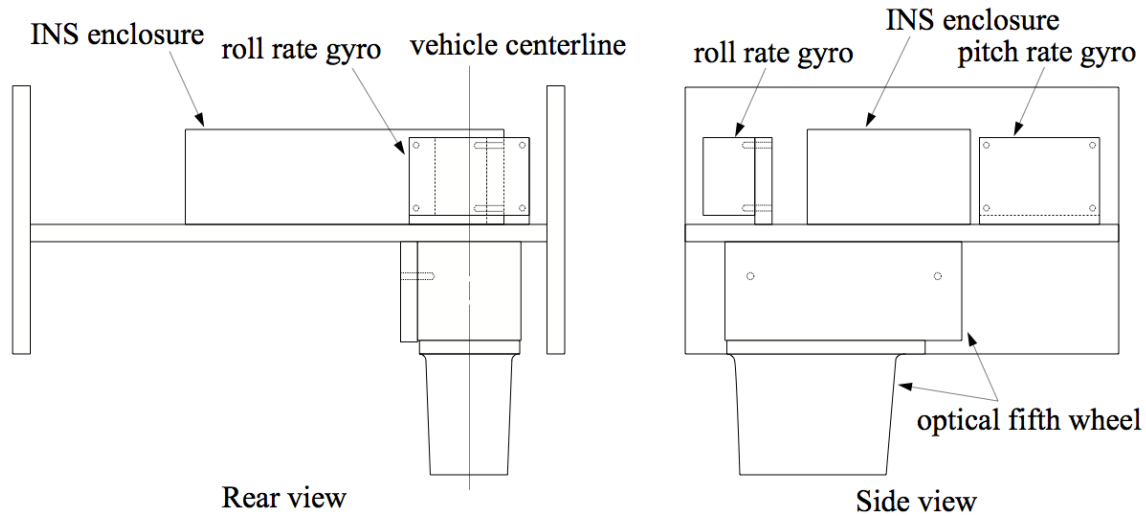
Figure 67. Schematic. Center sensor pod.

The rate gyroscopes are mounted along the host-vehicle longitudinal axis of symmetry. One of the gyroscopes is oriented for measurement of profiler pitch rotation rate, and the other is oriented for measurement of profile roll rotation rate. The integrated signals provide relative pitch and roll rotation. An optical fifth wheel is mounted to the underside of the center pod for measurement of longitudinal distance. The center pod also houses the main enclosure for the INS, which contains three accelerometers and three angular rate sensors.

Upper Instrumentation Rack

The upper instrumentation rack carries three GPS antennas for measurement of host-vehicle sprung-mass pitch and roll. (See figure 65.) The master antenna is mounted at the left rear corner. A rover antenna is mounted forward of it for measurement of pitch; and another rover antenna is mounted beside it for measurement of roll. When the vehicle is at rest, the three antennae form a plane that is about 97 inches above the ground. The pitch antennae are 132 inches apart, and the roll antennae are 78.7 inches apart.

The upper instrumentation rack also houses a GPS antenna at the center rear, which is used by the INS to eliminate drift in its calculation of position and velocity.

Other Sensors

As shown in figure 65, the system includes several additional sensors:

- Rotational encoders are mounted to each of the vehicle rear wheels.

- A point laser measures range to ground at the front left corner of the vehicle chassis.

- A forward-looking camera is mounted inside the windshield.

- A downward-looking camera is mounted to the left side of the upper instrumentation rack. The field of view includes the rear quarter of the vehicle's left side, the pavement beside it, and a portion of the roadside.

- An optical lane tracker system is mounted inside the windshield.

Although it is not shown in the diagrams, the system also records wheel speeds and other pertinent quantities (transmission status, cruise control, brake light switch, throttle position, etc.) from CAN bus messages.

SENSORS

Table 7 identifies each sensor by model number and serial number. The list that follows includes pertinent specifications of each sensor as they were used in this measurement system.

Table 7. System sensors.

Sensor Position	Make and Model Number	Serial Number
Left point laser	LMI Selcom SLS5200/300-RO	1002
Right point laser	LMI Selcom SLS5200/300-RO	2362
Front point laser	LMI Selcom SLS5000-200/300-RO	N2297
Left line laser	LMI Selcom Gocator 2342A-3B-12	00022133
Right line laser	LMI Selcom Gocator 2342A-3B-12	00022135
Left vertical accel.	Honeywell Q-Flex QA1400-AA03-0	459
Left longitudinal accel.	Honeywell Q-Flex QA1400-AA03-0	451
Right vertical accel.	Honeywell Q-Flex QA1400-AA03-0	438
Right longitudinal accel.	Honeywell Q-Flex QA1400-AA03-0	460
Left encoder	BEI XHS25-75-R2-SS-2048	QQ110792
Right encoder	BEI XHS25-75-R2-SS-2048	QQ110791
Optical fifth wheel	Datron DLS-2	06.303
Pitch rate gyro.	KVH DSP-3000 Fiber optic gyro 02-1222-01	RD 16610
Roll rate gyro.	KVH DSP-3000 Fiber optic gyro 02-1222-01	RD 20917
INS	Oxford Technical Solutions RT3050	073
GPS antenna, INS	Novatel GPS-600-SB 01017062	NTM03230018
GPS antenna, master	Novatel GPS-702-GG 01017577	NAE12100014
GPS antenna, pitch rover	Novatel GPS-702-GG 01017577	NAE12100009
GPS antenna, roll rover	Novatel GPS-702-GG 01017577	NAE12100016
GPS receiver, master	Novatel Flex6-G2L-R0G-55R	NKC12240013
GPS receiver, pitch	Novatel Flex6-G2L-B0G-55R	NKC12240021
GPS receiver, roll	Novatel Flex6-G2L-R0G-55R	NKC12240014
Lane tracker	MobilEye C2-270	
Front camera	B&H EVEMC700	
Rear camera	B&H EVEMC700	

The GPS-based attitude measurements were provided by a Novatel Align system, including a RavenX modem for receiving Radio Technical Commission for Maritime (RTCM) correction data from Networked Transport of RTCM via Internet Protocol servers. The INS combines measurements of acceleration, angular rate, and GPS position using Kalman filtering to estimate motion outputs. The specifications below are those listed for the RT3050 once the filter has converged. The actual outputs provide estimates of the probable error level with each set of readings.

Vertical Accelerometers

Range: 4 g (+/– 2 g)

Resolution: 0.001076 g left, 0.001095 g right

Bandwidth: to 2,000 Hz

Sample rate: 16,000 Hz

Longitudinal Accelerometers

Range: 2 g (+/– 1 g)

Resolution: 0.000543 g left, 0.000544 g right

Bandwidth: to 2,000 Hz

Sample rate: 16,000 Hz

Point Lasers

Range: 7.9 inches (+/– 3.9 inches)

Resolution: 0.004 inches left, 0.004 inches right, 0.005 inches front

Bandwidth: to 2,000 Hz

Sample rate: 16,000 Hz

Line Lasers

Range: 7.9 inches (+/– 3.9 inches)

Vertical Resolution: 0.00016 inches

Horizontal Resolution: ~400 readings over a 4-inch width at stand-off

Sample rate: ~3,240 Hz

Encoders

Resolution: 2048 cycles per rev quadrature (8192 counts per revolution, which is 0.012 inches per count)

Sample rate: recorded at 250 Hz

Optical Fifth Wheel

    Velocity resolution: 0.0089006 ft/s

    Velocity bandwidth: to 2000 Hz

    Position resolution: 0.089 inches

    Position sample rate: recorded at 16,000 Hz

Rate Gyros

    Range: full scale +/– 375 deg/sec

    Resolution: 0.000001 deg/sec

    Bandwidth: to 100 Hz

    Sample rate: 100 Hz

GPS Position (when real-time kinematic (RTK) integer fix is possible)

    Sample rate: 20 Hz

    Accuracy: 0.4 inches + 1 ppm of distance to base station

GPS Velocity

    Sample rate: 20 Hz

    Accuracy: 0.098 ft/s RMS

GPS Heading and Pitch

    Sample rate: 20 Hz

    Accuracy: 0.06 deg

GPS Roll

    Sample rate: 20 Hz

    Accuracy: 0.1 deg

MobilEye Lateral Lane Position

    Sample rate: asynchronous

    Resolution: 0.013 ft

Downward and Forward Cameras

    Sample rate: 30 images per second

    Resolution: 720x480

Update rate: 100 Hz

Position Accuracy: 2-inch probable circular error

Velocity Accuracy: 0.5 mi/hr RMS

Acceleration bias: 0.001 g at one st. dev.

Roll/pitch: 0.04 deg at one st. dev.

Angular rate: 0.01 deg/s at one st. dev.

SIGNAL FLOW

The measurement system includes a diverse set of sensors and cameras, with diverse outputs and timing. Some sensors provide serial outputs, some provide Ethernet outputs, some provide analog outputs, and others output counter values and digital signals.

Data logging is performed by an embedded system including: a host central processing unit (CPU), a secondary CPU, a counter/timer card, an A/D card with high-speed digital inputs, a dual channel CAN bus interface, and a video frame grabber. The A/D card is connected to a custom 8 channel analog signal conditioning chassis.

Synchronization of data from various sources is done in both distance and time. Temporal synchronization is done using constant monitoring of a common time signal by most sensors, and monitoring of a common pulse by others. The system records a reference time from a CPU clock with every video image, and every sample from the accelerometers, point lasers, rate gyroscopes, INS, lane tracker, and GPS receivers. The A/D card also outputs a pulse every 4 seconds. The pulse appears in the outputs from each line laser and the high-speed outputs from the accelerometers and point lasers. This provides a way to reconcile the internal clocks from each line laser with the common clock used by most of the rest of the system. For redundancy, a synchronization output from each frame recorded by the line laser is monitored synchronously with the 16,000 Hz outputs from the accelerometers and point lasers.

For spatial synchronization, the system records counts from the optical fifth wheel and both rotational encoders every 4 milliseconds using the CPU clock; as described above, these counts are also synchronized in time with GPS position. The system also routes rotational encoder counts to each liner laser. The vehicle odometer, while low in resolution, is logged over the CAN interface.

CHAPTER 4. NOMINAL SYSTEM PERFORMANCE

This chapter characterizes the performance of the nominal inertial profiling system mounted on the left side of the host vehicle. This system includes measurement of vertical acceleration by a servo-type accelerometer, measurement of range to ground by a line laser, and measurement of longitudinal distance by a rotational encoder mounted to the left rear wheel. System performance is characterized using stationary testing, profile measurement repeatability, and agreement to a reference profile measurement.

STATIONARY TESTING

Stationary testing was performed at the start of each test day to verify basic system health and vertical calibration, as described in AASHTO R 57-14.[92] In a stationary test, profile data are collected with the engine on and the vehicle parked on a flat, level platform. Longitudinal motion is simulated using an artificial distance encoder signal, which progresses at a constant rate. The results described here correspond to a simulated travel speed of 45 mi/hr. In all stationary tests, a clipboard was placed under each laser sensor to reduce the effect of surface texture on measurements of range to ground.

Stationary tests provide an efficient way to identify excessive noise, sensor malfunctions, poor sensor calibration, and signal processing errors in the field. Since the elevation of the road surface beneath the profiler remains constant throughout stationary tests, a perfect system would measure a flat profile and register no roughness. Two types of stationary tests were performed: quiescent tests and bounce tests.

Quiescent tests are typically performed with the engine on and no additional motion imposed on the vehicle chassis. The primary purpose of the quiescent test is to characterize the level of sensor noise that appears as artificial roughness in the measured profile. AASHTO R57-14 deems an IRI of 3 inched/mi or less acceptable for a quiescent test.[92]

In most cases, quiescent tests on the nominal inertial profiling system produced profiles with IRI values below 0.6 inches/mi. These profiles included evidence of sensor noise and imperfect cancelation of profiler motion caused by engine vibration. Roughness caused by engine vibration appeared at a simulated wavelength of 4.8 ft, which corresponds to an engine speed of 820 rpm (13.7 Hz). In specialized quiescent tests with the profiler removed from its mounts and supported by a rack (and the engine on), the roughness reduced to 0.25 inches/mi. With the engine off and the profiler mounted to the vehicle, quiescent tests produced profiles with IRI values near 0.3 inches/mi.

During a bounce test, the operator moves the profiler vertically by exercising the host-vehicle suspensions in jounce and rebound. A standard bounce test includes several seconds of quiescent operation followed by several seconds of induced vertical motion. Ideally, the cyclic changes in profiler reference height detected by the accelerometer would be perfectly canceled by equal changes in relative range to ground measured by the height sensor. AASHTO R57-14 deems an IRI of 8 inches/mi an acceptable level for a bounce test.[92]

Figure 68 shows a short-interval roughness profile produced by a bounce test using the nominal inertial profiling system. In this case, the induced motion took place over an interval of 6.5 seconds, which corresponds to a distance of approximately 430 ft at the simulated test speed. During the middle two thirds of the induced motion, the profiler moved downward 2.2 inches and upward 1.2 inches from its static position at a frequency very close to 2 Hz.
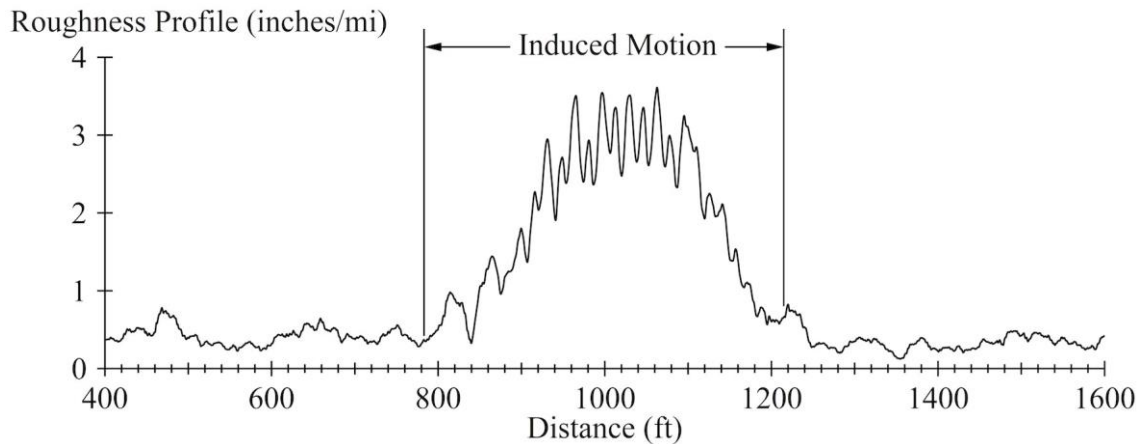
Figure 68. Graph. Short-interval roughness profile produced by a bounce test.

Artificial roughness appeared in the measured profile with amplitude of 0.004 inches and a wavelength of 33 ft due to imperfect cancelation of the vehicle motion between the height-sensor signal and the floating-reference-height signal. As shown in figure 68, the average IRI was 3 inches/mi when the induced motion was at its most severe, which is well below the threshold value of 8 inches/mi. The low roughness value over this interval is strong evidence that the sensors are functioning, are properly calibrated, and are stored with consistent signal timing. During the quiescent portions of the test, the IRI was 0.4 inches/mi. The low quiescent roughness value demonstrates a low level of system noise.

DYNAMIC TESTING

Test Section

Dynamic testing took place on the low volume loop at the Minnesota Road Research Facility (MnROAD) research facility near Albertville, MN. This is the same site where testing was conducted with staged reproductions of common operational conditions encountered during network-level profile measurements on low-speed and urban roadways, such as: (1) operation at low speed, (2) acceleration or deceleration, (3) stop-and-go operation, (4) profiling from a dead stop, and (5) operation on a curve. Most of the testing took place on a tangent section running southeast along the northern straightaway on the low volume loop. The tangent section was 1503 ft long. This length was needed to observe the effects on measurement of long-wavelength content during operation at very low speed and long transient effects that occurred during acceleration and deceleration, as well as the residual effects of high-pass filter settling behavior. Most of the test section was asphalt concrete, but it included a transition to Portland cement concrete about 110 ft upstream of the section end.

Figure 69 shows the tangent section. Section starting and ending locations were marked with temporary reflective tape. Diamond shaped marks were painted 18 inches to the right of the left track of interest to help the driver maintain the lateral position of the profiler accurately and consistently. The marks were placed about 20 ft apart starting 295 ft upstream of the section and extending over its length.

Figure 69. Image. Tangent section starting point.

Reference Measurements

Reference profile measurements were collected using a SurPRO 3500 on both sections. This device recorded profile data at 1-inch intervals. The SurPRO 3500 is an inclinometer-based device that is supported by two wheels 9.8 inches apart. It is pushed along a test section at walking speed, and constructs a profile by accumulating changes in height using a series of slope values recorded at a constant longitudinal distance interval.

At the tangent section, three repeat passes were made in each wheel path. The distance between the wheel paths was 69 inches. The overall IRI of the tangent section was 112 inches/mi in the left wheel path and 111 inches/mi in the right wheel path.

Test Section Boundaries

Static GPS readings were collected over a 50-second time interval with the receiver on the pavement surface at the test section boundaries. On the tangent section, the receiver was placed at the intersection of each wheel path of interest with the longitudinal center of the start and end stripe. Table 8 lists the mean latitude, longitude, and height above sea level observed over 50 seconds for the left and right side of the lane at the start and end of each test section.

Table 8. Test section boundaries.

Landmark	Latitude (deg)	Longitude (deg)	Height (ft)
Tangent, Left Start	45.265437474	–93.715535338	963.235
Tangent, Right Start	45.265424849	–93.715548998	962.820
Tangent, Left End	45.262924594	–93.710912428	970.906
Tangent, Right End	45.262912107	–93.710925729	970.839

Table 9 lists the standard deviation of position and speed measurements observed over the 50-second measurement interval. Many of the probability distributions were not normally distributed. In particular, distributions of position quantities at some locations included positive excess kurtosis (i.e., thin at the center with long tails). Typically, this system applied a new position correction every 0.8 to 1.2 seconds. The largest step changes in position quantities and larger speed values often corresponded to a recorded sample with a fresh position correction. Noise observed in the position quantities from this source was often correlated among the position signals (latitude, longitude, and height).

Table 9. Static measurement noise.

Landmark	Latitude (deg)	Longitude (deg)	Vertical Speed (ft/s)	Horizontal Speed (ft/s)	Height (inches)
Tangent, Left Start	3.02×10^{-8}	6.00×10^{-8}	0.544	0.098	0.75
Tangent, Right Start	1.40×10^{-8}	1.77×10^{-8}	0.157	0.036	0.16
Tangent, Left End	4.79×10^{-8}	5.47×10^{-8}	0.215	0.077	0.26
Tangent, Right End	1.46×10^{-8}	1.73×10^{-8}	0.175	0.035	0.17

At this location, an increase in latitude of 10^{-8} deg corresponds to a shift northward of 0.044 inches, and a change in longitude of 10^{-8} deg corresponds to a shift eastward of 0.031 inches.

Local Coordinates

Measurements of latitude and longitude collected by the master GPS antenna were transformed to local Cartesian coordinate systems with axes aligned eastward, northward, and upward. On each section, the origin was placed at the intersection of the left wheel path with the starting stripe. Locations north (dN) and east (dE) of the section origin were calculated from instantaneous readings of latitude (ϕ) and longitude (λ) as shown in figure 70 and figure 71.

$$dN = \left(R(\phi_0) + H_0 \right)\left(\phi - \phi_0 \right)$$

Figure 70. Equation. Northward travel from the section start.

$$dE = \left(R(\phi_0) + H_0 \right)\cos(\phi)\left(\lambda - \lambda_0 \right)$$

Figure 71. Equation. Eastward travel from the section start.

The symbols ϕ_0, λ_0, and H_0 denote the latitude, longitude, and height above sea level, respectively, at the test section origin. $R(\phi_0,)$ is an estimate of the Earth's radius at the origin. For both test sections, this was approximately 3,956.94 mi. The influence of changes in height at points away from the origin was neglected in these calculations.

Data were further transformed in the horizontal plane to distance forward dF and distance leftward dL along the section. This re-oriented the horizontal axes to include an axis (with the original origin) that passed through the left-side endpoint, as described in figure 72 and figure 73.

$$dF = dE\cos(\psi) + dN\sin(\psi)$$
$$dL = -dE\sin(\psi) + dN\cos(\psi)$$

Figure 72. Equations. Forward and leftward distance along the test section.

$$\psi = \operatorname{atan}\left(\frac{dN_{End}}{dE_{End}}\right) = -37.68 \text{ deg}$$

Figure 73. Equation. Test section orientation.

Subsequently, the coordinates were offset to provide the location of the left-side profiler instead of the position of the GPS antenna.

AGREEMENT TO THE REFERENCE

Several test runs were performed over the tangent section at various host-vehicle travel speeds to examine the influence of speed on profile measurement repeatability and agreement to the reference profile measurement. The runs included 28 passes: 3 passes at each speed in the range from 15 mi/hr to 50 mi/hr in 5 mi/hr increments, 2 passes at 10 mi/hr, and 2 passes at 60 mi/hr.

Cross correlation analysis using profile traces filtered by the IRI algorithm produced an average agreement score of 0.914 when the profiles were compared to the reference measurement. The comparisons were made over a 0.1-mile-long segment of the left wheel path. The IRI of the reference profile over this range was 115.6 inches/mi. The overall range of agreement scores for the 28 passes was 0.823 to 0.990. However, the individual agreement scores did not correlate to travel speed. Rather, agreement to the reference profile measurement was strongly influenced by errors in lateral tracking.

Unfortunately, none of the constant-speed runs tracked perfectly over the trace followed by the reference profiler. Figure 74 shows the lateral position of the left side profiler footprint relative to the reference trace for three of the runs. Local coordinates of the left profiler footprint were derived using local coordinates position of the master GPS antenna (derived using the equations in figure 70 through figure 73), GPS-based measurements of the pitch and roll attitude of the measurement platform, and the lever arm between the master GPS antenna and the left profiler footprint. The passes shown in figure 74 ran at 20 mi/hr and 50 mi/hr. Each pass followed a similar trajectory with an average of 5.5 inches left of the reference track. The agreement score for each profile was 0.949.
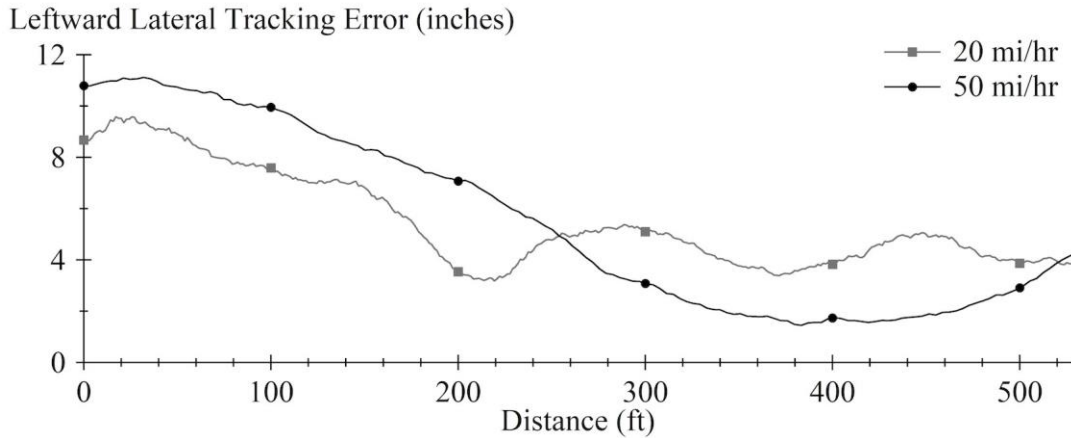
Figure 74. Graph. Leftward tracking error.

Figure 75 shows the profile agreement score versus leftward tracking bias for the 28 test runs. The figure demonstrates a strong association between leftward tracking bias and agreement score for this test section. The agreement score is above 0.98 for the three runs with an average leftward tracking error below 2.6 inches. A value of 0.98 has been proposed as the threshold for "reference quality" agreement in past studies.[75,86,93]
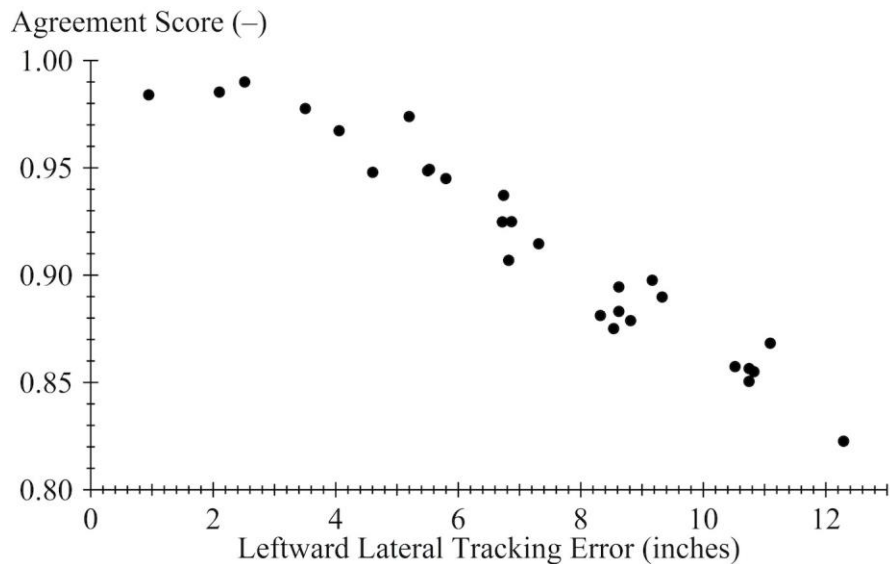
Figure 75. Graph. Agreement score versus lateral tracking error.

REPEATABILITY

For the 28 passes examined in figure 75, cross correlation analysis using profile traces filtered by the IRI algorithm produced an average repeatability score of 0.944 for the 378 permutations of two profiles from the group, with a range from 0.808 to 0.998.

Like agreement to the reference measurement, lateral tracking strongly influenced the repeatability scores. Figure 76 shows the repeatability scores versus average lateral separation. The average lateral separation is the average absolute difference in lateral position between the

paths followed by the two runs over the length of the test segment. The 14 pairs of passes with an average lateral separation of 1.2 inches or less produced repeatability scores above 0.98 with one exception (0.976). For the passes shown in figure 74, the average lateral separation was 2.0 inches, and their agreement score was 0.993.
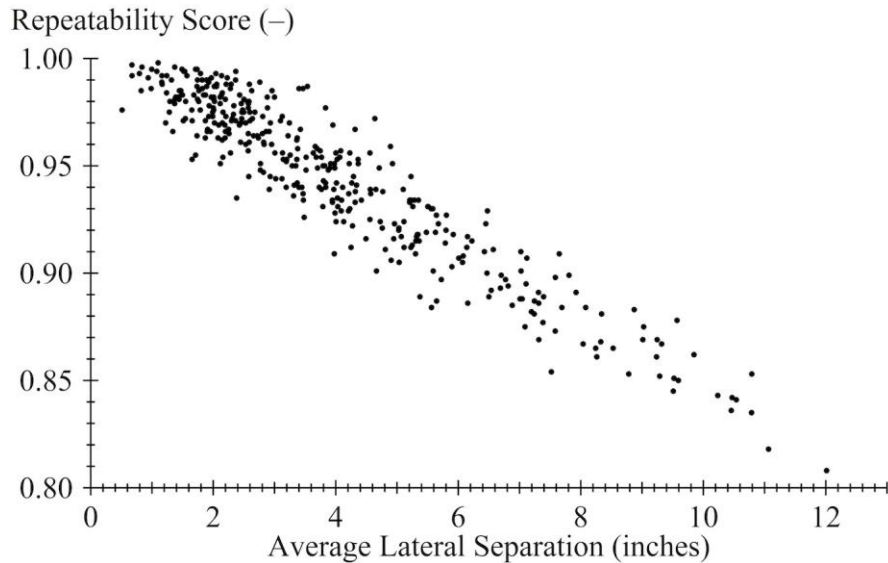
Figure 76. Graph. Repeatability score versus average lateral separation.

The results in figure 75 and figure 76 imply that production measurement of profile in two wheel paths, which is common in practice, provides only a sampling of the true roughness of a pavement section. Using a lane keeping assist system on inertial profilers is likely to improve the interpretation of changes in a pavement's roughness over time by reducing the confounding effects of inconsistent lateral tracking. Measurement of the road surface in three dimensions coupled with detection of lane edges would offer further improvement.

Measurements collected to establish the accuracy and repeatability of profilers should, at minimum, include a record of lateral position versus distance along the test section. To establish the maximum capability of the profiler sensors and processing software, the use of automated steering control is recommended. For profilers that are steered manually, clear guide marks should be provided.

CHAPTER 5. ERROR SUPPRESSION

This chapter presents algorithms for suppressing artificial localized roughness at locations where an inertial profiler host vehicle brakes, stops, or operates at low speed. The proposed error suppression algorithms operate using only the nominal profiler sensors: an accelerometer, a height sensor, and a distance encoder. That is, the proposed algorithms are designed to reduce measurement errors as much as possible on typical commercial profilers without incorporating additional sensors. Chapter 6 addresses the use of additional sensors.

Double integration of profiler accelerometer signals with slowly varying bias causes drift in the calculated vertical position of the profiler reference point. During low-speed operation and during stops, the calculated elevation change is concentrated over a small longitudinal distance and registers as roughness. The algorithms presented attempt to limit the magnitude of this change while removing as little of the profile content in the waveband of interest as possible. In particular, the algorithms reduce artificial localized roughness at stops without adversely affecting measurement of profile at host-vehicle travel speeds above 10 mi/hr.

The chapter introduces a basic temporal profile calculation algorithm and a basic spatial profile calculation algorithm, which use methods that are common in commercial inertial profilers. The proposed error suppression algorithms include additions or modifications to the basic algorithms. The performance of the basic algorithms serves as a baseline for comparison to the error suppression algorithms.

The chapter reviews the engineering requirements that influenced the design of the proposed error suppression algorithms. The chapter also describes the test conditions used to challenge each algorithm. The chapter proposes and evaluates four error suppression algorithms for use with temporal profile calculation architecture and two error suppression algorithms for use with spatial profile calculation architecture. The performance of each algorithm is characterized for test runs at low speed, during braking, and with stops. Performance is characterized by comparing profile (via cross correlation) and roughness to that of a reference run.

PROFILE CALCULATION ALGORITHMS

This chapter examines both temporal and spatial profile calculation algorithms, because both types are used in practice. Temporal algorithms calculate profile in the time domain, and then resample the profile to a constant distance interval afterward using the distance encoder signal. As such, temporal algorithms double integrate the accelerometer signal to obtain the floating-reference-height signal and combine it with the height-sensor signal in the time domain. Spatial algorithms resample the accelerometer and height-sensor signals to a constant distance interval before calculating profile. When a spatial algorithm is used, temporal signals only exist in analog form in the time domain, and the distance encoder triggers digital sampling at each distance increment. That process is simulated here on stored temporal signals using algorithms that could function in real time.

The chapter presents basic temporal and spatial profile calculation algorithms and variations on them intended to suppress artificial localized roughness during host-vehicle stops. The basic

algorithms include high-pass filtering on the profile to remove the low-frequency content. This is done in common practice because the low-frequency content is often contaminated by low signal strength in the accelerometer or slowly fluctuating accelerometer misalignment from a truly vertical orientation.

Variations on these algorithms used for error suppression include:

Mean Removal: This procedure removes the bias from the accelerometer signal prior to each stage of integration.

High-Pass Filtering, Pre-Integration: This procedure applies high-pass filtering to the individual sensor signals in addition to applying high-pass filtering to the computed profile. In particular, application of high-pass filtering to the accelerometer signal before each stage of the integration reduces drift.

Other variations on the basic temporal profile calculation algorithm specifically apply provisions for suppressing integrator drift in areas where the profiler host-vehicle travel speed passes below 10 mi/hr:

Local Suppression: This procedure augments the pre-integration high-pass filtering. It uses discrete-time proportional-integral (PI) control to suppress bias in the integrated accelerometer signal at low speed.

Adaptive High-Pass Filtering: This procedure modifies the pre-integration high-pass filtering algorithm by adapting the high-pass filter cut-off frequency as a function of host-vehicle speed. In particular, this algorithm maintains a constant cut-off wavelength in areas of high-speed operation, and transitions to a set temporal cut-off frequency as speed diminishes.

The basic spatial profile calculation algorithm offers fewer options for suppressing integrator drift, because of the long time interval associated with consecutive distance samples digitized at low host-vehicle travel speed and at a stop. In addition to high-pass filtering, variations on the basic spatial algorithm apply the following provisions in areas where the speed passes below 10 mi/hr:

Timer Distortion: This procedure artificially limits the integration time interval associated with consecutive spatial profile samples in areas of low-speed operation.

Height-Sensor Reflection: This procedure works in conjunction with timer distortion. Height-sensor reflection enforces cancelation of fluctuations in the height-sensor signal in areas where timer distortion has suppressed content within the floating-reference-height signal.

These algorithms function in typical fashion in areas where the host-vehicle speed is above 10 mi/hr. However, each suppression algorithm introduces error into the profile in areas where the host-vehicle speed is below 10 mi/hr.

The chapter compares the performance of each modification to the basic profile calculation algorithms in light of the following design objectives:

1. Reduction in the magnitude of artificial roughness caused by braking and stops: This is quantified using the peak value of the short-interval roughness profile in the area where the host vehicle stopped or released the brakes. An artificially high peak value in the short-interval roughness profile is undesirable for two reasons. First, the corresponding error in the average roughness of the overall road segment affects statistics used for pavement management and assessment of pavement network health. Second, the high peak value causes a false positive for an area of localized roughness that needs attention.

2. Valid measurement of profile and roughness at speeds above 10 mi/hr: This is quantified by comparing the average values of segment-wide roughness from runs collected at various host-vehicle travel speeds and cross correlation to profile measured under ideal conditions. A minimum threshold value for cross correlation of 0.92 is adopted from AASHTO R56-14.[87] This depends on maintaining content within the profile in the waveband of interest for the measurement of IRI. In terms of wavelength, this is 2.0 ft to 140.7 ft. (See Chapter 2.)

3. Standardized high-pass filtering: Whenever it is possible, these algorithms adhere to the high-pass filtering requirement in AASHTO M 328-14 of 3 dB reduction in gain for the wavelength range of 300 ft and above.[40] Retaining the waveband of interest for general roughness measurement (0.48 ft to 215 ft) is preferred.

4. Minimization of signal storage: The design of these algorithms prioritizes real-time analysis of sensor signals, particularly in the time domain. This minimizes the burden of storing all of the signals needed for profile computation until the end of a measurement run. To support real-time operation, these algorithms apply infinite impulse response (IIR) high-pass filters. These algorithms apply equivalent reverse-running filters to cancel the phase shift imposed in the real-time filtering stages. The reverse-running filters are applied as late in the process as possible to avoid increasing the storage burden.

The chapter describes the test conditions used to evaluate the performance of each algorithm. The sections that follow describe each algorithm and their performance in light of the design objects listed above. The description of the basic temporal profile calculation algorithm includes an illustrative example of drift in the floating-reference-height signal from a run that included a stop.

TEST CONDITIONS

The error suppression algorithms examined in this chapter are evaluated using test runs collected on the tangent section at MnROAD. (See figure 69.) The test runs include seven staged stop-and-go runs, a near stop with movement at low speed for a short time, seven runs with braking (but no stop), and two passes at low speed. These runs were selected to challenge the performance of the proposed algorithms as much as possible.

During each stop-and-go run, the host vehicle entered the test section with cruise control set at approximately 45 mi/hr, decelerated to a stop near a designated landmark, remained still for a short time interval, then accelerated to a target speed of 36 mi/hr. Figure 77 shows the temporal speed profile from one of these runs, and figure 78 shows the spatial speed profile. In this run the

average deceleration of the host vehicle over the speed range from 43.8 mi/hr to 0.3 mi/hr was 0.20 g. The profiler stopped 710.3 ft from the test section starting location and remained stopped for 10.7 seconds. Table 10 describes each of the seven stop-and-go runs by average deceleration, stop duration, and stop location. The table also provides a designation used to identify each run in tabulated results throughout the rest of this document.
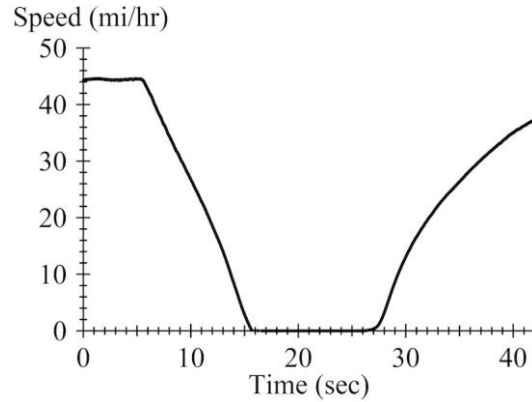
Figure 77. Graph. Stop-and-go run temporal speed profile.
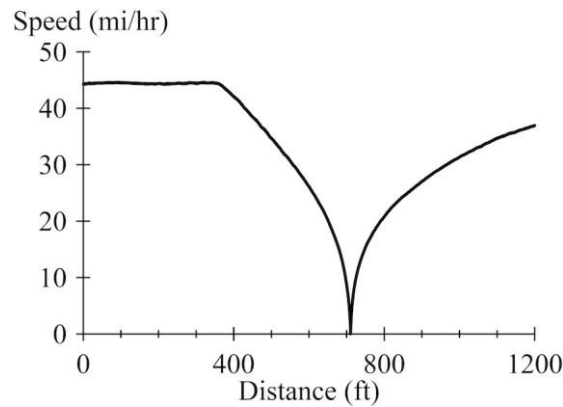
Figure 78. Graph. Stop-and-go run spatial speed profile.

Table 10. Stop-and-go run characteristics and designations.

Designation	Average Decel. (g)	Stop Duration (sec)	Stop Location (ft)
S&G, 1.1-sec stop, 0.17 g	0.171	1.07	705.8
S&G, 1.1-sec stop, 0.20 g	0.203	1.12	708.8
S&G, 2.1-sec stop, 0.33 g	0.329	2.10	710.7
S&G, 5.8-sec stop, 0.17 g	0.167	5.77	703.9
S&G, 5.7-sec stop, 0.20 g	0.202	5.69	706.8
S&G, 5.8-sec stop, 0.20 g	0.201	5.78	710.3
S&G, 10.7-sec stop, 0.20 g	0.200	10.70	710.3

In the pass with a near stop, the host vehicle entered the test section with cruise control set at approximately 44.5 mi/hr, reduced its speed to 7.1 mi/hr with an average deceleration of 0.196 g,

63

coasted for 2.19 seconds, and then accelerated to 36 mi/hr. The coast occurred while the profiler passed over a range from 705.6 ft to 724.6 ft from the test section start.

During each "braking run" (i.e., run with braking but no stop), the host vehicle entered the test section traveling at a constant speed, applied the brakes to slow to a lower target speed, and continued to the end of the test section at the new target speed. Figure 79 shows the temporal speed profile from one of these runs, and figure 80 shows the spatial speed profile. In this run, the driver applied the brakes while the vehicle traveled over a range from 578.9 ft to 717.3 ft from the test section starting location. Over this interval, 4.2 seconds elapsed and the host vehicle decelerated from 31 mi/hr to 14 mi/hr. This corresponds to an average deceleration of 0.18 g. Table 11 describes each of the seven braking runs and the near stop by average deceleration, initial speed, final speed, and the location where the brakes were released. The table also provides a designation used to identify each run in tabulated results throughout the rest of this chapter.
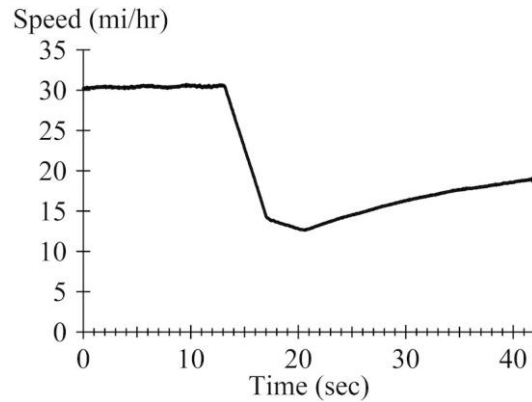
Figure 79. Graph. Braking run temporal speed profiles.
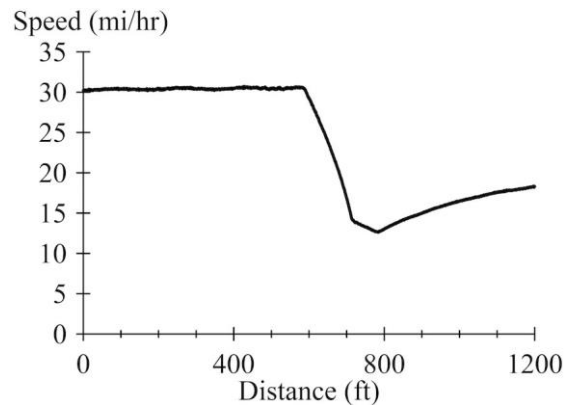
Figure 80. Graph. Braking run spatial speed profiles.

64

Table 11. Braking run characteristics and designations.

Designation	Average Decel. (g)	Speed Range During Braking (mi/hr)	Location, End of Braking (ft)
NS, 45–7 mi/hr, 0.20 g	0.196	44.5–7.1	705.6
Brk, 44–19 mi/hr, 0.19 g	0.195	44.4–18.6	698.8
Brk, 45–18 mi/hr, 0.39 g	0.390	44.6–18.1	660.0
Brk, 31–14 mi/hr, 0.16 g	0.163	30.5–13.7	722.6
Brk, 31–14 mi/hr, 0.18 g	0.178	30.6–14.4	726.5
Brk, 31–14 mi/hr, 0.18 g	0.178	30.6–14.1	717.3
Brk, 31–12 mi/hr, 0.25 g	0.248	30.6–12.2	714.1
Brk, 30–21 mi/hr, 0.84 g	0.842	30.4–21.2	648.8

The test conditions also include three passes at (relatively) constant speed. In one pass, profile data were collected with cruise control set to 45 mi/hr. Since this pass was conducted under favorable test conditions, the roughness values it produced serve as reference values. In another, the host vehicle operated at a speed near 10 mi/hr over the entire test section. This pass is included to confirm that the proposed error suppression algorithms and sensor augmentation do not affect the validity of profile measured at a travel speed of 10 mi/hr or above. In the third pass, the host vehicle traveled over the test section at speeds in a range from 2.5 mi/hr to 3.1 mi/hr. This pass is included to demonstrate the performance at very low speed.

For the stop-and-go, near stop, and braking runs, this chapter quantifies the artificial roughness caused by measurement error using the peak value of the short-interval roughness profile in the range from 600 ft to 750 ft from the test section start. This is the area where the vehicle came to a stop in the stop-and-go runs. (See table 10.) It is also the area where the brakes were released in the runs with braking but no stop. (See table 11.)

Figure 81 shows the short-interval roughness profile from a measurement run performed at a constant speed of 45 mi/hr. In the range near the stop location for stop-and-go runs and the coast for the near stop, the peak value of this short-interval roughness profile is 151.9 inches/mi. This is considered a reference roughness value, since the run was performed under ideal conditions. The average roughness measured at 45 mi/hr over the range from 528 ft to 1056 ft is 100.0 inches/mi. This is the reference value for average IRI over the test section.
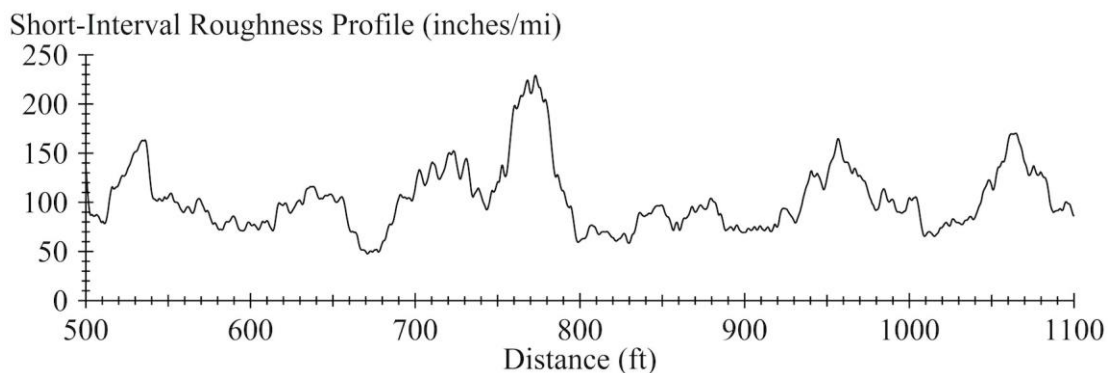
Figure 81. Graph. Short-interval roughness profile measured under favorable conditions.

BASIC TEMPORAL ALGORITHM

The basic temporal algorithm represents a baseline case. The algorithm includes common practices among commercial profilers with temporal data collection architecture, with no added provisions for error suppression. Figure 82 describes the basic temporal profile calculation algorithm. The digitized accelerometer signal, $a_{zp}(t_k)$, is integrated twice. This produces the floating-reference-height signal, which is a time history of vertical position of the profiler reference point, $r_{zp}(t_k)$. The height-sensor signal, $h(t_k)$, provides the relative height of the profiler reference point above the road. Subtraction of it from the vertical position of the profiler reference point produces the time history of relative road elevation beneath the profiler. This is the temporal profile, $r_{zr}(t_k)$. Note that the second character of the subscript on position and motion variables indicates whether a quantity represents the profiler reference point (p) or the road surface (r). The index, k, on time (t) indicates progression at a constant time interval, Δt.
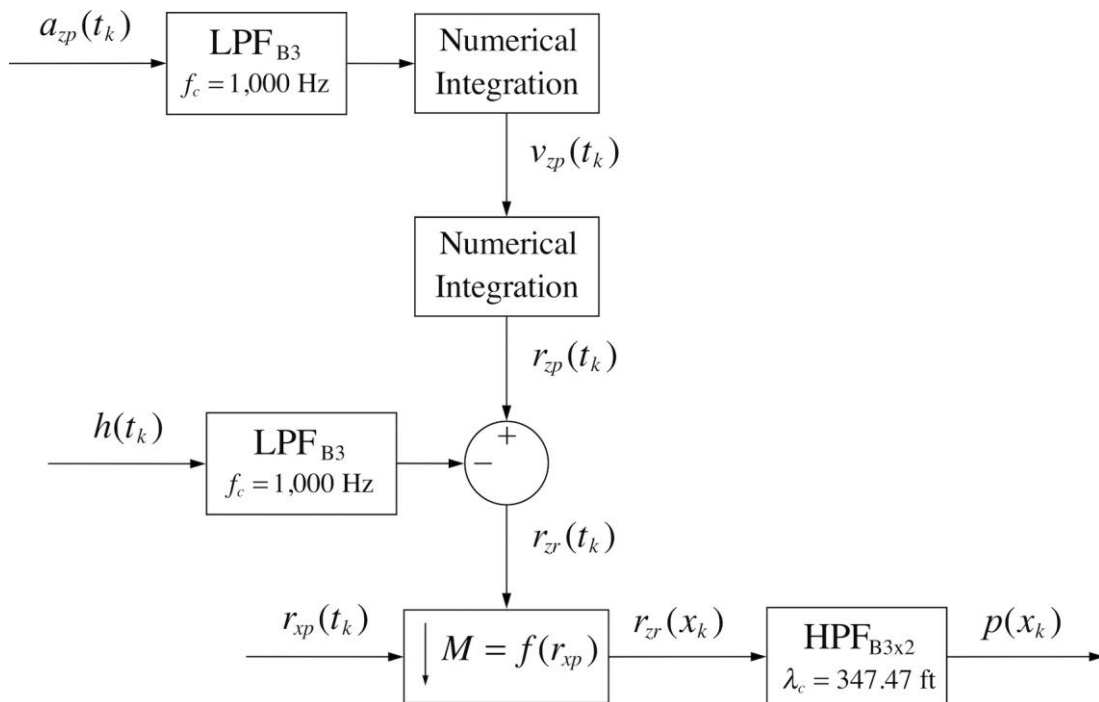
Figure 82. Block Diagram. Basic temporal profile calculation algorithm.

All of the profile computation algorithms discussed in this chapter use the following procedures for anti-aliasing, numerical integration, and conversion from the time domain to the distance domain:

- The accelerometer and height-sensor signals are low-pass filtered to avoid aliasing. The filter is a third-order Butterworth type with a cut-off frequency of 1,000 Hz. (See LPF$_{B3}$ in Appendix A.) At this cut-off frequency, the gain of the filter is very close to unity (>0.9999) in the wavelength range of interest for the IRI and general roughness measurement at practical levels of host-vehicle travel

- Digital integration is performed using the trapezoidal rule.

- The temporal profile, $r_{zr}(t_k)$, is decimated to obtain spatial profile, $r_{zr}(x_k)$, as a function of distance at a constant interval Δx. Temporal data were digitized at a sampling rate of 16,000 Hz, and the profile was decimated to a constant distance interval of 0.2 inches. The decimation factor, M, varies with host-vehicle speed, v_{xp}. In this implementation, the decimation factor depends directly on the progression of pulses from the distance encoder at the left rear wheel. The block diagram represents this signal as host-vehicle longitudinal travel distance, $r_{xp}(t_k)$.

In the basic temporal algorithm, a high-pass filter removes very long wavelength content from the spatial profile. This is done to eliminate content outside of the waveband of interest, which is often contaminated by low signal strength in the accelerometer or slowly fluctuating accelerometer alignment. High-pass filtering of the spatial profile was performed using a set of Butterworth filters. Butterworth filters are IIR type. As such, they impose a non-linear phase shift on the profile. To avoid this, equivalent third-order filters were applied in the forward and reverse directions to cancel the phase shift. (See HPF$_{B3x2}$ in Appendix A.)

The cut-off wavelength setting, λ_c, for the filter (in each direction) was set to 347.47 ft. This results in a reduction of 3 dB at a wavelength of 300 ft for the forward and backward passes combined. The gain of this filter is 0.996 at the upper limit of the wavelength range of interest for the IRI (140.7 ft) and 0.947 at the upper limit of the wavelength range of interest for general roughness measurement (215.2 ft).

The basic temporal algorithm contains no provisions for avoiding drift in the integrated accelerometer signal. As such, a very small bias in the accelerometer signal during the stop translates to a large error in the computed vertical position of the profiler reference point. For example, figure 83 shows a portion of the accelerometer signal for a run with a 10.7-second-long stop. The trace shows a reduction in the severity of acceleration as the speed diminishes. The profiler oscillates vertically at about 2 Hz for a short time after coming to a stop because of pitch motion of the host-vehicle sprung mass. The accelerometer also detects motion at about 13.7 Hz (~820 rpm) caused by engine vibration.
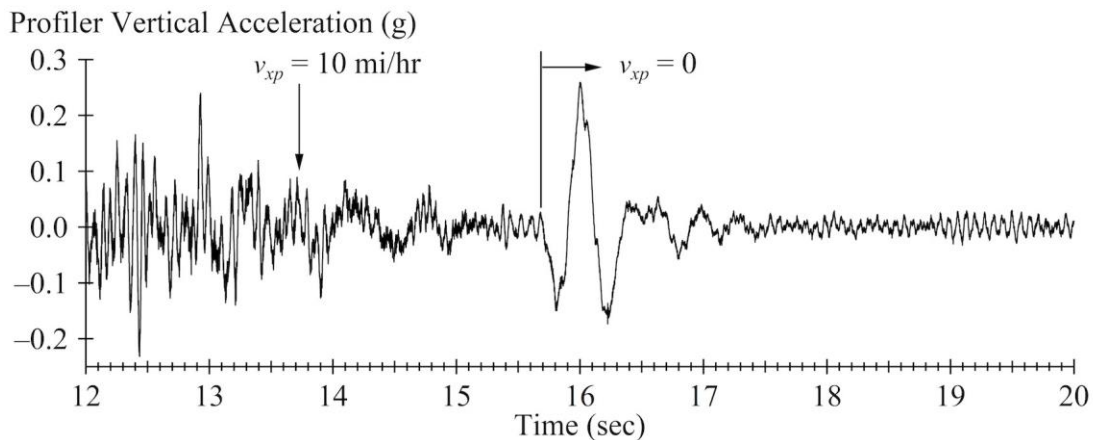
Figure 83. Graph. Accelerometer signal, 10.7-second-long stop.

A small bias exists in the accelerometer signal over the duration of the stop. This is caused by a combination of misalignment of the sensitive axis from true vertical, local variations in the

67

acceleration due to gravity from the assumed nominal value of 32.17405 ft/s^2, fluctuations caused by temperature variations, etc. For this run, the vehicle is stopped for 10.7 seconds, and the average value of the accelerometer signal is 0.00115 g over this interval. This translates to a 2.11 ft increase in elevation after double integration.

The profile also includes the cumulative effect of drift before the stop. Figure 84 shows a portion of the integrated accelerometer signal. At the beginning of the stop, the computed velocity of the profiler reference point is 2.21 ft/s. When it is combined with the bias in acceleration, this initial velocity translates to a change in vertical position of the profiler reference point of 25.79 ft while the vehicle is stopped. Most of this change is artificial, and it is not cancelled by a commensurate change in the height-sensor signal. Since the profiler was not progressing forward over this interval, the elevation change is concentrated at the location of the stop in the spatial profile.
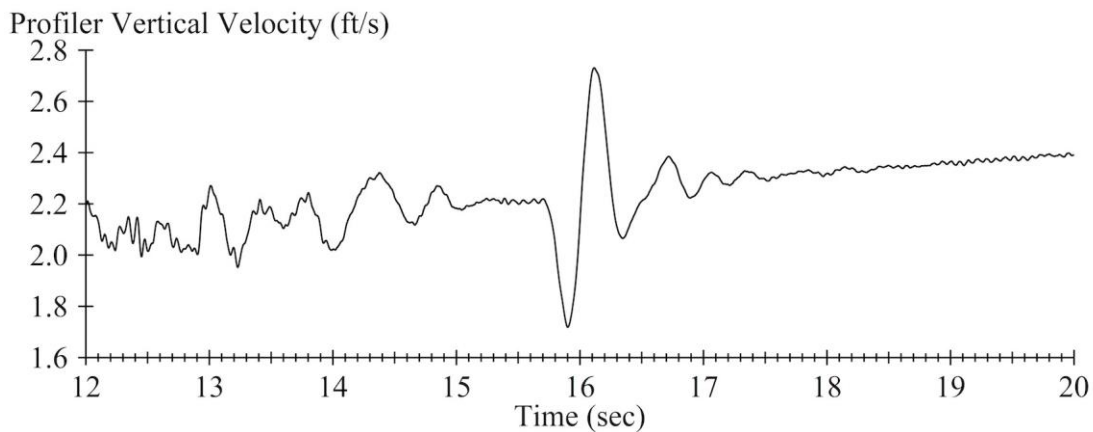
Figure 84. Graph. Integrated accelerometer signal, 10.7-second-long stop.

Figure 85 shows the spatial profile after high-pass filtering. The total magnitude of the change in elevation is greater than 25.79 ft because of the additional effects of drift during very low speed operation near the stop. The concentrated elevation change registers as severe localized roughness in the short-interval roughness profile, as shown in figure 86. The short-interval roughness profile rises to a peak value of 209,076 inches/mi. This implies a contribution to the average IRI value for a 0.1-mile-long segment of 9,899 inches/mi.
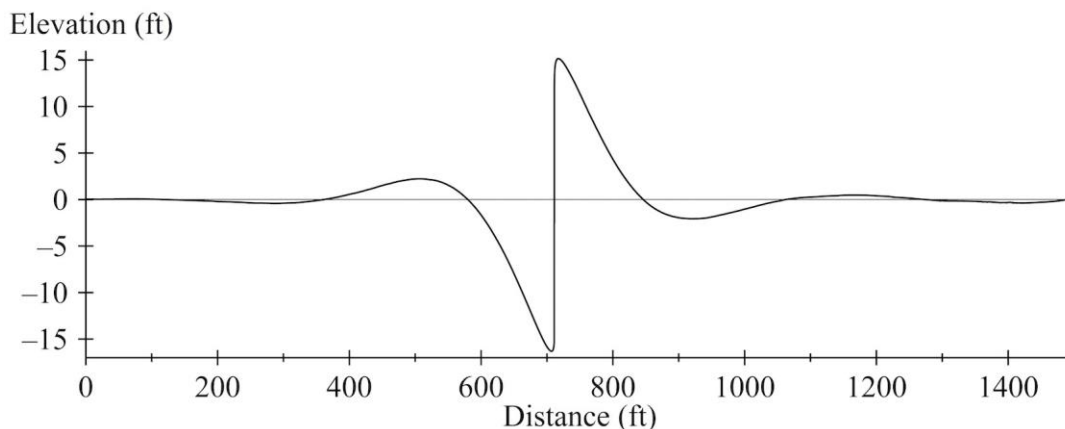
Figure 85. Graph. High-pass filtered profile, 10.7-second-long stop.
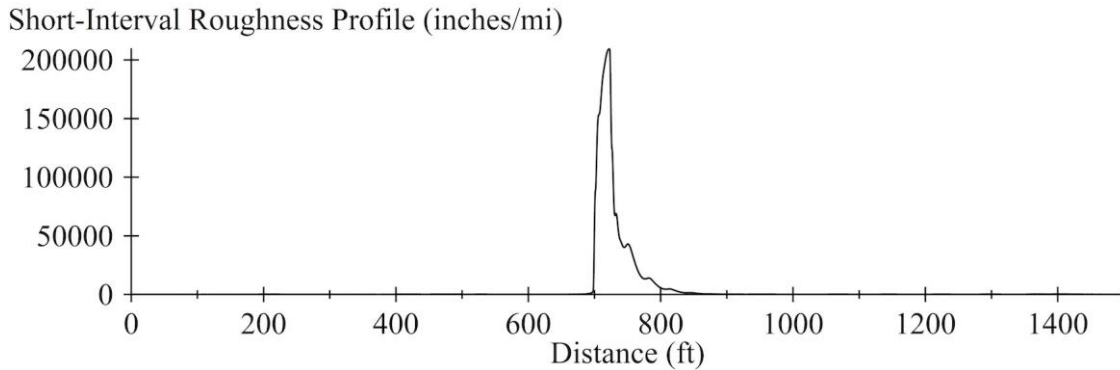
Figure 86. Graph. Short interval roughness profile, 10.7-second-long stop.

Table 12 lists the peak roughness, the percentage error in average roughness, and cross correlation to the reference profile for each test run processed using the basic temporal algorithm. Peak roughness is the highest value in the short-interval roughness profile in the range from 600 ft to 750 ft from the test section start. This is the area where the host vehicle came to a stop in the stop-and-go runs or released the brakes in the braking runs without a stop.

Table 12. Results for the basic temporal algorithm.

Run Designation	Peak Roughness (inches/mi)	Average Roughness Error (Percent)	Cross Correlation
S&G, 1.1-sec stop, 0.17 g	26,195	1,736.8	< 0.2
S&G, 1.1-sec stop, 0.20 g	54,170	3,588.0	< 0.2
S&G, 2.1-sec stop, 0.33 g	13,693	862.6	< 0.2
S&G, 5.8-sec stop, 0.17 g	73,282	4,678.9	< 0.2
S&G, 5.7-sec stop, 0.20 g	60,130	3,784.1	< 0.2
S&G, 5.8-sec stop, 0.20 g	66,733	4,222.7	< 0.2
S&G, 10.7-sec stop, 0.20 g	209,076	13,139.7	< 0.2
NS, 45–7 mi/hr, 0.20 g	1,798	195.3	< 0.2
Brk, 44–19 mi/hr, 0.19 g	214	10.5	0.836
Brk, 45–18 mi/hr, 0.39 g	150	1.7	0.841
Brk, 31–14 mi/hr, 0.16 g	309	17.7	0.650
Brk, 31–14 mi/hr, 0.18 g	301	15.3	0.668
Brk, 31–14 mi/hr, 0.18 g	393	27.9	0.605
Brk, 31–12 mi/hr, 0.25 g	142	0.0	**0.944**
Brk, 30–21 mi/hr, 0.84 g	164	9.3	0.889
10 mi/hr	147	9.2	0.863
3 mi/hr	3,435	1622.7	< 0.2

Reference peak roughness value: 152 inches/mi. Adequate cross correlation > 0.92.

The test runs with a stop or a near stop produced profile with very high peak roughness. This caused a large error in the average roughness for the test section and very low cross correlation. The high peak roughness was caused by a large artificial change in the floating reference height, which was concentrated over a short distance. This is the phenomenon illustrated in figure 83 through figure 86.

The test runs with braking also produced erroneously high peak roughness and a commensurate error in the average roughness. Cross correlation for the majority of braking runs is well below the threshold value of 0.92. Integrator drift caused artificially high roughness throughout the test section for the lower-speed runs. In particular, the integrated signal grew very large in magnitude relative to the terms that are added at each time step. This reduced the effective numerical precision of the calculation. Performing the calculations with higher precision arithmetic would mitigate this error for these test runs. High-precision arithmetic was not incorporated into the algorithm because it would not eliminate this phenomenon during very long production runs.

The basic temporal algorithm performed inadequately for runs with low speed, with braking, and with stops. The performance of the basic temporal algorithm serves as a baseline for demonstrating improvement offered by the other temporal algorithms because it includes no explicit procedures for error suppression. The temporal error suppression algorithms described below are designed to improve the performance of the temporal algorithm.

TEMPORAL MEAN REMOVAL

This algorithm removes the mean from $a_{zp}(t_k)$ and $v_{zp}(t_k)$ before integration. This is done to reduce the drift that accumulates at each stage of integration. In turn, this reduces the magnitude of the artificial elevation change at stops. For example, removal of the mean from the accelerometer signal in the run with the 10.7-second-long stop reduced the mean value during the stop to –0.000454 g. Subsequent removal of the mean from the integrated accelerometer signal produced a value of 0.303 ft/s for velocity of the profiler reference point at the beginning of the stop. Together, these conditions produced a calculated change in vertical position of the profiler reference point of 2.37 ft. As a result, mean removal reduced the peak value of the short-interval roughness profile for the 10.7-second-long stop to 20,119 inches/mi. However, this value remains very high, and implies a contribution to the average IRI value for a 0.1-mile-long section of 952.6 inches/mi.

Table 13 provides roughness and cross correlation results for profiles processed using mean removal. Mean removal offered some improvement in cross correlation over the basic temporal algorithm for the braking test runs, and eliminated the issues with numerical integration for the test run at 3 mi/hr. However, test runs with stops register very large errors in peak roughness and very low cross correlation.

Temporal mean removal is an undesirable method for suppressing integrator drift, because it requires storage of the accelerometer, height-sensor, and encoder signals in the time domain until the end of the profile measurement run. (For algorithms that do not convert signals to spatial coordinates in real time, the encoder signal is most likely replaced by distance or speed as a function of time.) Further, removal of the global mean from each signal does not guarantee a reduction in accelerometer bias during each stop, so drift in the floating-reference-height signal is still possible. This is particularly true in profile measurements for pavement network monitoring. In that application the profile measurement runs often go on for more than an hour and cover tens of miles of roadway. In such cases, mechanisms that determine the level of accelerometer bias often change between stops, such as temperature, road grade, and cross slope.

Table 13. Results for temporal mean removal.

Run Designation	Peak Roughness (inches/mi)	Average Roughness Error (Percent)	Cross Correlation
S&G, 1.1-sec stop, 0.17 g	6,560	417.2	< 0.2
S&G, 1.1-sec stop, 0.20 g	6,261	398.5	< 0.2
S&G, 2.1-sec stop, 0.33 g	3,687	220.9	< 0.2
S&G, 5.8-sec stop, 0.17 g	15,950	998.2	< 0.2
S&G, 5.7-sec stop, 0.20 g	14,156	871.2	< 0.2
S&G, 5.8-sec stop, 0.20 g	14,740	920.1	< 0.2
S&G, 10.7-sec stop, 0.20 g	20,119	1258.2	< 0.2
NS, 45–7 mi/hr, 0.20 g	566	47.5	0.332
Brk, 44–19 mi/hr, 0.19 g	156	2.4	**0.954**
Brk, 45–18 mi/hr, 0.39 g	142	0.5	0.848
Brk, 31–14 mi/hr, 0.16 g	149	–0.9	**0.930**
Brk, 31–14 mi/hr, 0.18 g	150	–0.8	**0.941**
Brk, 31–14 mi/hr, 0.18 g	181	1.1	**0.953**
Brk, 31–12 mi/hr, 0.25 g	137	–0.1	**0.942**
Brk, 30–21 mi/hr, 0.84 g	161	9.4	0.891
10 mi/hr	146	–0.7	**0.985**
3 mi/hr	150	–4.5	0.903

Reference peak roughness value: 152 inches/mi. Adequate cross correlation (> 0.92) is shown in bold.

An alternative form of mean removal was considered that set the accelerometer signal to zero during stops. This was not viable for two reasons. First, this introduces a concentrated change in curvature into the profile at the beginning and end of the stop. Second, the content that captures true vertical vibration of the profiler reference point during the stop is needed to cancel the equal and opposite fluctuations in distance to the road surface measured by the height sensor.

TEMPORAL HIGH-PASS FILTERING, PRE-INTEGRATION

This proposed algorithm applies high-pass filtering to the accelerometer signal before integration to suppress drift in the floating reference height. In particular, by reducing the mean value of each signal before integration, the concentrated elevation change that appears in areas with braking and stops is reduced.

Figure 87 shows a block diagram of the time-domain portion of the basic temporal algorithm with temporal high-pass filtering added. Accelerometer and height-sensor signals are high-pass filtered in the time domain. Once the temporal profile is computed, the cascaded version of the third-order Butterworth high-pass filter is applied in reverse order and in the reverse direction (HPF_{B3S2R}, HPF_{B3S1R}). The reverse passes cancel the phase shift imposed by the forward passes. Appendix A describes each filter stage in detail. To support the reverse filtering stage, the temporal high-pass filtering algorithm requires storage of the pre-filtered temporal profile, $r_{zr}(t_k)$, and the encoder signal, $r_{xp}(t_k)$, in the time domain until the end of the profile measurement run.
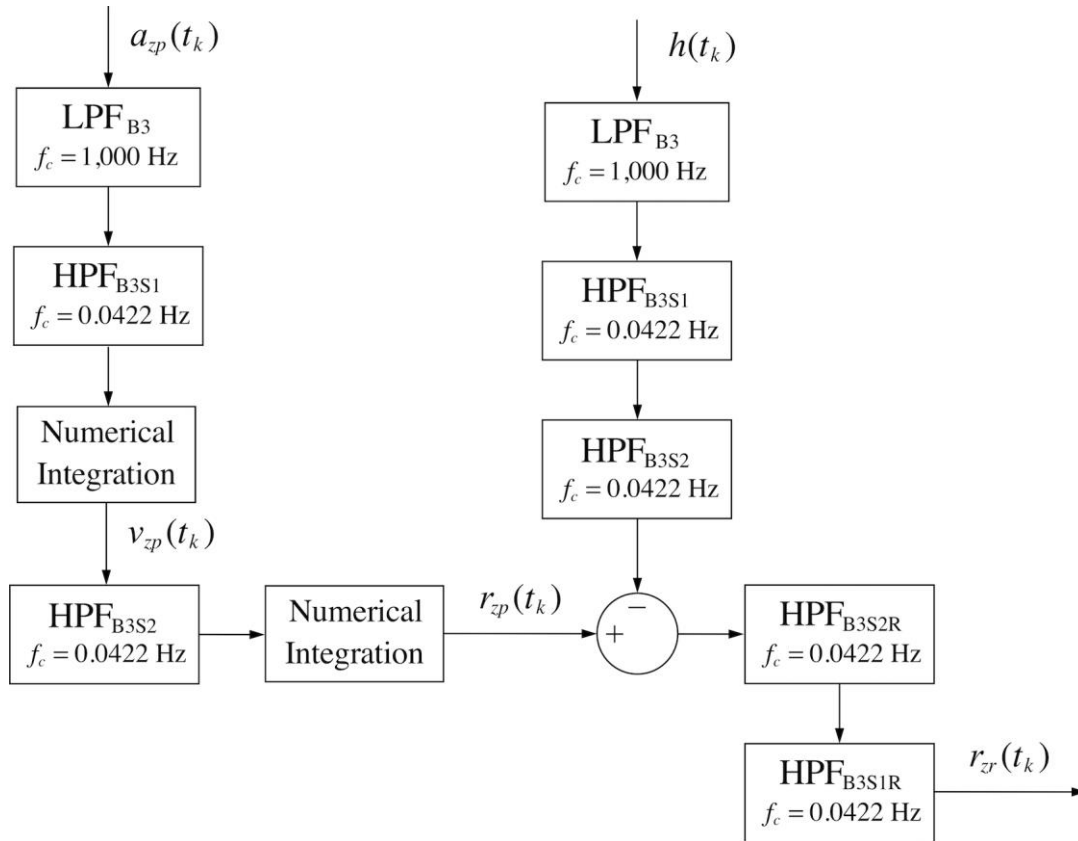
Figure 87. Block diagram. Temporal profile calculation algorithm with high-pass filtering.

The high-pass filtering in the temporal portion of this algorithm is applied in lieu of spatial high-pass filtering. That is, no additional filtering is performed after decimation to spatial profile. The cut-off frequency values for the individual high-pass filtering stages shown in figure 87 were adjusted to place the cut-off frequency of the collective set at 0.0489 Hz. This corresponds to a cut-off wavelength of 300 ft at a host-vehicle speed of 10 mi/hr.

Temporal high-pass filtering suppressed integrator drift more effectively than mean removal. For example, the change in profiler reference point height during the 10.7-second-long stop was reduced to 0.699 ft. This reduced the peak value of the short-interval roughness profile to 1,837 inches/mi.

Table 14 provides roughness and cross correlation results for profiles processed using temporal high-pass filtering. Temporal high-pass filtering consistently lowered the errors in peak roughness values relative to the basic temporal algorithm and relative to mean removal for the stop-and-go runs and the near stop. However, in the runs with a stop, cross correlation values were very low, and the artificial roughness values exceed the typical range for very rough localized road features. With one exception, use of temporal high-pass filtering reduced peak roughness values relative to the basic temporal algorithm.

Table 14. Results for temporal high-pass filtering.

Run Designation	Peak Roughness (inches/mi)	Average Roughness Error (Percent)	Cross Correlation
S&G, 1.1-sec stop, 0.17 g	2,072	117.1	< 0.2
S&G, 1.1-sec stop, 0.20 g	1,976	107.2	< 0.2
S&G, 2.1-sec stop, 0.33 g	781	36.8	0.256
S&G, 5.8-sec stop, 0.17 g	2,699	151.5	< 0.2
S&G, 5.7-sec stop, 0.20 g	1,522	78.7	< 0.2
S&G, 5.8-sec stop, 0.20 g	1,958	106.5	< 0.2
S&G, 10.7-sec stop, 0.20 g	1,837	99.5	< 0.2
NS, 45–7 mi/hr, 0.20 g	316	17.7	0.578
Brk, 44–19 mi/hr, 0.19 g	157	2.3	**0.954**
Brk, 45–18 mi/hr, 0.39 g	141	1.2	0.848
Brk, 31–14 mi/hr, 0.16 g	145	–1.0	**0.929**
Brk, 31–14 mi/hr, 0.18 g	148	–0.8	**0.941**
Brk, 31–14 mi/hr, 0.18 g	170	0.6	**0.963**
Brk, 31–12 mi/hr, 0.25 g	144	0.1	**0.948**
Brk, 30–21 mi/hr, 0.84 g	159	8.6	0.898
10 mi/hr	146	–0.7	**0.985**
3 mi/hr	147	–4.2	**0.940**

Reference peak roughness value: 152 inches/mi. Adequate cross correlation (> 0.92) is shown in bold.

Temporal high-pass filtering increased cross correlation for all braking test runs relative to the basic temporal algorithm (see table 12), and adequate cross correlation is achieved for five of the seven runs as shown in table 14. Cross correlation was improved relative to the basic temporal algorithm (see table 12) for the low-speed runs, and was well within the adequate range as shown in table 14. However, the use of a constant cut-off frequency of 0.0489 Hz caused a reduction in the IRI value for the test run at 3 mi/hr. This is because 0.0489 Hz corresponds to a cut-off wavelength of 90 ft at 3 mi/hr, and some of the wavelength range of interest for the IRI is removed. This demonstrates the trade-off imposed by using temporal high-pass filtering with a constant cut-off frequency: removal of low-frequency content reduces artificial localized roughness during braking and at stops by suppressing integrator drift but removes some of the content of interest at very low speed.

LOCAL SUPPRESSION

The "local suppression" algorithm applies digital control to eliminate bias in the integrated accelerometer signal when the host vehicle is traveling at low speed. This algorithm is applied in conjunction with temporal high-pass filtering. At higher host-vehicle speeds, the algorithm applies temporal high-pass filtering as shown in figure 87. When the travel speed passes below 10 mi/hr, the portion of the algorithm where the accelerometer signal is integrated switches to the procedure shown in figure 88.
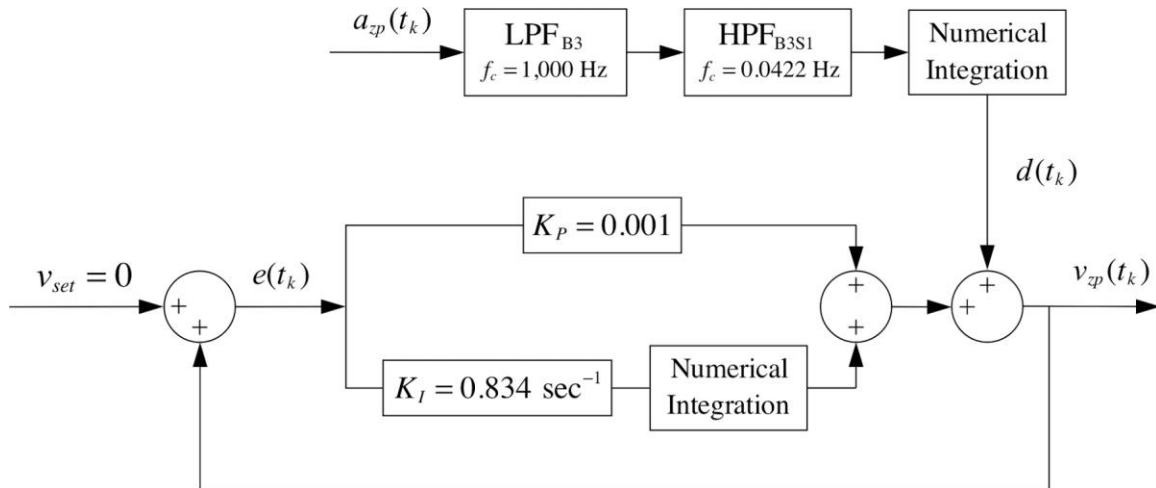
Figure 88. Block diagram. Local suppression algorithm applied at low speed.

The concept of the local suppression algorithm is to artificially suppress the absolute value of the integrated accelerometer signal, $v_{zp}(t_k)$, when the travel speed is low. In turn, this suppresses the computed change in height of the profiler reference point after the next stage of integration. A controller is used in place of directly setting the integrated accelerometer signal to zero in regions with low travel speed because preliminary analysis showed that doing so introduced a sudden change in slope into the computed profile. As an alternative, the suppression algorithm proposed here attempts to mitigate the slope break by introducing a gradual reduction in the magnitude of $v_{zp}(t_k)$ in regions of low travel speed. This is done using a simple PI controller with a slow time constant. The controller is designed to retain content at frequencies above 2 Hz with minimal phase shift. The procedure retains high-frequency content because it is needed to cancel relative motion between the profiler reference point and the road surface detected by the height sensor.

In the procedure illustrated in figure 88, a discrete-time PI controller operates on vertical velocity (i.e., integrated vertical acceleration) with a set point of zero. The integrated accelerometer signal serves as a disturbance, $d(t_k)$. The controller rejects the initial offset at the instant of the switch and low-frequency content from the disturbance.

Figure 89 provides the expression for the controller time constant (τ) for a step response, and figure 90 provides the frequency response function for the output relative to the disturbance.

$$\tau = \frac{K_P + 1}{K_I}$$

Figure 89. Equation. Controller time constant.

$$\frac{v_{zp}(\omega)}{d(\omega)} = \frac{1}{K_I}\left[\frac{j\omega - \tau\omega^2}{1 + \tau^2\omega^2}\right]$$

Figure 90. Equation. Frequency response relative to the disturbance.

In figure 90, ω is angular frequency. The controller settings ($K_P = 0.001$, $K_I = 0.834$ sec^{-1}) produce a time constant of 1.2 seconds. At 2 Hz, this frequency response function has a gain of 0.996 and a phase shift of 1.9 degrees. At 14 Hz, the gain is 0.999 and the phase shift is 0.3 degrees. For very high frequency content, the gain approaches 0.999 and the phase shift diminishes to zero.

The criterion for activating local suppression depends on host-vehicle speed. Direct numerical differentiation of the wheel encoder signal at a sampling rate of 16,000 Hz produces a very noisy estimate of speed. As such, the decision to switch at any instant is based on the accumulated progression of encoder pulses over the preceding 0.05 seconds.

Table 15 provides roughness and cross correlation results for test runs with stops, with a near stop, and at low speed using local suppression together with temporal high-pass filtering. In every case, the error in peak roughness was reduced by a factor of at least 10 relative to the basic temporal algorithm. With one exception, adding local suppression reduced the error in peak roughness values relative to temporal high-pass filtering alone for the runs with a stop. In many cases, the peak roughness values were reduced to less than half. However, the peak roughness values for the runs with stops remain several times larger than the reference value in many of the test runs. As a result, large errors remain in the average roughness values and cross correlation is well below 0.92 in all of the runs. Note that local suppression was not activated in the other runs with braking, so those results are unchanged relative to temporal high-pass filtering.

Table 15. Results for local suppression combined with temporal high-pass filtering.

Run Designation	Peak Roughness (inches/mi)	Average Roughness Error (Percent)	Cross Correlation
S&G, 1.1-sec stop, 0.17 g	510	20.9	0.374
S&G, 1.1-sec stop, 0.20 g	888	42.3	0.219
S&G, 2.1-sec stop, 0.33 g	967	46.0	< 0.2
S&G, 5.8-sec stop, 0.17 g	428	18.3	0.443
S&G, 5.7-sec stop, 0.20 g	486	14.9	0.379
S&G, 5.8-sec stop, 0.20 g	359	12.1	0.530
S&G, 10.7-sec stop, 0.20 g	446	16.4	0.460
NS, 45–7 mi/hr, 0.20 g	214	10.5	0.702
10 mi/hr	146	–0.7	**0.985**
3 mi/hr	127	–14.4	0.588

Reference peak roughness value: 152 inches/mi. Adequate cross correlation (> 0.92) is shown in bold.

At 10 mi/hr, the switch to local suppression was not activated. As such, the profile and the resulting roughness were the same as in the temporal high-pass filtering algorithm. In the run at 3 mi/hr, removal of content from the integrated accelerometer signal caused a reduction in the measured roughness. The cut-off frequency for disturbance response in the local suppression procedure is 0.13 Hz. At frequencies near this value and below, the floating-reference-height signal derived from the accelerometer contributes much more heavily to the profile than the height-sensor signal. Attenuating it removed some of the measured roughness.

Local suppression offers an improvement over temporal high-pass filtering alone and a major improvement over the basic temporal algorithm. However, profile content measured at low speed is lost, and the overall performance in not adequate.

ADAPTIVE HIGH-PASS FILTERING

The performance of the temporal high-pass filtering algorithm with a fixed cut-off frequency is limited because the effective cut-off wavelength increases in proportion to speed. The cut-off frequency was set to 0.0489 Hz to enforce a cut-off wavelength of 300 ft at a host-vehicle speed of 10 mi/hr. At higher travel speeds where the effective cut-off wavelength is greater than 300 ft, additional drift in the integrated accelerometer signal accumulates that is not needed to retain content of interest. This mechanism is illustrated conceptually in figure 83 and figure 84.

A modified high-pass filter is proposed with a cut-off frequency that adapts to host-vehicle speed to address this shortcoming of the temporal high-pass filtering algorithm. To do this, the adaptive high-pass filtering algorithm imposes an upper limit on the cut-off wavelength at progressively higher travel speeds and an upper limit on cut-off frequency at progressively lower travel speeds.

The adaptive high-pass filtering algorithm includes the same components as the temporal high-pass filtering algorithm, with the exception that the high-pass filter cut-off frequency (f_c) is adjusted at each time step as shown in figure 91.

$$f_c(t_k) = \frac{f_{ls} + \left(v_{xp}(t_k)/\lambda_c\right)e^{\alpha(v_{xp}(t_k)-v_0)}}{1 + e^{\alpha(v_{xp}(t_k)-v_0)}}$$

Figure 91. Equation. High-pass filter cut-off frequency.

In figure 91, $v_{xp}(t_k)$ is the current value of host-vehicle speed in ft/s, f_{ls} is the desired cut-off frequency for low-speed operation in Hz, and λ_c is the desired cut-off wavelength for high-speed operation in ft. Parameters v_0 and α determine the speed range where the cut-off transitions from the high-speed wavelength setting to the low-speed frequency setting and the steepness of the transition. Like the local suppression algorithm, real-time estimates of speed are averaged over 0.05 seconds.

In this implementation, f_{ls} is 0.45 Hz, λ_c is 347.47 ft, v_0 is 9.11 ft/s, and α is 0.762 (for speed expressed in ft/s). Figure 92 shows the cut-off frequency as a function of speed using these settings, and figure 93 shows the effective cut-off wavelength as a function of speed. The plots produced by this function include three features that affect the performance of the algorithm.
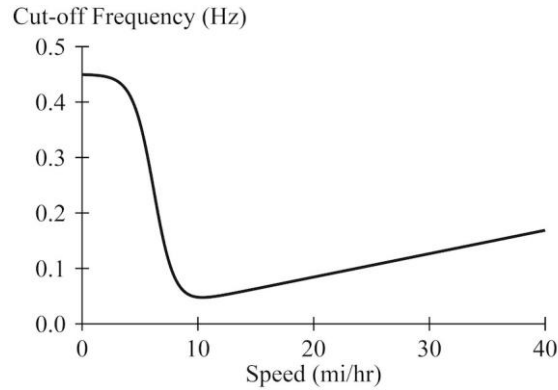
Figure 92. Graphs. Adaptive high-pass filter cut-off frequency.
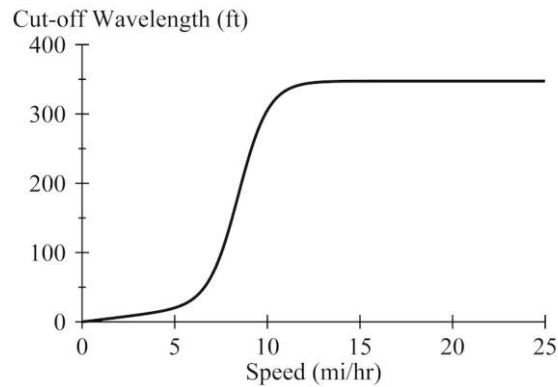
Figure 93. Graphs. Adaptive high-pass filter cut-off wavelength.

First, the function limits the cut-off wavelength explicitly at high speed. This avoids rapid changes in the cut-off wavelength as host-vehicle speed changes during braking, which would introduce artificial curvature into the floating-reference-height signal. Similarly, the gradual transition between the high-speed and low-speed limits for speeds below 10 mi/hr helps mitigate this problem.

Second, the function maintains the wavelength range of interest for host-vehicle speeds of 10 mi/hr and above. At 10 mi/hr, the cut-off frequency is 0.0481 Hz, which is an effective cut-off wavelength of 305.24 ft. For the combined filtering applied by this algorithm, this is a gain of 0.991 at the upper limit of the wavelength range of interest for the IRI (140.7 ft) and 0.891 at the upper limit of the wavelength range of interest for general roughness measurement (215.2 ft).

Third, the function limits temporal frequency rather than spatial frequency at low speeds to avoid an infinite cut-off wavelength as speed approaches zero. This helps reduce drift in the double-integrated accelerometer signal. However, the filtering removes a progressively larger portion of the wavelength range of interest as speed diminishes.

This algorithm requires storage of the computed profile and the encoder signal (or an equivalent) until the end of the measurement run. To avoid this, a version of the algorithm is proposed in which the backward filtering pass is performed after decimation to spatial profile. As such, the

77

algorithm performs all temporal calculations in real-time. Figure 94 presents the details of the adaptive high-pass filtering algorithm with the spatial backward pass.
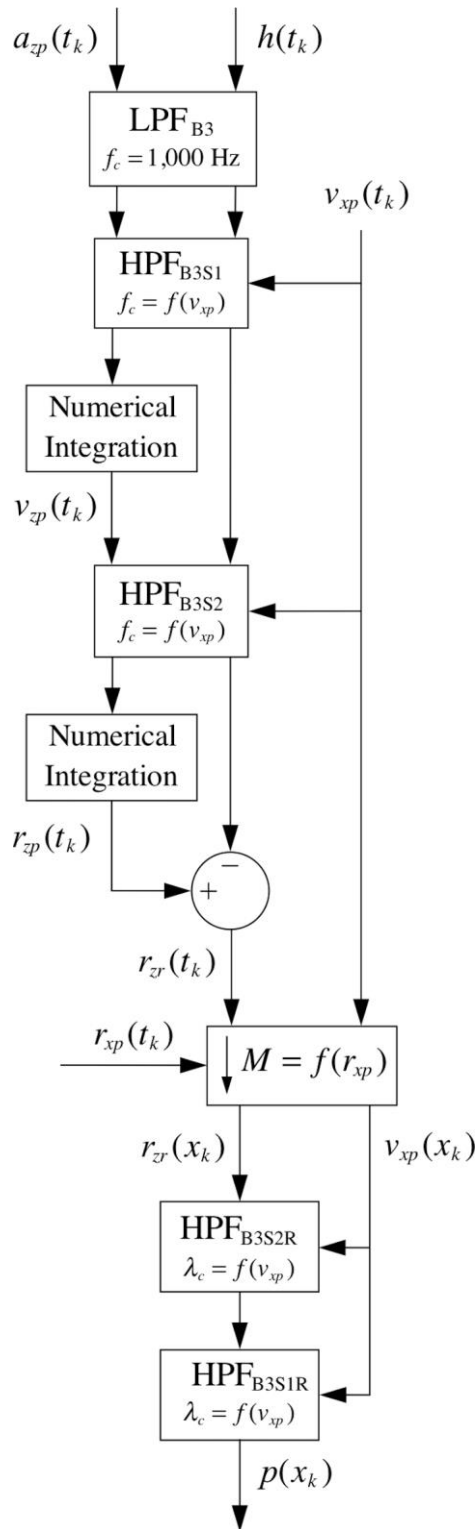
Figure 94. Block diagram. Adaptive high-pass filtering algorithm, spatial backward pass.

In this implementation the speed signal, $v_{xp}(t_k)$, is derived in real-time in the temporal portion of the algorithm using the progression of encoder pulses over the preceding 0.05 seconds. Like the temporal profile, the temporal speed record is decimated and converted to the distance domain. To accommodate the backward filtering pass, the spatial record of speed must be stored until the end of the measurement run.

Table 16 and table 17 list the peak roughness, the percentage error in average roughness, and cross correlation to the reference profile for each test run processed using the two adaptive filtering algorithms. Both adaptive algorithms demonstrated a major improvement over the basic temporal algorithm. (See table 12.) Relative to their non-adaptive counterpart (i.e., the temporal high-pass filtering algorithm), both adaptive high-pass filtering algorithms reduced the errors in peak roughness level in all of the runs with a stop and the near stop. In all of the runs with a stop, the artificial localized roughness was less severe using the real-time adaptive high-pass filtering algorithm than the temporal high-pass filtering algorithm, both with and without with local suppression. (See table 15 and table 14, respectively.) Neither of the adaptive algorithms offered consistently better results than the other for the test runs with braking and stops.

Both algorithms removed valid content in the wavelength range of interest from the profile measured at 3 mi/hr, and reduced the measured roughness by half. This is reflected in the low cross correlation levels.

Table 16. Results for adaptive high-pass filtering.

Run Designation	Peak Roughness (inches/mi)	Average Roughness Error (Percent)	Cross Correlation
S&G, 1.1-sec stop, 0.17 g	334	10.3	0.742
S&G, 1.1-sec stop, 0.20 g	237	3.1	0.831
S&G, 2.1-sec stop, 0.33 g	447	18.9	0.565
S&G, 5.8-sec stop, 0.17 g	753	38.7	0.302
S&G, 5.7-sec stop, 0.20 g	282	5.8	0.764
S&G, 5.8-sec stop, 0.20 g	296	10.1	0.716
S&G, 10.7-sec stop, 0.20 g	290	9.0	0.727
NS, 45–7 mi/hr, 0.20 g	150	1.3	0.852
Brk, 44–19 mi/hr, 0.19 g	159	2.6	**0.951**
Brk, 45–18 mi/hr, 0.39 g	140	1.7	0.844
Brk, 31–14 mi/hr, 0.16 g	148	–0.8	**0.931**
Brk, 31–14 mi/hr, 0.18 g	151	–0.7	**0.943**
Brk, 31–14 mi/hr, 0.18 g	173	0.8	**0.958**
Brk, 31–12 mi/hr, 0.25 g	147	0.3	**0.950**
Brk, 30–21 mi/hr, 0.84 g	167	8.5	0.859
10 mi/hr	146	–0.8	**0.985**
3 mi/hr	75	–52.0	0.321

Reference peak roughness value: 152 inches/mi. Adequate cross correlation (> 0.92) is shown in bold.

Table 17. Results for adaptive high-pass filtering with a backward pass.

Run Designation	Peak Roughness (inches/mi)	Average Roughness Error (Percent)	Cross Correlation
S&G, 1.1-sec stop, 0.17 g	180	1.6	0.880
S&G, 1.1-sec stop, 0.20 g	263	4.7	0.815
S&G, 2.1-sec stop, 0.33 g	366	17.5	0.581
S&G, 5.8-sec stop, 0.17 g	416	20.1	0.576
S&G, 5.7-sec stop, 0.20 g	179	0.3	0.854
S&G, 5.8-sec stop, 0.20 g	343	12.1	0.655
S&G, 10.7-sec stop, 0.20 g	291	9.3	0.724
NS, 45–7 mi/hr, 0.20 g	250	4.9	0.793
Brk, 44–19 mi/hr, 0.19 g	159	2.7	**0.950**
Brk, 45–18 mi/hr, 0.39 g	141	1.6	0.846
Brk, 31–14 mi/hr, 0.16 g	149	–0.8	**0.932**
Brk, 31–14 mi/hr, 0.18 g	152	–0.7	**0.943**
Brk, 31–14 mi/hr, 0.18 g	176	1.0	**0.955**
Brk, 31–12 mi/hr, 0.25 g	159	1.1	**0.952**
Brk, 30–21 mi/hr, 0.84 g	205	10.5	0.841
10 mi/hr	146	–0.8	**0.985**
3 mi/hr	75	–51.9	0.322

Reference peak roughness value: 152 inches/mi. Adequate cross correlation (> 0.92) is shown in bold.

The adaptive high-pass filtering algorithms offered the greatest reduction in artificial localized roughness for runs with braking and stops. However, a high percentage error in peak roughness remains for most of the runs with stops, and cross correlation levels are below the threshold value of 0.92 for all of the runs with stops, two of the runs with braking, and the run at 3 mi/hr. The adaptive high-pass filtering algorithm with the spatial backward pass is recommended for use on profilers with temporal architecture, but only as a means of avoiding large error in roughness measurement when it is not practical to use additional sensors.

BASIC SPATIAL ALGORITHM

The basic spatial algorithm represents a baseline case. The algorithm includes common practices among commercial profilers with spatial data collection architecture, with no added provisions for error suppression. Figure 95 describes the basic spatial profile calculation algorithm.

This algorithm includes the same processing steps as the basic temporal algorithm with one exception. The algorithm converts the accelerometer and height-sensor signals to spatial coordinates before combining them to calculate the profile. As a result, numerical integration of the accelerometer signal is performed in the distance domain. A high-pass filter removes very long wavelength content from the spatial profile. As described in Appendix A (see HPF_{B3x2}), equivalent third-order IIR filters are applied in the forward and reverse directions to cancel the phase shift.
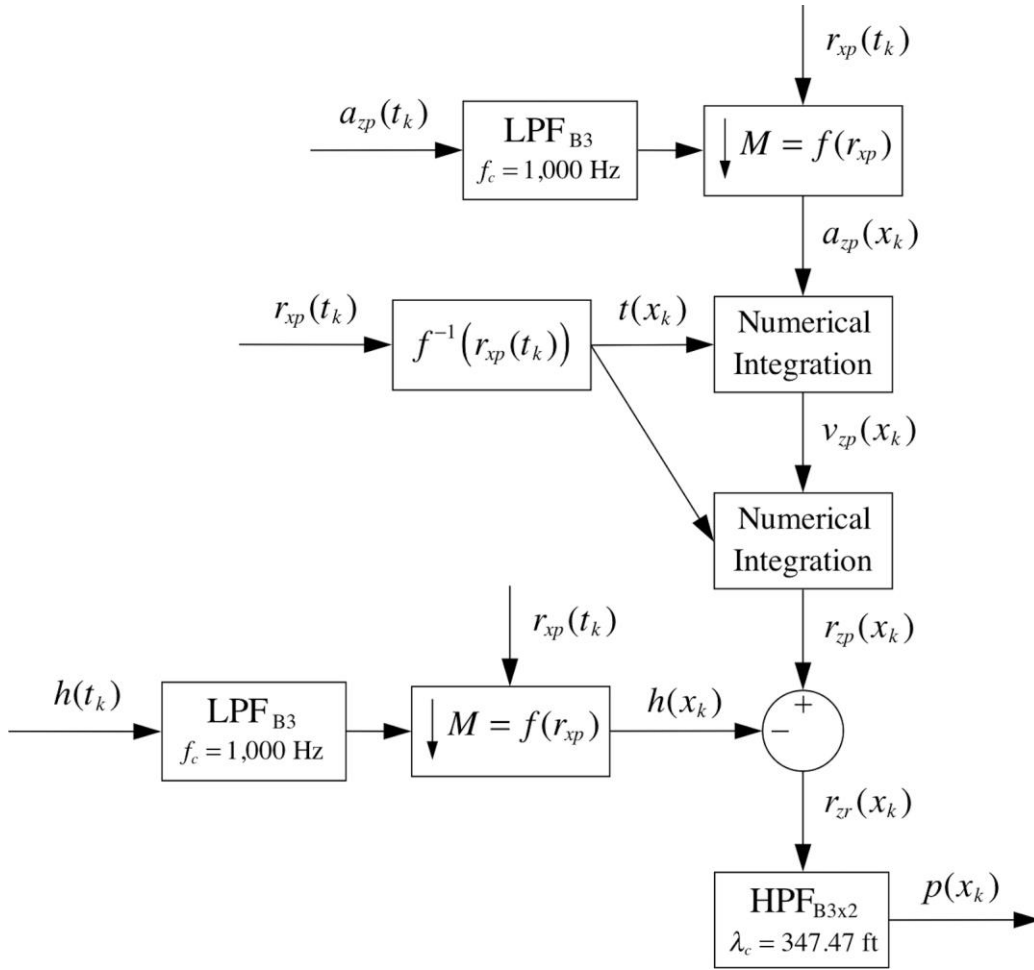
Figure 95. Block diagram. Basic spatial profile calculation algorithm.

The basic spatial calculation algorithm shown in figure 95 typically operates in real time. Real-time operation was simulated using the stored time-domain signals. The simulated algorithm "captures" accelerometer and height-sensor readings from the time-domain signals each time it is triggered by a distance encoder pulse. To accommodate changes in host-vehicle speed, the algorithm must calculate a time step for integration corresponding to each distance increment. To support integration in the distance domain, the simulated algorithm stores the time associated with each distance sample. In turn, the numerical integration algorithm computes the elapsed time between spatial samples (Δt), as shown if figure 96. Numerical integration proceeds using the elapsed time associated with each distance increment, as shown in figure 97 and figure 98.

$$\Delta t(x_k) = t(x_k) - t(x_{k-1})$$

Figure 96. Equation. Elapsed time between distance samples.

$$v_{zp}(x_k) = v_{zp}(x_{k-1}) + \Delta t(x_k)\big(a_{zp}(x_k) + a_{zp}(x_{k-1})\big)$$

Figure 97. Equation. First state of numerical integration.

81

$$r_{zp}(x_k) = r_{zp}(x_{k-1}) + \Delta t(x_k)\big(v_{zp}(x_k) + v_{zp}(x_{k-1})\big)$$

Figure 98. Equation. Second stage of numerical integration.

Like the basic temporal algorithm, this algorithm often produces a large artificial change in elevation at the location where the host vehicle stops. For example, in the run with the 10.7-second-long stop, the time difference between the readings surrounding the stop was 10.7643 seconds. The accelerometer reading at the sample preceding the stop was –0.01865 g and the trailing reading was 0.00910 g. This resulted in a change of the integrated accelerometer signal to –1.66484 ft/s from a leading value of –0.01045 ft/s. After the second stage of integration, these readings translated to a computed change in vertical position of the profiler reference point of 9.017 ft downward. This is not balanced by the height-sensor reading, which indicated an upward change of 0.6 inches. The peak value of the short-interval roughness profile at the stop for this run was 135,657 inches/mi.

Table 18 lists the peak roughness, the percentage error in average roughness, and cross correlation to the reference profile for each test run processed using the basic spatial algorithm. All test runs with a stop or a near stop produce profiles with very high errors in peak localized roughness. This caused a large error in the average roughness for the test section and very low cross correlation.

Table 18. Results for the basic spatial algorithm.

Run Designation	Peak Roughness (inches/mi)	Average Roughness Error (Percent)	Cross Correlation
S&G, 1.1-sec stop, 0.17 g	28,028	1859.7	< 0.2
S&G, 1.1-sec stop, 0.20 g	50,679	3374.5	< 0.2
S&G, 2.1-sec stop, 0.33 g	13,534	852.5	< 0.2
S&G, 5.8-sec stop, 0.17 g	56,955	3668.3	< 0.2
S&G, 5.7-sec stop, 0.20 g	28,342	1807.1	< 0.2
S&G, 5.8-sec stop, 0.20 g	55,755	3544.9	< 0.2
S&G, 10.7-sec stop, 0.20 g	135,657	8607.7	< 0.2
NS, 45–7 mi/hr, 0.20 g	1,761	190.8	< 0.2
Brk, 44–19 mi/hr, 0.19 g	216	10.8	0.848
Brk, 45–18 mi/hr, 0.39 g	151	1.9	0.838
Brk, 31–14 mi/hr, 0.16 g	301	15.8	0.671
Brk, 31–14 mi/hr, 0.18 g	301	16.7	0.684
Brk, 31–14 mi/hr, 0.18 g	390	27.2	0.621
Brk, 31–12 mi/hr, 0.25 g	141	0.1	**0.942**
Brk, 30–21 mi/hr, 0.84 g	181	10.3	0.879
10 mi/hr	150	0.2	**0.985**
3 mi/hr	1459	928.5	< 0.2

Reference peak roughness value: 152 inches/mi. Adequate cross correlation (> 0.92) is shown in bold.

Cross correlation for the majority of braking test runs is well below the threshold value of 0.92. In the test run at 3 mi/hr, excessive drift in the floating-reference-height signal caused issues with numerical precision during integration. Overall, the basic temporal calculation algorithm demonstrated inadequate performance at stops, during braking, and at 3 mi/hr.

The performance of the basic spatial algorithm serves as a baseline for demonstrating improvement offered by the other spatial algorithms because it includes no explicit procedures for error suppression. The spatial error suppression algorithms described below are designed to improve the performance of the spatial algorithm.

SPATIAL HIGH-PASS FILTERING, PRE-INTEGRATION

This proposed algorithm is a variation on the basic spatial algorithm in which high-pass filtering is applied to the accelerometer signal before each stage of integration. Application of high-pass filtering to the accelerometer signal before each stage of integration suppresses drift in the integrated accelerometer signal. This algorithm applies forward-running filtering stages to the height sensor and accelerometer signals after conversion to spatial coordinates, but before combining them into profile. The backward-running filtering stages are applied to the profile. (Appendix A describes each filtering stage.) The backward-running filters are applied to cancel the phase shift imposed by the filters that are applied to the sensor signals. Figure 99 provides the details of this algorithm.
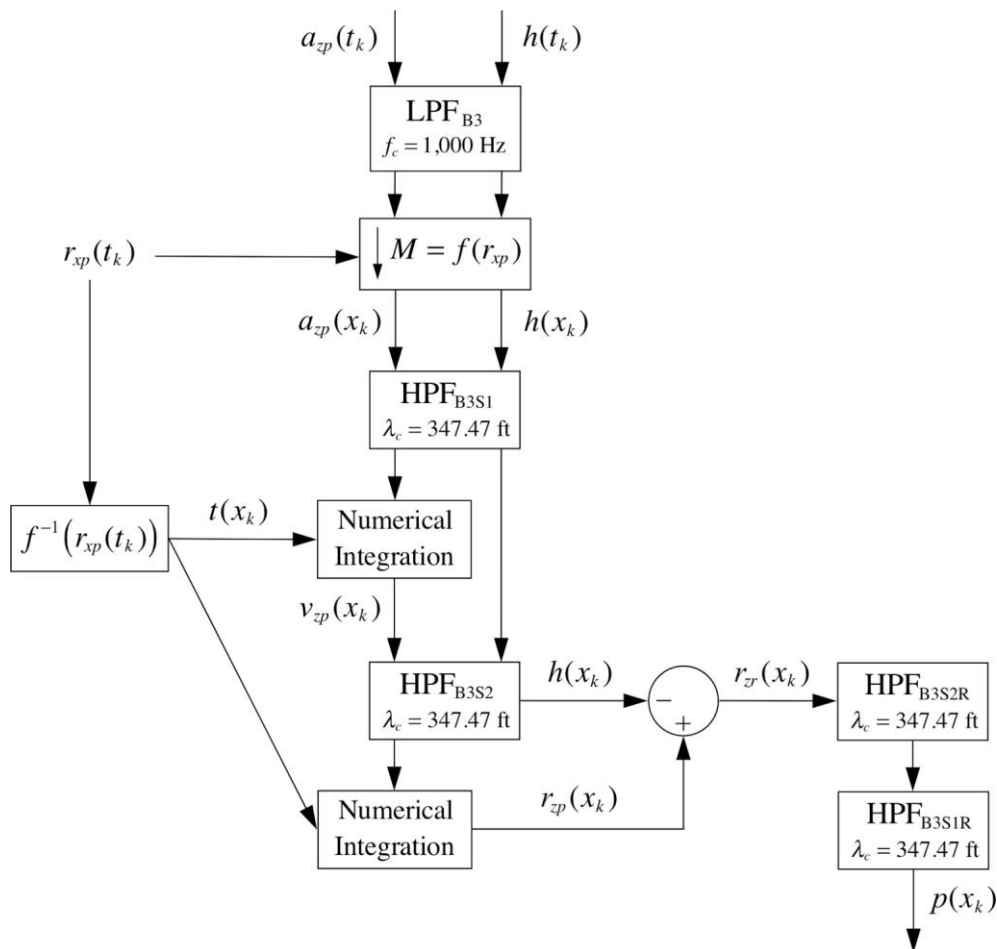
Figure 99. Block diagram. Spatial high-pass filtering, pre-integration.

In the spatial algorithms, the magnitude of the computed change in vertical position of the reference point during a stop no longer depends on the prevailing level of bias in the

accelerometer signal. Instead, it depends on the values from the accelerometer signal at the specific temporal samples when each spatial sample was established. All of the information about vehicle vibration between the distance samples is lost in the conversion to spatial coordinates. Together, the temporal gap in the spatial accelerometer signal and the large numerical value of time step used in the integration reduce the effectiveness of high-pass filtering.

Table 19 provides roughness and cross correlation results for profiles processed using the spatial algorithm with pre-integration high-pass filtering. High-pass filtering before integration consistently reduced the peak roughness values in runs with a stop. However, the level of reduction is somewhat arbitrary, since the artificial change in elevation at the location where the host vehicle stops depends primarily on the average of two accelerometer samples surrounding the stop. The influence of these accelerometer readings grows very large because they are multiplied by a large time step at each stage of integration.

Table 19. Results for the spatial algorithm with pre-integration high-pass filtering.

Run Designation	Peak Roughness (inches/mi)	Average Roughness Error (Percent)	Cross Correlation
S&G, 1.1-sec stop, 0.17 g	1,562	96.8	< 0.2
S&G, 1.1-sec stop, 0.20 g	4,810	295.1	< 0.2
S&G, 2.1-sec stop, 0.33 g	3,695	231.3	< 0.2
S&G, 5.8-sec stop, 0.17 g	16,035	1022.7	< 0.2
S&G, 5.7-sec stop, 0.20 g	27,429	1788.8	< 0.2
S&G, 5.8-sec stop, 0.20 g	9,875	616.4	< 0.2
S&G, 10.7-sec stop, 0.20 g	75,192	4946.6	< 0.2
NS, 45–7 mi/hr, 0.20 g	173	8.1	0.713
Brk, 44–19 mi/hr, 0.19 g	163	3.3	0.891
Brk, 45–18 mi/hr, 0.39 g	145	1.4	0.789
Brk, 31–14 mi/hr, 0.16 g	145	0.5	0.871
Brk, 31–14 mi/hr, 0.18 g	151	0.5	0.889
Brk, 31–14 mi/hr, 0.18 g	178	1.8	0.900
Brk, 31–12 mi/hr, 0.25 g	152	1.7	0.902
Brk, 30–21 mi/hr, 0.84 g	226	13.2	0.781
10 mi/hr	149	–1.0	**0.927**
3 mi/hr	175	14.5	0.746

Reference peak roughness value: 152 inches/mi. Adequate cross correlation (> 0.92) is shown in bold.

Spatial high-pass filtering reduced errors in peak roughness in the most severe cases among the braking runs, but increased peak roughness in others. This algorithm failed to produce cross correlation above the 0.92 threshold value in any of the test runs.

Table 18 and table 19 demonstrate that spatial high-pass filtering of the accelerometer signal, applied before or after integration, does not offer adequate performance. Large errors in roughness and very low cross correlation are shown for runs with a stop. Additional provisions are needed to address the artificial roughness at the stop caused by the large integration time step.

TIMER DISTORTION AND HEIGHT-SENSOR REFLECTION

Walker and Becker recommended timer distortion during low-speed profiler operation as a means to minimize "wide swings" that appear in computed profile during stop-and-go operation.[15] Timer distortion artificially adjusts the elapsed time between spatial samples in areas where the host vehicle travels at low speed. This approach offers a way to address the main weakness in the spatial high-pass filtering algorithm because it reduces the potentially large changes in elevation that occur over distance increments that are associated with a large time step. This section describes the application of a version of Walker's approach to the spatial high-pass filtering algorithm shown in figure 99.

This procedure replaces time interval associated with consecutive samples used for numerical integration (as shown in figure 97 and figure 98) with an adjusted value based on travel speed. At high host-vehicle speed, no adjustment is applied, and this procedure is equivalent to the pre-integration spatial high-pass filtering algorithm. At low speed, this algorithm imposes an artificial limit on the time step associated with each distance increment. This suppresses the magnitude of the changes in floating reference height after double integration.

The time interval used for numerical integration is unaffected at high speed and limited to a maximum value of Δt_0 at low speed, as shown in figure 100.

$$\Delta t_0 = \frac{\Delta x}{v_0}$$

Figure 100. Equation. Limit value for time interval.

In figure 100, Δx is the distance increment of the spatial profile and v_0 is a low-speed threshold. The adjusted time interval (Δt_{Adj}) is calculated based on the actual time interval (Δt) and the limit value as shown in figure 101.

$$\Delta t_{Adj} = \Delta t_0 \left(1 + \left(\frac{\Delta t}{\Delta t_0} \right) - \left(1 + \left(\frac{\Delta t}{\Delta t_0} \right)^{\beta} \right)^{1/\beta} \right)$$

Figure 101. Equation. Adjusted time interval.

The function in figure 101 returns an adjusted value of time step close to the actual value at high host-vehicle speed (i.e., low Δt). At very low speed, when the actual time interval is much larger, this function returns the limit value. The coefficient β determines the sharpness of the transition between the unaltered and limited ranges.

This implementation uses a value for β of 25 and Δt_0 of 0.0014205 seconds. The time interval threshold corresponds to a distance interval of 0.2 inches and a speed of 11.733 ft/s. Figure 102 shows the ratio of adjusted values to actual values of time interval as a function of speed. Note that the ratio shown in figure 102 approaches 1 as speed increases. At speeds of 10 mi/hr and above, the actual and adjusted time interval values agree to within 0.004 percent.
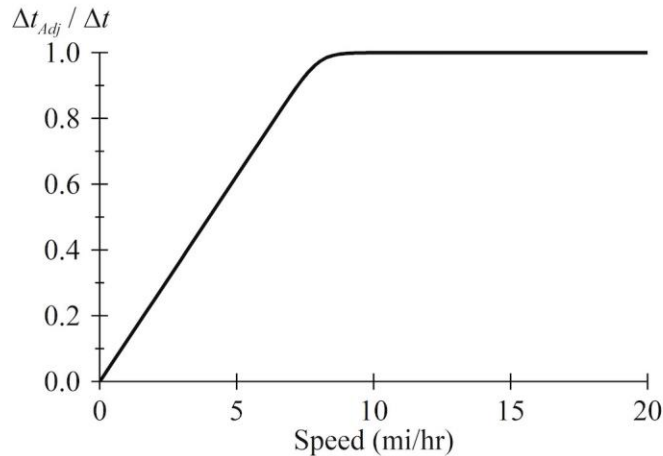
Figure 102. Graph. Timer adjustment versus speed

Table 20 provides roughness and cross correlation results for test runs with braking and stops using the spatial algorithm with high-pass filtering and timer distortion. (The adjusted time interval is virtually equal to the actual time interval in the braking runs, and their results are the same as in table 19.) Timer distortion greatly reduces the peak roughness values for the runs with stops by removing the large artificial change in height of the profiler reference point. For example, in the run with the 10.7-second-long stop, the time difference between the readings surrounding the stop was adjusted from 10.7643 to 0.0014205 seconds. This, and the change to the integrated accelerometer signal leading to the stop, reduced the magnitude of the step change in height of the profiler reference point from 9.017 ft to 0.00035 inches.

Table 20. Results for stops and the near stop, timer distortion.

Run Designation	Peak Roughness (inches/mi)	Average Roughness Error (Percent)	Cross Correlation
S&G, 1.1-sec stop, 0.17 g	553	31.4	0.327
S&G, 1.1-sec stop, 0.20 g	820	45.8	0.230
S&G, 2.1-sec stop, 0.33 g	1,139	66.3	< 0.2
S&G, 5.8-sec stop, 0.17 g	612	36.5	0.263
S&G, 5.7-sec stop, 0.20 g	824	46.6	< 0.2
S&G, 5.8-sec stop, 0.20 g	877	54.0	0.208
S&G, 10.7-sec stop, 0.20 g	867	52.4	0.236
NS, 45–7 mi/hr, 0.20 g	221	10.9	0.609

Reference peak roughness value: 152 inches/mi. Adequate cross correlation > 0.92.

Timer distortion greatly reduced peak roughness on runs with a stop relative to the spatial algorithms without timer distortion. However, the peak roughness values remain more than three times the reference values in all of those runs, and the cross correlation values were all well below the threshold value of 0.92. Further provisions are needed to suppress artificial localized roughness at stops.

The remaining artificial localized roughness in the runs with a stop is caused by a step change between the height-sensor readings surrounding the stop. Figure 103 shows the floating-reference-height signal and height-sensor signal for the run with a 10.7-second-long stop. The

stop occurred 710.3 ft from the start of the test section. Timer distortion removed the large change in the floating-reference-height signal at the stop and attenuated the fluctuations in the signal in the region near the stop (704 ft to 719 ft).
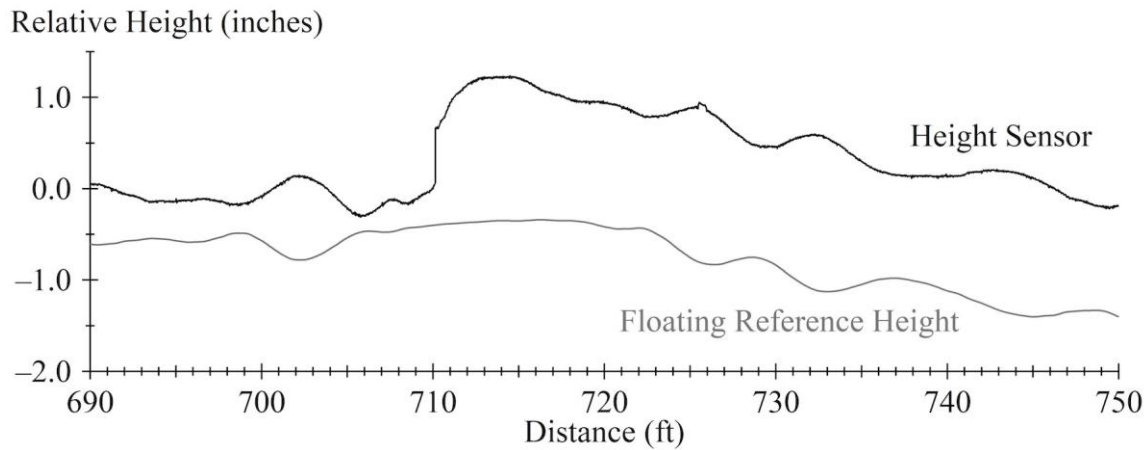
Figure 103. Graph. Height-sensor and floating-reference-height signals, timer distortion.

As shown in figure 103, the height sensor detected a 0.6-inch change in road height relative to the profiler during the stop. This indicates a net downward motion of the profiler over the 10.7 seconds that elapsed between distance samples, due primarily to settling of pitch motion caused by deceleration leading to the stop. The floating-reference-height signal, which was attenuated at the stop by timer distortion, does not properly detect this aspect of vehicle motion or the dynamics detected by the height sensor in the area surrounding the stop. Similarly, timer distortion caused the peak roughness to increase in the run with a near stop due to a lack of cancellation of content from the height sensor.

Walker and Becker passed the computed profile through a "slew" to mitigate the cancellation error caused by attenuating the floating-reference-height signal.[15] The slew limited the rate of change in elevation of the profile near the stop. The method applied here superimposes fluctuations onto the floating-reference-height signal that are equal and opposite to those of the height-sensor signal in the attenuated area.

This procedure is based on the assumption that the floating-reference-height signal is not valid in the area near the stop, and that removing the roughness from the profile in this area is preferable to introducing artificial roughness. In this procedure, the equation shown in figure 104 replaces the second stage of integration of the accelerometer signal.

$$r_{zp}(x_k) = r_{zp}(x_{k-1}) + \Delta t_{Adj}(x_k)\left(v_{zp}(x_k) + v_{zp}(x_{k-1})\right) - \left(1 - \left(\frac{\Delta t_{Adj}(x_k)}{\Delta t(x_k)}\right)^2\right)\left(h(x_k) - h(x_{k-1})\right)$$

Figure 104. Equation. Second stage of numerical integration with height-sensor reflection.

In figure 101, the second term after the equal sign represents integration using the adjusted time interval. Since this algorithm also applies the adjusted time interval in the first stage of integration, fluctuations in the floating-reference-height signal are reduced in proportion to the

square of $\Delta t_{Adj}/\Delta t$. The third term after the equal sign imposes the opposite of changes that appear in the height-sensor signal. This term is scaled in proportion to attenuation imposed on the accelerometer signal.

Figure 105 shows the height-sensor signal and the adjusted floating-reference-height signal produced by this process for the run with the 10.7-second-long stop. In the region near the stop (704 ft to 719 ft), the adjusted time interval is below the actual time interval and the floating-reference-height signal includes reflected content from the height sensor. In this region, the content cancels and the profile is essentially flat. However, a rapid change in slope appears in the profile at the end of the affected region, which registers as roughness.
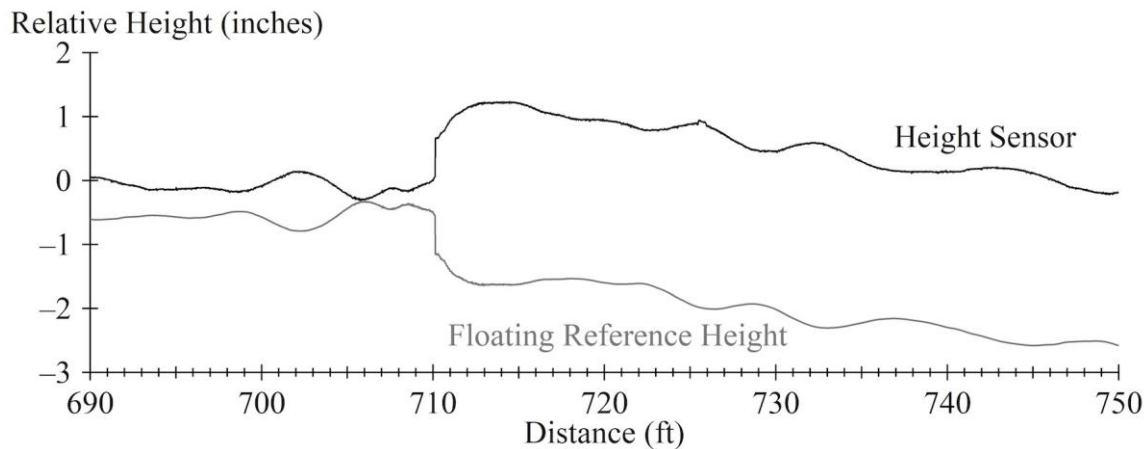
Figure 105. Graph. Height-sensor and floating-reference-height signals, timer distortion and height-sensor reflection.

Table 21 lists roughness and cross correlation results for test runs at low speed, with stops, and with a near stop using the spatial algorithm with high-pass filtering, timer distortion, and height-sensor reflection. Together, these provisions reduced the peak roughness values to a small fraction of those produced by the basic spatial algorithm. Cross correlation values are greatly improved, yet well below the 0.92 threshold value.

Table 21. Results for stops and the near stop, timer distortion and height-sensor reflection.

Run Designation	Peak Roughness (inches/mi)	Average Roughness Error (Percent)	Cross Correlation
S&G, 1.1-sec stop, 0.17 g	263	7.4	0.693
S&G, 1.1-sec stop, 0.20 g	275	7.5	0.702
S&G, 2.1-sec stop, 0.33 g	291	11.7	0.587
S&G, 5.8-sec stop, 0.17 g	281	12.3	0.616
S&G, 5.7-sec stop, 0.20 g	244	6.2	0.696
S&G, 5.8-sec stop, 0.20 g	306	13.8	0.652
S&G, 10.7-sec stop, 0.20 g	300	11.8	0.678
NS, 45–7 mi/hr, 0.20 g	146	3.4	0.756
10 mi/hr	149	–1.0	**0.927**
3 mi/hr	21	–86.6	< 0.2

Reference peak roughness value: 152 inches/mi. Adequate cross correlation (> 0.92) is shown in bold.

The provisions used to suppress errors at the stop removed more than 85 percent of the valid roughness in the test run at 3 mi/hr. Note that adjustment of the speed threshold to capture more valid profile content for constant-speed runs at low speed reduced error suppression at stops.

Overall, spatial high-pass filtering combined with timer distortion and height-sensor reflection greatly reduced the artificial localized roughness registered at stops. However, this reduction was achieved at the cost of valid profile measurement at very low speed. In particular, the profile measured at 3 mi/hr was completely invalid. Further, runs with a stop correlated poorly to the reference runs, because of missing profile content in the vicinity of the stop.

SUMMARY

This chapter presented algorithms for suppressing artificial localized roughness at locations where an inertial profiler host vehicle brakes, stops, or operates at low speed. The chapter examined each algorithm using only the sensors that appear in a typical commercial profiler.

As a baseline, the chapter presented results for basic profile calculation algorithms that use methods found in common practice. This included a basic temporal algorithm and a basic spatial algorithm. Both of the basic algorithms demonstrated errors in profile and roughness measurement at low speed, during braking, and at stops. This included very large errors in roughness for runs with a stop, including extremely high values of peak roughness in the location of the stop.

Application of high-pass filters to the accelerometer signal before each stage of integration (i.e., "temporal high-pass filtering, pre-integration") demonstrated adequate performance for runs at low speed and a majority of runs with braking. This algorithm greatly reduced the error in roughness measurement for runs with stops, but large errors in roughness remained. The stages of this algorithm that occur before decimation to the distance domain do not run in real time, and storage of the temporal profile and distance encoder output in the time domain are required.

Modification of the temporal high-pass filter to use an adaptive cut-off frequency reduced errors in roughness measurement at stops further. However, the performance for runs with stops was not adequate, and the improvement came at the cost of errors in measurement of profile at very low speed. This filter enforces a limit of cut-off wavelength at high speed and a limit of cut-off frequency at low speed. This adaptation allows for application of the filter in the time and distance domain. Application of a backward-running filter after digitizing the profile to a constant distance interval cancelled the phase shift associated with the forward-running (temporal) filter applied to the sensor signals. Applying the backward pass in the distance domain avoids the burden of storing any time-domain signals.

Pre-integration high-pass filtering was not as effective in the spatial profile calculation algorithm. Digitizing the accelerometer signal to a constant distance step before filtering and integration removes an opportunity for effective removal of drift in the integrated signals. Further, it causes the integrator to use a very large time step for the distance interval that includes the stop.

A specialized version of an algorithm recommended by Walker and Becker is proposed here that includes pre-integration high-pass filtering, temporal distortion at very low speed, and height-

sensor reflection at very low speed.[15] Together, these provisions remove profile content at very low speed without introducing a large step change in elevation or slope, and rapid changes in curvature are minimized. As a result, errors in roughness measured at stops are greatly reduced. However, the performance for runs with stops was not adequate, and the improvement came at the cost of errors in measurement of profile at very low speed.

These algorithms establish performance limits that can be attained without adding sensors to the nominal commercial profiler design. The adaptive pre-integration high-pass filtering algorithm is recommended for profilers with temporal profile calculation architecture. The pre-integration high-pass filtering algorithm with temporal distortion and height-sensor reflection is recommended for profilers with spatial profile calculation architecture. Neither algorithm offers adequate performance during braking or at stops, nor are they capable of roughness measurement at speeds below 10 mi/hr. However, they both reduce errors in roughness measurement from a factor of 10 and above to 20 percent and below.

These algorithms are only recommended for error mitigation when the resources are not available for adding sensors. Chapter 6 demonstrates a profiler design that achieves adequate performance using additional sensors.

CHAPTER 6: SENSOR AUGMENTATION

This chapter describes the use of additional sensors to improve inertial profiler performance at very low speed, during braking, and in stop-and-go operation. Like a strap-down inertial navigation system, the augmented profiler uses measurements from body-fixed accelerometers and rate gyroscopes in three dimensions to calculate position of the profiler reference point. In this application, only the change in vertical position of the profiler reference point is of interest. However, measurements are needed in three dimensions to resolve body-fixed acceleration into a truly vertical direction (i.e., aligned with gravity).

A multi-rate extended Kalman filter with a Rauch-Tung-Striebel (RTS) smoother eliminates drift in the integrated acceleration and rate signals using GPS measurements of host-vehicle height, vertical velocity, pitch, and roll. In the Kalman filter, the core of the process includes kinematic resolution of acceleration into the vertical direction, as well as integration of acceleration and rate of rotation to obtain position and orientation. Measurements of acceleration and rate of rotation drive the system, and determine its high-frequency output. The GPS sensors provide an absolute reference, and establish the low-frequency output of the system and impose a limit on integrator drift.

This application required a multi-rate implementation, because the frequency range of interest exceeded the waveband of the outputs from the GPS. Further, the inertial sensors provided inputs at 16,000 Hz, whereas the GPS provided observations at 20 Hz. Additionally, this application required a Kalman smoother to help eliminate drift in the floating-reference-height signal that occurred during braking, particularly near stops.

The Kalman smoother produced better reproduction of the reference profile measurement during braking and at stops than the error suppression algorithms proposed in Chapter 5. Unlike the error suppression algorithms, the smoother demonstrated improvement in profile measurement at low speed. Adaptation of the Kalman filtering stage to use the height sensor in place of the GPS outputs at speeds below 0.1 mi/hr further reduced profile measurement error at stops. Additional implementations of the Kalman smoother that do not depend on GPS measurements are demonstrated for cases in which GPS readings are unavailable.

The chapter presents a review of Kalman filtering, the RTS smoother, and relevant kinematics of rotating and accelerating reference frames. The chapter also presents the system equations used in this application of the Kalman filter and smoother, and estimates of system and measurement noise. Five implementations of the Kalman filter and smoother are demonstrated. The performance of each is presented for test runs at low speed, with braking, and with stops. Results are quantified using cross correlation to profile measured in a reference test run and comparison of IRI values.

THE KALMAN FILTER

The Kalman filter is an optimal state estimation algorithm, which was originally proposed for prediction of random signals and separation of random signals from noise.[94–96] The algorithm combines discrete-time models of system and sensor dynamics with statistical descriptions of system noise and measurement errors to estimate the system state.[97] In this manner, the Kalman

filter infers values of state variables that are not measured directly or are measured imperfectly. State estimates are optimal in that the Kalman filter minimizes the estimated error covariance, so long as the system is linear with additive Gaussian noise in both the system dynamics and the measurement.[98,99] The Kalman filter is recursive, in that it updates estimates of the state using a weighted average of the previous state estimate and new values based on the latest measurement data.[100] The relative efficiency of the recursive approach has lead to broad application in numerous fields, including as terrestrial navigation.[98,101]

Welch and Bishop provide an introductory description of the Kalman filter and the extended Kalman filter.[98] Portions of those descriptions are summarized here with changes in notation.

Linear Kalman Filter

The Kalman filter estimates the state recursively for a linear stochastic system in state space form, as shown in figure 106.

$$x_k = A_{k-1}x_{k-1} + B_{k-1}u_{k-1} + w_{k-1}$$
$$y_k = H_k x_k + v_k$$

Figure 106. Equations. Kalman filter, discrete linear system equations.

In figure 106, the subscript k represents the time step. If the system has ns state variables, is monitored by nm measurements, and is driven by ni inputs, then: $x_k \in \Re^{ns \times 1}$ is the state, $u_{k-1} \in \Re^{ni \times 1}$ is the input, and $y_k \in \Re^{nm \times 1}$ is the output (i.e., measurements). The system equation includes a state transition matrix $A_{k-1} \in \Re^{ns \times ns}$ and an input matrix $B_{k-1} \in \Re^{ns \times ni}$. The measurement equation includes an observation matrix $H_k \in \Re^{ns \times nm}$, which relates the state to the available measurements.

The system includes independent zero-mean, Gaussian process noise $w_{k-1} \in \Re^{ns \times 1}$ and independent zero-mean, Gaussian measurement noise $v_k \in \Re^{nm \times 1}$, as described in figure 107 and figure 108.

$$p(w) \sim \mathcal{N}(0, \sigma_w^2)$$

Figure 107. Equation. Zero mean Gaussian process noise.

$$p(v) \sim \mathcal{N}(0, \sigma_v^2)$$

Figure 108. Equation. Zero mean Gaussian measurement noise.

The Kalman filtering equations do not include the noise signals directly. Rather, they incorporate noise using the process noise covariance matrix $Q_{k-1} \in \Re^{ns \times ns}$ and the measurement noise covariance matrix $R_k \in \Re^{nm \times nm}$, as defined in figure 109.

$$Q_{k-1} = \varepsilon\{w_{k-1}w_{k-1}^T\}$$
$$R_k = \varepsilon\{v_k v_k^T\}$$

Figure 109. Equations. Process and measurement noise covariance matrices.

At each time step the Kalman filter performs a *time update* and a *measurement update*. The time update makes the best possible estimate of the state at time step k, given the sequence of inputs and measurements up to time step k–1 and the known system dynamics, as shown in figure 110.

$$\hat{x}_{k|k-1} = A_{k-1}\hat{x}_{k-1|k-1} + B_{k-1}u_{k-1}$$
$$P_{k|k-1} = A_{k-1}P_{k-1|k-1}A_{k-1}^{T} + Q_{k-1}$$

Figure 110. Equations. Kalman filter time update.

In figure 110, $\hat{x}_{k|k-1}$ is the *a priori* (i.e., predicted) estimate of x_k and $P_{k|k-1} \in \mathfrak{R}^{ns \times ns}$ is the *a priori* estimate of the error covariance at time step k. Figure 111 provides the expression for the error covariance matrix.

$$P_{k|k-1} = \mathcal{E}\{(x_k - \hat{x}_{k|k-1})(x_k - \hat{x}_{k|k-1})^{T}\}$$

Figure 111. Equation. Error covariance matrix.

The measurement update refines the estimates of the state and the error covariance at time step k using the measurements at time step k and the predictions produced in the time update, as shown in figure 112.

$$K_k = P_{k|k-1}H_k^{T}(H_k P_{k|k-1}H_k^{T} + R_k)^{-1}$$
$$\hat{x}_{k|k} = \hat{x}_{k|k-1} + K_k(y_k - H_k\hat{x}_{k|k-1})$$
$$P_{k|k} = (I - K_k H_k)P_{k|k-1}$$

Figure 112. Equations. Kalman filter measurement update.

Figure 112 shows the equations for the measurement update, where $\hat{x}_{k|k}$ and $P_{k|k}$ are the *a posteriori* (i.e., corrected) estimates of x_k and P_k, respectively. The matrix $K_k \in \mathfrak{R}^{ns \times nm}$ is the Kalman gain, and is often referred to as the blending factor. The Kalman gain determines the relative influence of measurements and system dynamics in the refined state estimate. The Kalman gain is optimal, because it minimizes the mean square state estimation error by minimizing the trace of the error covariance matrix.

The filter typically runs from $k=1$ to N, where N is the number of time steps. At the first time step, initial estimates of the state vector $\hat{x}_{0|0}$ and error covariance matrix $P_{0|0}$ take the place of the previous measurement update. Note that, for the linear Kalman filter, the subscripts on A, B, w, H, v, Q, and R only appear to accommodate time-variant systems.

Extended Kalman Filter

The extended Kalman filter estimates the state for a non-linear discrete time process, as shown in figure 113. Where f is a set of *nn* non-linear functions in the state equation, and h is a set of *nm* non-linear functions in the measurement equation. Like the linear Kalman filter, the extended Kalman filter includes a time update and a measurement update.

$$x_k = f(x_{k-1}, u_{k-1}, w_{k-1})$$
$$y_k = h(x_k, v_k)$$

Figure 113. Equations. Extended Kalman filter system equations.

The time update estimates the state using non-linear system equations, as shown in figure 114.

$$\hat{x}_{k|k-1} = f(\hat{x}_{k-1|k-1}, u_{k-1}, 0)$$

Figure 114. Equation. Extended Kalman filter state estimates.

However, the estimate of the state error covariance depends on linearized versions of the state transition matrix A and process noise matrix W, as shown in figure 115. Where $A_{k-1} \in \mathfrak{R}^{ns \times ns}$ is a Jacobian matrix of partial derivatives of f with respect to the system state, as shown in figure 116.

$$P_{k|k-1} = A_{k-1} P_{k|k-1} A_{k-1}^T + W_{k-1} Q_{k-1} W_{k-1}^T$$

Figure 115. Equation. Extended Kalman filter state error covariance estimates.

$$A_{k-1}[i,j] = \frac{\partial f[i]}{\partial x[j]}(\hat{x}_{k-1|k-1}, u_{k-1}, 0)$$

Figure 116. Equation. Extended Kalman filter linearized A matrix.

Note that a one-to-one mapping may not exist between process noise terms and state variables. As such, the process noise covariance matrix, $Q_{k-1} \in \mathfrak{R}^{nn \times nn}$, corresponds to nn noise terms, and $W_{k-1} \in \mathfrak{R}^{ns \times nn}$ is a Jacobian matrix of partial derivatives of f with respect to process noise, as shown in figure 117.

$$W_{k-1}[i,j] = \frac{\partial f[i]}{\partial w[j]}(\hat{x}_{k-1|k-1}, u_{k-1}, w_{k-1})$$

Figure 117. Equation. Extended Kalman filter linearized W matrix.

The measurement update incorporates the non-linear measurement equation, but the Kalman matrix and state error covariance updates depend on linearization of the measurement equation, as shown in figure 118. Figure 119 and figure 120, respectively, provide expressions for the linearized H and V matrix.

$$K_k = P_{k|k-1} H_k^T (H_k P_{k|k-1} H_k^T + V_k R_k V_k^T)^{-1}$$
$$\hat{x}_{k|k} = \hat{x}_{k|k-1} + K_k(y_k - h(\hat{x}_{k|k-1}, 0))$$
$$P_{k|k} = (I - K_k H_k) P_{k|k-1}$$

Figure 118. Equations. Extended Kalman filter measurement update.

$$H_k[i,j] = \frac{\partial h[i]}{\partial x[j]}(\hat{x}_{k|k-1}, 0)$$

Figure 119. Equation. Extended Kalman filter linearized H matrix.

$$V_k[i,j] = \frac{\partial h[i]}{\partial v[j]}(\hat{x}_{k|k-1}, v_k)$$

Figure 120. Equation. Extended Kalman filter linearized V matrix.

Each element in the matrices *A*, *W*, *H* and *V* are linearized using the first term in the Taylor expansion. Since they are evaluated using the most recent input and the most recent available estimates of the state, they change with time. With this formulation, the filter is linearized about the estimated system trajectory.[101] This has three consequences relative to the standard Kalman filter. First, the covariance estimates change with changes in system dynamics, even with constant estimates of system and measurement noise. As such, the Kalman gain and state error covariance matrix must be evaluated at every time step.[99] Second, convergence of the filter is not guaranteed. Third, the extended Kalman filter is not optimal, because propagating Gaussian random variables through the non-linear equations does not always produce Gaussian outputs. This violates the assumptions in the minimization of state error covariance.[98]

Multi-Rate Kalman Filter

The Kalman filtering application described in this chapter applies the process model (i.e., the dynamical equations) at a higher rate than the updates prompted by observations. This is because the sensors detect system inputs (e.g., acceleration, rate of rotation) at a higher rate than measurements used to adjust the state estimates (e.g., GPS position, velocity, and orientation). As such, the measurement update is only applied when an observation is available. At time steps with no corresponding observation, the a posteriori estimates of x_k and P_k are equal to the a priori estimates, as shown in figure 121.

$$\hat{x}_{k|k} = \hat{x}_{k|k-1}$$
$$P_{k|k} = P_{k|k-1}$$

Figure 121. Equations. A posteriori estimates with no measurements.

Jones, and Cipra and Romero established this procedure as optimal for linear systems.[102,103] Smyth and Wu demonstrated the efficacy of this approach for multi-rate Kalman filters that estimate position based on integrated acceleration.[104]

Kalman Smoother

The Kalman filter estimates current and future values of state variables based only on existing measurements, whereas a smoother applies the available measurements to past values.[105] That is, the smoother improves the state estimates at a given time using measurements that occur afterward.[104,106] The improvement comes at the cost of reduced computational efficiency. Further, the possibility of obtaining state estimates in real time is lost.

The RTS smoother "starts with the filtered estimate at the last point and calculates backward point by point determining the smoothed estimate as a linear combination of the filtered estimate at that point and the smoothed estimate at the previous point."[105] This procedure requires the application of a Kalman filter over a specified time interval; followed by a backward pass to improve the state estimates based on statistics influenced by all of the available measurements.

Meditch describes this as *fixed-interval smoothing*.[107] (See Brown and Huang or Aslan for straightforward descriptions of the numerical procedure.[101,108])

For an interval including N time steps, the smoothing stage runs backward from time step $N–1$ to 1. The smoothed state estimates, $\hat{x}_{k|N}$, are computed recursively as shown in figure 122.

$$\hat{x}_{k|N} = \hat{x}_{k|k} + L_k(\hat{x}_{k+1|N} - \hat{x}_{k+1|k})$$

$$L_k = P_{k/k}A_k^T P_{k+1/k}^{-1}$$

Figure 122. Equations. Kalman smoother backward pass.

For a system with non-linear dynamics, A_k is a Jacobian matrix of partial derivatives of the state equations with respect to the system state, as shown in figure 123.

$$A_k[i,j] = \frac{\partial f[i]}{\partial x[j]}(\hat{x}_{k|k}, u_k, 0)$$

Figure 123. Equation. Kalman smoother linearized A matrix.

For the initial step in the backward pass ($k=N–1$), the smoothed versions of the state estimate, $\hat{x}_{N|N}$, and the state error covariance matrix, $P_{N|N}$, are obtained from the final step in the forward pass.

Note that the notation used for estimated state corresponds to the distinction between the outputs of the Kalman filter and the Kalman smoother. In the Kalman filter, $\hat{x}_{k+1|k}$ represents an estimate of the state at time step $k+1$, given the information available up to time step k. In the RTS Kalman smoother, $\hat{x}_{k+1|N}$ represents an estimate of the state at time step $k+1$, given the information available up to time step N (i.e., over the entire testing interval).

The smoother equations above require storage of the inputs; the a priori states and state error covariance matrix; and the a posteriori states and state error covariance matrix. Some of the storage burden is eliminated by redundantly calculating a priori variables using stored values of a posteriori variables and inputs, as shown in figure 124.

$$\hat{x}_{k+1|k} = f(\hat{x}_{k|k}, u_k, 0)$$

$$P_{k+1|k} = A_k P_{k|k} A_k^T + W_k Q_k W_k^T$$

$$W_k[i,j] = \frac{\partial f[i]}{\partial w[j]}(\hat{x}_{k|k}, u_k, w_k)$$

Figure 124. Equations. Kalman smoother redundant calculations.

The state error covariance for the smoothed state estimates is calculated as shown in figure 125.

$$P_{k|N} = P_{k|k} + L_k(P_{k+1|N} - P_{k+1|k})L_k^T$$

Figure 125. Equation. Kalman smoother state error covariance.

Calculation of the smoothed state estimates does not require knowledge of $P_{k|N}$.

COORDINATE REFERENCE FRAMES

Each rate gyroscope and accelerometer provides measurements relative to the inertial reference and resolved along their sensitive axes. This section introduces coordinate reference frames in support of discussions that follow of measurements and system dynamics. The axis systems defined here are dextral and orthogonal.

Inertial Frame (i): A non-rotating, non-accelerating reference frame with respect to distant stars with its origin fixed in the center of the Earth. Its Z-axis is aligned with the Earth's spin axis running northward.

Earth-Fixed Frame (e): A reference frame fixed in the Earth. Its origin and its Z-axis are coincident with the Inertial Frame. The Earth frame X-axis passes through the intersection of the plane of the Greenwich meridian with the equatorial plane.

Navigation Frame (n): A local geographic frame with its origin fixed at a reference point on the vehicle. The Z-axis is aligned with the gravity vector running upward. The X-axis and Y-axis are parallel to the ground plane, running eastward and northward, respectively.

Body Frame (b): A reference frame fixed in the sprung mass of a vehicle with its origin fixed at a reference point on the vehicle. The X-axis is parallel to the vehicle plane of symmetry running forward, and is approximately parallel to the road surface when the vehicle is at rest. The Y-axis is perpendicular to the vehicle plane of symmetry running leftward. The Z-axis runs upward, and is approximately perpendicular to the road surface.

Wander Frame (w): A reference frame whose Z-axis coincides with the navigation frame, and whose origin coincides with the body frame and the navigation frame. The X-axis and Y-axis are parallel to the ground plane. The X-axis is aligned with the vertical projection of the body X-axis into the ground plane.

The inertial frame and Earth-fixed frame are adopted from terrestrial navigation. The body frame and wander frame correspond to the vehicle and intermediate axis systems as defined in SAE J670, respectively.[91] The navigation frame is similar to the east-north-up navigation frame, except the horizontal plane is normal to gravity, rather than referenced to the Earth ellipsoid. A *reference point* is established for each of the left and right profilers where the sensitive axes of their vertical and longitudinal accelerometers intersect. For each profiler, the reference point is used as an origin for the navigation, wander, and body frames.

Coordinate Frame Rotation

Orientation of one coordinate frame relative to another is parameterized in this research using Euler angles for successive body-axis rotations. This is defined by yaw rotation (ψ) about the reference Z-axis, a pitch rotation (θ) about the reoriented Y-axis, and a roll rotation (ϕ) about the reoriented X-axis. A vector in the rotated frame, b, can be resolved to the un-rotated frame, n, as follows shown in figure 126. In figure 126, s and c represent sine and cosine functions,

respectively, of the angle that appears in the subscript. C^{nb} is the direction cosine matrix. Resolving a matrix in the reference system to the rotated system requires the transpose of C^{nb}, as shown in figure 127.

$$\vec{a}^n = \begin{bmatrix} c_\psi c_\theta & c_\psi s_\theta s_\phi - s_\psi c_\phi & c_\psi s_\theta c_\phi + s_\psi s_\phi \\ s_\psi c_\theta & s_\psi s_\theta s_\phi + c_\psi c_\phi & s_\psi s_\theta c_\phi - c_\psi s_\phi \\ -s_\theta & c_\theta s_\phi & c_\theta c_\phi \end{bmatrix} \vec{a}^b = C^{nb} \vec{a}^b$$

Figure 126. Equation. Vector transformation from frame b to frame n.

$$\vec{a}^b = (C^{nb})^T \vec{a}^n = C^{bn} \vec{a}^n$$

Figure 127. Equation. Vector transformation from frame n to frame b.

Formulation of the kinematic measurement equations and system dynamic equations required elements of the direction cosine matrix and their time derivatives. The time rate of change is caused by an instantaneous rate of rotation of frame b relative to frame n, which is defined in figure 128.

$$\vec{\omega}_{b/n}^b = \omega_x \hat{i}^b + \omega_y \hat{j}^b + \omega_z \hat{k}^b$$

Figure 128. Equation. Rate of rotation of frame b relative to frame n.

In figure 128, the subscript on the term to the left of the equal sign indicates rotation of the first frame relative to the second, and the vector is resolved into the frame that appears in the superscript.

The rate of change of the direction cosine matrix is given in figure 129, where $\Omega_{b/n}^b$ is the skew symmetric matrix that corresponds to the angular rate vector $\vec{\omega}_{b/n}^b$.[109]

$$\dot{C}^{nb} = C^{nb} \Omega_{b/n}^b = C^{nb} \begin{bmatrix} 0 & -\omega_z^b & \omega_y^b \\ \omega_z^b & 0 & -\omega_x^b \\ -\omega_y^b & \omega_x^b & 0 \end{bmatrix}$$

Figure 129. Equation. Rate of change of a direction cosine matrix.

The equation in figure 129 allows the expression of the rate of change of a direction cosine matrix element as a function of direction cosine matrix elements and angular rates measured in the rotated frame. In turn, the rate of change of the pitch and roll angle can be derived as shown in figure 130 and figure 131, respectively.

$$\dot{\theta} = c_\phi \omega_y^b - s_\phi \omega_z^b$$

Figure 130. Equation. Rate of change of pitch angle.

$$\dot{\phi} = \omega_x^b + s_\theta (s_\phi \omega_y^b + c_\phi \omega_z^b) / c_\theta$$

Figure 131. Equation. Rate of change of roll angle.

SYSTEM EQUATIONS

This section presents the system dynamics used by the Kalman filter. Prior work in sensor fusion for human and vehicle motion tracking guided the formulation of the process model and the sensor error modeling.[110,111] The purpose of the process model is estimation of changes in vertical position of the profiler reference point, r_{zp}^n, using inputs from body-mounted accelerometers and rate gyroscopes.

The state equations follow the same signal flow as a typical strap-down navigation system, as shown in figure 132. Three-dimensional measurements of specific force and rate of rotation by body-fixed sensors provide the means to derive vertical acceleration of the profiler reference point in the navigation frame. In turn, vertical acceleration is integrated twice to obtain relative vertical position. As described below, the measurement model compares independent measurements of height, vertical velocity, pitch inclination, and roll inclination to estimates from the state equations.
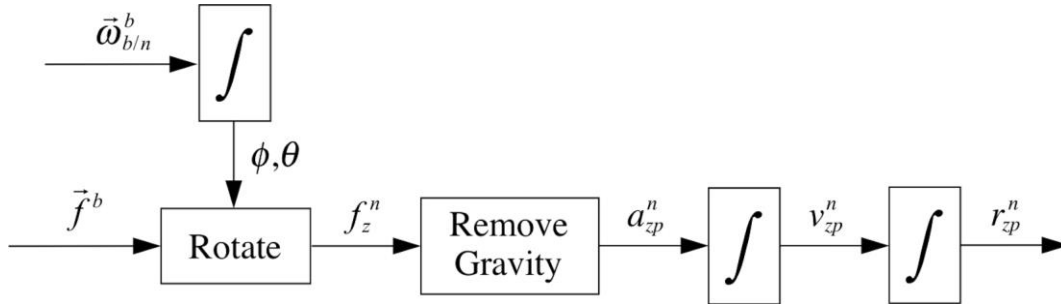
Figure 132. Block diagram. Process model signal flow.

Angular Rate

The angular rate vector, $\vec{\omega}$, of the body frame relative to the inertial frame can be expressed using the components shown in figure 133.

$$\vec{\omega}_{b/i}^b = C^{bn}(\vec{\omega}_{e/i}^n + \vec{\omega}_{n/e}^n) + \vec{\omega}_{w/n}^b + \vec{\omega}_{b/w}^b$$

Figure 133. Equation. Angular rate vector, body frame relative to inertial frame.

The rotation rate of the Earth relative to the inertial frame, $\vec{\omega}_{e/i}^n$, has a magnitude of approximately 7.3×10^{-5} rad/sec. The rate of rotation of the navigation frame relative to the Earth, which is the magnitude of $\vec{\omega}_{n/e}^n$, depends on the motion of the vehicle reference point with respect to the Earth. This is referred to as the *transport rate*.[112] For surface travel along a meridian at speeds below 100 mi/hr, the magnitude of the transport rate is less than 10 percent of the Earth rotation rate. For surface travel at speeds below 100 mi/hr along a circle of latitude below 82 degrees, the magnitude of the transport rate is below the Earth rotation rate.

In this formulation, the transport rate and the Earth's rotation rate are considered components of the time-varying bias, and output of the gyroscopes are interpreted as angular rate of the body-fixed frame relative to navigation frame.

The gyroscopes produce a measurement of each component of angular rate, u_ω, along their sensitive axis resolved into the body-fixed frame, as shown in figure 134. In figure 134, $\omega_{b/n}^b$ is considered the true angular rate, δ_ω accounts for slowly time-varying bias, and each component of e_ω accounts for additive Gaussian white noise measurement error.

$$u_\omega = \omega_{b/n}^b - \delta_\omega - e_\omega$$

Figure 134. Equation. Angular rate measurement.

Linear Acceleration

Acceleration of the profiler reference point at the navigation frame origin $\vec{a}_p$ as the Earth rotates relative to the inertial frame can be expressed as the sum of linear acceleration of the navigation frame relative to the Earth $\vec{a}_{n/e}$, Coriolis acceleration, and centrifugal acceleration. Figure 135 provides the equation for profiler reference point acceleration.

$$\vec{a}_p = \vec{a}_{n/e} + 2\vec{\omega}_{e/i} \times \vec{v}_{n/e} + \vec{\omega}_{e/i} \times \vec{\omega}_{e/i} \times \vec{p}_{n/e}$$

Figure 135. Equation. Profiler reference point acceleration.

At sea level, the centrifugal acceleration due to the Earth's rotation is limited to 0.0035 g. For horizontal or vertical motion at speeds below 100 mi/hr, the Coriolis acceleration is limited to 0.00066 g. In this formulation, centrifugal acceleration due to the Earth's rotation is considered a bias in the local gravity vector and Coriolis acceleration is considered a component of the slowly time-varying bias.

The accelerometers produce a measurement of each component of specific force, u_a, along their sensitive axis in the body-fixed frame, as shown in figure 136. Where f^b is the true specific force, δ_a^b is slowly time-varying bias, and each component of e_a^b is additive Gaussian white noise.

$$u_a = f^b + \delta_a^b + e_a^b$$

Figure 136. Equation. Acceleration measurement.

The specific force includes a contribution due to gravity. Figure 137 provides the expression for specific force written as a vector resolved into the body-fixed frame, and figure 138 represents the accelerometer measurements as a vector.

$$\vec{f}^b = C^{bn}(\vec{a}_{n/e}^n - \vec{g}^n)$$

Figure 137. Equation. Specific force vector.

$$\vec{u}_a = C^{bn}(\vec{a}^n_{n/e} - \vec{g}^n) + \vec{\delta}^b_a + \vec{e}^b_a$$

Figure 138. Equation. Acceleration measurement vector.

Rearranging this expression in figure 138 to obtain acceleration as a function of sensor output, gravity, and error terms produces the equation in figure 139. Only the vertical component is required for calculation of profiler reference point height. Figure 140 provides the expression for the vertical component of acceleration.

$$\vec{a}^n_{n/e} = C^{nb}(\vec{u}_a - \vec{\delta}^b_a - \vec{e}^b_a) + \vec{g}^n$$

Figure 139. Equation. Acceleration measurement in terms of sensor output.

$$a^n_{zp} = C^{nb}_{31}u_{ax} + C^{nb}_{32}u_{ay} + C^{nb}_{33}u_{az} + \delta_a + e_a - g$$

Figure 140. Equation. Vertical component of measured acceleration.

Only the third row of the direction cosine matrix is required to make this calculation, which only requires knowledge of the pitch and roll angle. In order to minimize the number of state in the system equation, this formulation uses pitch and roll angle directly, as shown in figure 141.

$$a^n_{zp} = -s_\theta u_{ax} + c_\theta s_\phi u_{ay} + c_\theta c_\phi u_{az} + \delta_a + e_a - g$$

Figure 141. Equation. Measured vertical acceleration in terms of pitch and roll.

This expression combines terms for accelerometer noise and time-varying bias from each sensor into a consolidated error model. The consolidated error terms correspond to vertical acceleration in the navigation reference frame. These terms incorporate the influence of input measurement errors, errors in sensor mounting and alignment, numerical approximation errors, local fluctuations in the acceleration due to gravity, etc.

Sensor Drift

Slowly varying bias in the roll rate, pitch rate, and the resultant vertical acceleration all modeled using random walk with the discrete representation shown in figure 142.

$$\delta_{a,k+1} = \delta_{a,k} + e_{a',k}$$
$$\delta_{\omega_1,k+1} = \delta_{\omega_1,k} + e_{\omega'_1,k}$$
$$\delta_{\omega_2,k+1} = \delta_{\omega_2,k} + e_{\omega'_2,k}$$

Figure 142. Equations. Discrete representations of random walk.

Since the system dynamics do not require a measure of yaw angle, no random walk is assigned to yaw rate.

GPS Position and Velocity

The system includes height and vertical velocity measured by a GPS using an antenna mounted to the host-vehicle body. Figure 143 shows a schematic of the measurement system hardware in

the rear view with some roll of the body frame relative to the navigation frame. The figure shows the position of the GPS antenna relative to the profiler reference point $\vec{r}^b_{gps/p}$, which is considered constant in the body-fixed frame.
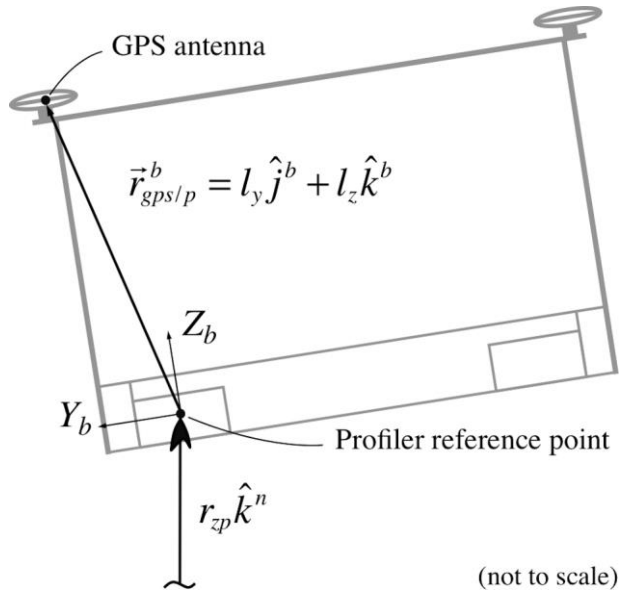
Figure 143. Schematic. GPS antenna offset, rear view.

Figure 144 shows the vertical offset of the GPS antenna relative to the profiler reference point in the navigation frame. The vertical offset is a function of elements of the direction cosine matrix that depend on pitch and roll rotation and the locally horizontal (l_y) and locally vertical offset (l_z) of the GPS antenna. Figure 145 shows the vertical velocity of the GPS antenna relative to the profiler reference point is.

$$\vec{r}^b_{gps/p} \cdot \hat{k}^n = C^{nb}_{32} l_y + C^{nb}_{33} l_z$$

Figure 144. Equation. GPS antenna vertical offset.

$$\vec{v}^n_{gps/p} \cdot \hat{k}^n = \dot{C}^{nb}_{32} l_y + \dot{C}^{nb}_{33} l_z = C^{nb}_{31}(\omega_y l_z - \omega_z l_y) - C^{nb}_{32} \omega_x l_z + C^{nb}_{33} \omega_x l_y$$

Figure 145. Equation. GPS antenna relative vertical velocity.

Figure 146 shows the model for measured GPS height, y_{rz}, and figure 147 shows the model for measured GPS vertical velocity, y_{vz}.

$$y_{rz} = r^n_{zp} + c_\theta(s_\phi l_y + c_\phi l_z) + e_{rz}$$

Figure 146. Equation. GPS height measurement model.

$$y_{vz} = v^n_{zp} + s_\theta(\omega_z l_y - \omega_y l_z) + c_\theta \omega_x(c_\phi l_y - s_\phi l_z) + e_{vz}$$

Figure 147. Equation. GPS velocity measurement model.

In figure 146 and figure 147, r^n_{zp} and v^n_{zp} are height and velocity of the profiler reference point relative to the Earth ellipsoid expressed in the navigation (and wander) frame. Each measurement

102

includes independent Gaussian white noise (e_{rz} and e_{vz}). The additional terms are required to calculate the vertical offset between the profiler reference point and the GPS antenna.

GPS Pitch and Roll

Figure 65 shows a schematic of the GPS-based attitude measurement system. (See Chapter 3.) A master antenna is placed at the rear left corner of the vehicle. A "pitch rover" antenna appears forward of the master antenna, and is aligned with it in the body-fixed longitudinal (X) direction. A "roll rover" antenna appears rightward of the master antenna, and is aligned with it in the body-fixed lateral (Y) direction. The GPS-based attitude measurement system provides inclination of the body-fixed X-axis and Y-axis relative to the horizontal plane. For each axis, inclination is positive when the rover antenna is above the master antenna.

Inclination of the X-axis (θ_{gps}) is equivalent to the Euler pitch angle, as shown in figure 148. Euler rotation in both pitch and roll of the body-fixed axis system relative to the navigation system affect inclination of the Y-axis (ϕ_{gps}). The equation in figure 149 relates roll inclination to the Euler angles.

$$\theta_{gps} = \theta$$

Figure 148. Equation. Pitch inclination and Euler pitch angle.

$$\phi_{gps} = \sin^{-1}(c_\theta s_\phi)$$

Figure 149. Equation. Roll inclination and Euler roll angle.

Figure 150 and figure 151 provide the measurement models for GPS pitch and roll inclination, respectively. Each measurement includes independent Gaussian white noise (e_θ and e_ϕ).

$$y_\theta = \theta + e_\theta$$

Figure 150. Equation. GPS pitch inclination measurement model.

$$y_\phi = \sin^{-1}(c_\theta s_\phi) + e_\phi$$

Figure 151. Equation. GPS roll inclination measurement model.

Discrete System Equations

The process model includes seven state variables ($r_{zp}^n, v_{zp}^n, \theta, \phi, \delta_a, \delta_{\omega_1}, \delta_{\omega_2}$) and seven system error terms ($e_a, e_{\omega_1}, e_{\omega_2}, e_{\omega_3}, e_{a'}, e_{\omega_1'}, e_{\omega_2'}$). Figure 152 presents the equations for the process model in discrete form.

$$r^n_{zp,k} = r^n_{zp,k-1} + v^n_{zp,k-1}\Delta t$$
$$+ (-s_{\theta_{k-1}} u_{ax,k-1} + c_{\theta_{k-1}} s_{\phi_{k-1}} u_{ay,k-1} + c_{\theta_{k-1}} c_{\phi_{k-1}} u_{az,k-1} + \delta_{a,k-1} + e_{a,k-1} - g)\Delta t^2 / 2$$
$$v^n_{zp,k} = v^n_{zp,k-1} + (-s_{\theta_{k-1}} u_{ax,k-1} + c_{\theta_{k-1}} s_{\phi_{k-1}} u_{ay,k-1} + c_{\theta_{k-1}} c_{\phi_{k-1}} u_{az,k-1} + \delta_{a,k-1} + e_{a,k-1} - g)\Delta t$$
$$\theta_k = \theta_{k-1} + \left(c_{\phi_{k-1}}(u_{\omega_2,k-1} + \delta_{\omega_2,k-1} + e_{\omega_2,k-1}) - s_{\phi_{k-1}}(u_{\omega_3,k-1} + e_{\omega_3,k-1}) \right)\Delta t$$
$$\phi_k = \phi_{k-1} + (u_{\omega_1,k-1} + \delta_{\omega_1,k-1} + e_{\omega_1,k-1})\Delta t$$
$$+ t_{\theta_{k-1}} \left(s_{\phi_{k-1}}(u_{\omega_2,k-1} + \delta_{\omega_2,k-1} + e_{\omega_2,k-1}) + c_{\phi_{k-1}}(u_{\omega_3,k-1} + e_{\omega_3,k-1}) \right)\Delta t$$
$$\delta_{a,k} = \delta_{a,k-1} + e_{a',k-1}$$
$$\delta_{\omega_1,k} = \delta_{\omega_1,k-1} + e_{\omega'_1,k-1}$$
$$\delta_{\omega_2,k} = \delta_{\omega_2,k-1} + e_{\omega'_2,k-1}$$

Figure 152. Equations. Process model discrete equations.

In figure 152, Δt is the interval between time steps, and index for time step (e.g., k or k—1) is appended to the subscript of any quantity that varies with time.

The measurement model includes four measurements $(y_{rz}, y_{vz}, y_\theta, y_\phi)$, and four measurement error terms $(e_{rz}, e_{vz}, e_\theta, e_\phi)$. Figure 153 presents the equations for the measurement model in discrete form.

$$y_{rz,k} = r^n_{zp,k} + c_{\theta_k}(s_{\phi_k} l_y + c_{\phi_k} l_z) + e_{rz,k}$$
$$y_{vz,k} = v^n_{zp,k} + s_{\theta_k}(u_{\omega_3,k} l_y - (u_{\omega_2,k} + \delta_{\omega_2,k}) l_z) + c_{\theta_k}(u_{\omega_1,k} + \delta_{\omega_1,k})(c_{\phi_k} l_y - s_{\phi_k} l_z) + e_{vz,k}$$
$$y_{\theta,k} = \theta_k + e_{\theta,k}$$
$$y_{\phi,k} = \sin^{-1}(c_{\theta_k} s_{\phi_k}) + e_{\phi,k}$$

Figure 153. Equations. Measurement model discrete equations.

Appendix C provides the linearized matrices used in the extended Kalman filter and smoother.

SENSOR ERRORS

This section examines noise sources in the rate gyroscopes and GPS outputs using Allan deviation, and describes the approach used to tune the noise estimate for the Kalman filter.

Allan Variance

Allan variance was originally developed to characterize the frequency instability in precision oscillators.[113] The formulas presented here use notation adapted from subsequent applications of Allan variance to sensors from inertial navigation systems, such as fiber-optic gyroscopes.[114–116] Allan variance is calculated by comparing adjacent cluster averages. As shown in figure 154, a cluster average is calculated by averaging a set of consecutive sampled values.

$$\bar{\Omega}_k(n\Delta t) = \frac{1}{n} \sum_{j=k}^{k+n-1} \Omega_j$$

Figure 154. Equation. Cluster average.

The corresponding cluster time is $n\Delta t$, where n is the number of samples in the cluster and Δt is the time interval between samples. For a signal with N samples, the overlapping Allan variance is defined for a given cluster time as shown in figure 155.

$$\sigma_A^2(n\Delta t) = \frac{1}{2(N-2n+1)} \sum_{k=1}^{N-2n+1} (\bar{\Omega}_{k+n} - \bar{\Omega}_k)^2$$

Figure 155. Equation. Allan variance from cluster averages.

The term "overlapping" applies here to signify that each time the index, k, increments forward, the two new clusters overlap the clusters used in the previous step by n–1 samples. Typically, this formula is applied for many possible values of cluster time and displayed in a plot as Allan deviation (σ_A) versus cluster time. El-Sheimy et al. describe Allan variance as a representation of "the RMS random-drift errors as a function of averaging times."[116]

Computational effort is greatly reduced by preprocessing the signal using simple (rectangular) integration and substituting differences from the integrated signal for the cluster averages, as shown in figure 156 and figure 157.

$$\theta_k = \Delta t \sum_{j=1}^{k} \Omega_j$$

Figure 156. Equation. Rectangular integration.

$$\sigma_A^2(n\Delta t) = \frac{1}{2(N-2n+1)} \frac{1}{(n\Delta t)^2} \sum_{k=1}^{N-2n+1} (\theta_{k+2n-1} - 2\theta_{k+n-1} + \theta_{k-1})^2$$

Figure 157. Equation. Allan variance from the integrated signal.

Rate Gyroscopes

Three tests were performed with a rate gyroscope still (in the Earth-fixed frame) to characterize its noise and bias using Allan deviation. In two of the tests, the sensitive axis was parallel to a circle of latitude (i.e., pointing east-west). As such, the sensor was subjected to a zero rate input. In the third, the axis was aligned with a meridian (i.e., pointing north-south), and could detect the rotation of the Earth. Each test proceeded for at least 17.5 hours, and data were obtained at 100 Hz. Figure 158 shows the Allan deviation for a zero-input test performed over 21.5 hours.
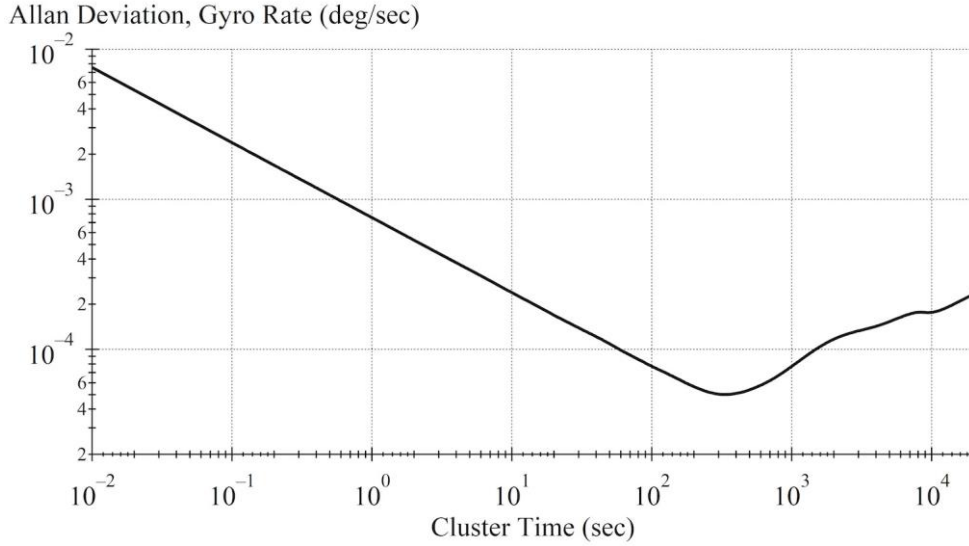
Figure 158. Graph. Allan deviation, rate gyroscope.

IEEE Std 952 recommends the use of an empirical curve fit to measured Allan variance to determine the coefficients associated with each class of noise in fiber-optic gyroscopes.[114] The standard form of the fitting function is as shown in figure 159.

$$\sigma_A^2(n\Delta t) = \frac{R_A^2(n\Delta t)^2}{2} + \frac{K_A^2 n\Delta t}{3} + \frac{2B_A^2 \ln(2)}{\pi} + \frac{N_A^2}{n\Delta t} + \frac{3Q_A^2}{(n\Delta t)^2}$$

Figure 159. Equation. Allan variance fitting function.

The terms to right of the equal sign correspond to ramp instability (R_A), rate random walk (K_A), bias instability (B_A), angle random walk (N_A), and quantization (Q_A).

For the rate gyroscope examined in figure 158, angle random walk dominates the signal for cluster times less than or equal to 100 seconds. This manifests as a slope of –1/2, due to the logarithmic scaling. Angle random walk is estimated using the value of Allan deviation for a 1-second cluster time, which is 7.56×10^{-4} deg/s. This implies the coefficient for angle random walk shown in figure 160. Often, angle random walk is specified in alternate units, as shown.

$$N_A = 7.56\text{x}10^{-4}\ \deg/\sqrt{s} = 0.0454\ \deg/\sqrt{h}$$

Figure 160. Equation. Angle random walk value.

None of the other idealized mechanisms described in IEEE Std 952 fit the data for cluster times above 100 seconds very closely. However, addition of rate random walk and ramp instability improves the curve fit for cluster times between 100 seconds and ½ hour. Figure 161 lists the coefficient values.

$$R_A = 1.03\text{x}10^{-7}\,\deg/s^2,\ K_A = 1.38\text{x}10^{-6}\,\deg/s^{3/2}$$

Figure 161. Equations. Rate random walk and ramp instability coefficients.

The actual spectral content of the rotation rate signals approximated the idealized (one-sided) spectral density function, S_Ω, expected using the three noise parameters derived in the Allan variance analysis, as shown in figure 162.

$$S_\Omega(2\pi f) = \frac{R_A^2}{(2\pi f)^3} + \frac{K_A^2}{(2\pi f)^2} + N_A^2$$

Figure 162. Equation. Idealized spectral content from Allan variance.

The actual spectral content is flat, and approximates white noise rotation rate, for frequencies above 0.002 Hz. As frequency decreases below 0.002 Hz, the spectral density increases. For frequencies below 0.0005 Hz, the contributions of rate random walk and ramp instability effects outpace angle random walk.

Other relevant observations from the three trials include:

- For the test examined in figure 158, the standard deviation with the bias removed was 0.00752 deg/s. This is the value of the Allan deviation for a cluster time of 0.01 sec (i.e., using 1-point clusters).

- Auto correlation using 20,000 sampled data points did not produce a value above 0.5 percent of the signal variance for a non-zero lag. This implies that the signal is dominated by white noise at high frequencies.

- Normalized probability distributions produced values of skew below $2\mathrm{x}10^{-3}$ and excess Kurtosis below $2.6\mathrm{x}10^{-2}$.

- Normalized probability distributions produced Kolmogorov-Smirnov test for normality produces scores of 0.00504–0.00546. The high number of samples ($> 6,400,000$) implies confidence that the distribution is not normal, yet a similar level of confidence that the cumulative distribution differs from normality by less than 0.0055.

GPS Outputs

Figure 163 shows the Allan deviation for GPS height collected over 3.0 hours. These data included RTK corrections, and carrier phase ambiguities resolved to "narrow-lane integers." The empirical function in figure 159 produces a reasonable fit to the data for cluster times less than 10 seconds, but not the rest. Inspection of the autocorrelation function reveals the presence of several distinct noise sources with specific time constants and characteristic frequencies. (See figure 164.) The same is true of GPS pitch inclination and GPS roll inclination.
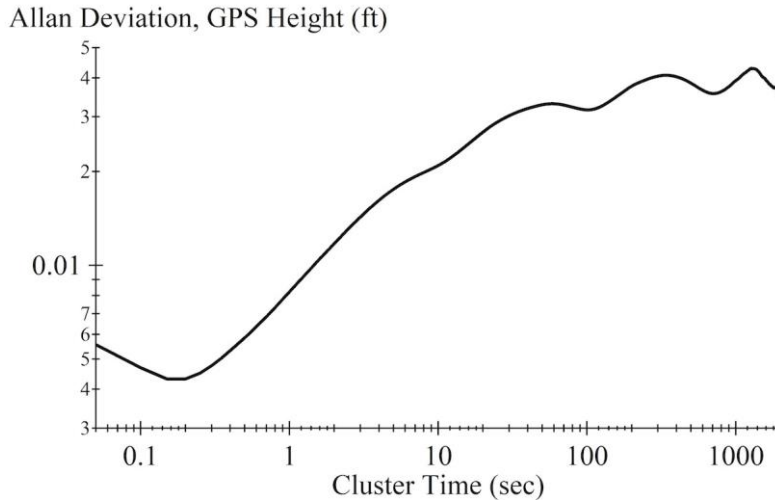
Figure 163. Graph. Allan deviation, GPS height.
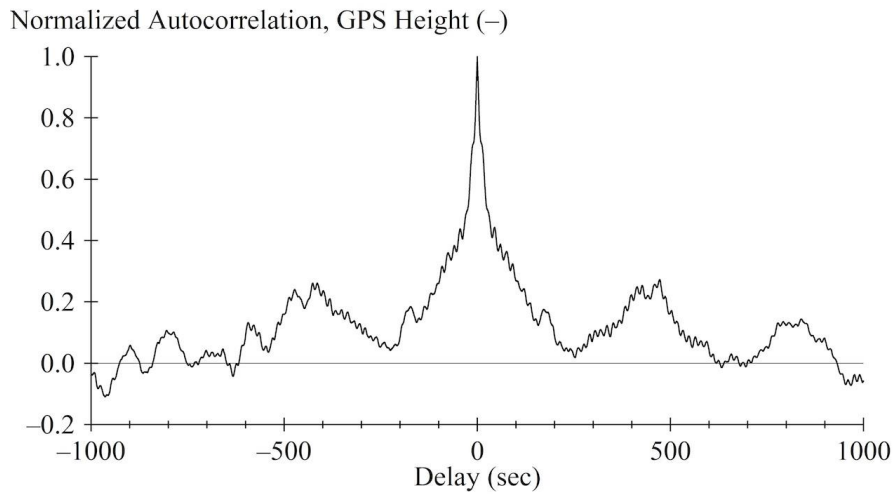
Figure 164. Graph. GPS height, normalized autocorrelation.

It is likely that tightly coupled integration with the GPS system would be required to capture the noise sources evident in the Allan deviation and autocorrelation functions. For simplicity, the measurement model for all of the GPS outputs only includes normally distributed random noise. These are quantified using estimates of standard deviation.

Tuning

Table 22 summarizes the approach used to tune the Kalman filter. The table lists each error quantity, the associated symbol for standard deviation, the corresponding model (measurement or process), and the value. The table also identifies which values were established before tuning and fixed, and which values were tuned based on the outcome of preliminary test runs.

Table 22. Kalman filter tuning approach.

Error Estimate	Symbol	Model	Status	Value
GPS height	σ_{pz}	Measurement	Fixed	0.47 inches
GPS vertical velocity	σ_{vz}	Measurement	Fixed	0.098 ft/s
GPS pitch inclination	σ_{θ}	Measurement	Fixed	0.12 deg
GPS Roll inclination	σ_{ϕ}	Measurement	Fixed	0.2 deg
Acceleration	σ_a	Process	Tuned	6×10^{-4} g
Acc. random walk	$\sigma_{a'}$	Process	Tuned	1.64×10^{-9} ft/s^3
Roll rate	σ_{ω_1}	Process	Fixed	7.7×10^{-3} deg/s
Roll rate random walk	$\sigma_{\omega_1'}$	Process	Tuned	4.2×10^{-6} deg/s^2
Pitch rate	σ_{ω_2}	Process	Fixed	7.7×10^{-3} deg/s
Pitch rate random walk	$\sigma_{\omega_2'}$	Process	Tuned	2.2×10^{-4} deg/s^2
Yaw rate	σ_{ω_3}	Process	Fixed	0 deg/s

Of the 11 estimates of standard deviation, only four were designated for tuning. Preliminary analysis revealed that tuning the full set of values improved the results. However, it required a very complicated optimization process that was not guided by insight into the system kinematics or knowledge of signal processing. Further, the reported performance of the system would have been difficult to reproduce in a practical application.

Fixed quantities were set using information that could be easily obtained, as follows:

GPS height, GPS roll inclination, and GPS pitch inclination: The GPS provided a real-time estimate of standard deviation with each observation of height, roll, and pitch. Table 22 lists the median values of those estimates observed during preliminary runs, excluding bounce tests and quiescent tests. Use of the individual estimates in real time may lead to some improvement, but was not found to be necessary. Note that the performance reported in this chapter is not maintained if the carrier phase ambiguities are not resolved to "narrow-lane integers," except in the constant height and attitude reference implementation.

GPS vertical velocity: The manual for the GPS hardware and firmware reported "velocity accuracy" to less than 0.098 ft/s.

Pitch and roll rate: Standard deviation values for pitch rate and roll rate are fixed at 0.0077 deg/s. This is the average value from the three laboratory tests used to examine Allan deviation. This value can be obtained by monitoring the output of each sensor over several minutes of zero-input operation.

Yaw rate: Since the influence of yaw rate on system performance for the test runs used in this demonstration is small, a value of zero is used for it standard deviation. Using a value of zero for yaw rate changes the results very little. However, this may not be the case for a testing program that includes operation on a curve.

Tuning of the remaining four quantities using profiles from the left- and right-side using at least six test runs is recommended: (1) constant speed of 5 mi/hr or less, (2) constant speed of 45 mi/hr or greater, (3) braking at 0.15–0.2 g, (4) braking at 0.3 g or greater, (5) a stop no more

than 2 seconds long preceded by braking at 0.3 g or greater, and (6) a stop no less than 5 seconds long preceded by braking at 0.2 g or less. In the braking runs, the final speed should be at least 15 mi/hr. In the runs with stops, the speed before braking begins should be greater than 25 mi/hr.

In this research, the tuning procedure optimized the same quantities in the preliminary runs that are used here to report the performance of the system in the regular test runs. This includes: (1) maximizing cross correlation for all preliminary runs, (2) maximizing agreement in average IRI for preliminary runs at constant speed, and (3) maximizing agreement in peak IRI at the critical location for all runs with braking and stops. The "critical location" is either the location of a stop, or the location where the brakes were released for runs with braking but no stop. Visual inspection of short-interval roughness profiles, PSD plots, and filtered profile plots is recommended.

Although a tuning process based on blind optimization would have succeeded, some preliminary constraints on the process were applied:

1. Set the values for pitch rate random walk and roll rate random walk at the level derived from the Allan variance analysis described above. If the required test data are not available, use values of zero.

2. Define a space of error estimates for acceleration and acceleration random walk that perform as well or better than the nominal profiler for the constant (high) speed run (i.e., do no harm) and the run with light braking. In this case, the "nominal profiler" means profile derived with this system using only the body-fixed component of vertical acceleration, the height sensor, and the distance encoder.

3. Using the lowest values found in step 2, define the range of values for pitch rate random walk that maximizes performance for the run with heavy braking and improves performance for the runs with stops. Prioritize the left side profile. Deprioritize values of pitch rate random walk that degrade performance for the runs examined in step 2.

4. Using the lowest values found in steps 2 and 3, define the range of values for roll rate random walk that maximizes the performance for the run at low speed and the run with heavy braking. Prioritize the right side profile. Deprioritize values of roll rate random walk that degrade performance on the other runs.

5. Repeat steps 2 through 4 until no incremental performance improvement is observed. Each time step 2 is re-applied, fix pitch rate random walk and roll rate random walk at the lowest values found in the previous iteration.

6. Fix the acceleration error estimate. Find the combination of the three random walk error estimates that provide the best collective performance for all preliminary runs. This will often require a trade-off between maintaining performance at constant speed and improving performance with braking.

Blind optimization beginning with results from the steps above may further improve performance. However, if performance improvements depend on adjustment of the error estimates to a precision level lower than several percent, it is less likely the same level of

performance will exist in all conditions. With the tuning approach described here, the overall performance of each Kalman filtering and smoothing implementation presented in this chapter is maintained for changes in each standard deviation value in table 22 of up to 40 percent. (The variations were tested using scale factors with a constant step on a logarithmic scale of ½ octave.) That is, the performance does not depend on precise tuning.

The overall objective of the tuning is to determine the frequency range where the inertial sensors (i.e., the process model) dominate the content within the kinematic state variables, the frequency range where the GPS observations dominate, and the frequency range where their influence is of the same order of magnitude. Note that the three random walk values represent the collective influence of several factors, including slowly varying sensor bias, omissions in the process model, numerical imprecision, and imprecise sensor mounting.

IMPLEMENTATION FOR PROFILE CALCULATION

Figure 165 summarizes the flow of sensor outputs used to calculate profile with the Kalman smoother. Inertial sensors (accelerometers and rate gyroscopes) drive the process model within the Kalman filter, and GPS sensors provide inputs to the measurement model. The Kalman filter passes estimates of the system state and state error covariance to the Kalman smoother. The system state variables include floating reference height. The Kalman smoother produces refined estimates of the system state and updated estimates of covariance based on stored readings from the inertial sensors and stored Kalman filter outputs. The smoother requires stored signals because it steps backward in time through them to make the calculations.
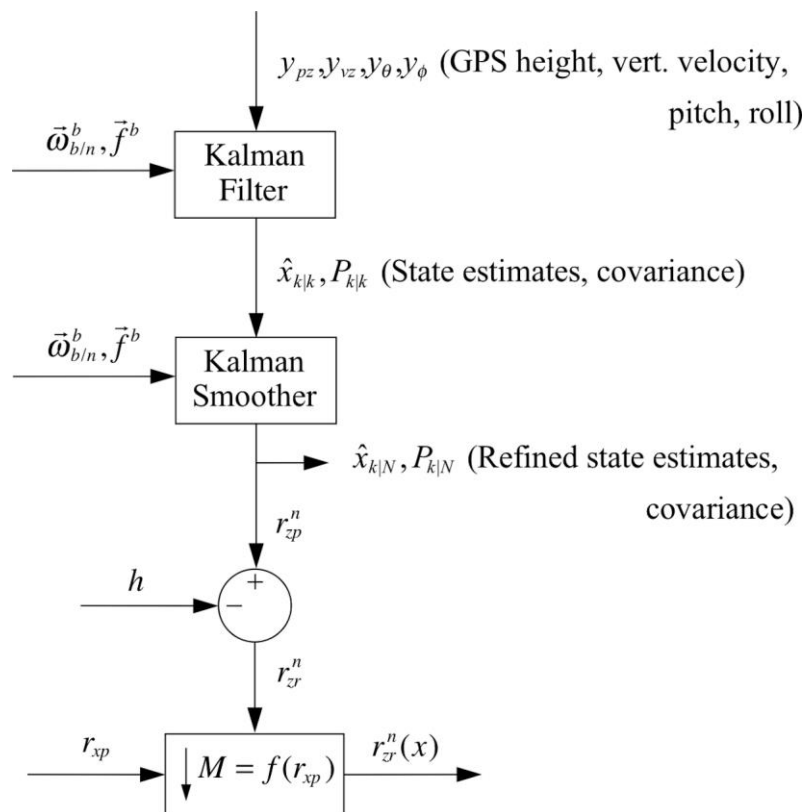
Figure 165. Block diagram. Sensor signal flow for profile computation.

Profile elevation ($r_{zr,k}^n$) at each time step (k) is calculated as shown in figure 166.

$$r_{zr,k}^n = r_{zp,k}^n - h_k$$

Figure 166. Equation. Profile elevation calculation using Kalman smoother.

In figure 166, $r_{zp,k}^n$ is the floating reference height produced by the Kalman smoother, and h_k is the height-sensor reading. The temporal profile (i.e., road elevation versus time), $r_{zr,k}^n$, is decimated to obtain spatial profile, $r_{zr}^n(x_k)$, as a function of distance at a constant interval of 0.2 inches. The decimation factor, M, varies with host-vehicle speed and depends on longitudinal travel distance, r_{xp}. An optical distance encoder measures longitudinal distance.

This system uses a constant time step of 1/16,000 seconds because analog data from the height sensors, vertical accelerometers, and longitudinal accelerometers were digitized at 16,000 Hz. However, the rate gyroscopes and the lateral accelerometer update their readings at 100 Hz, and the height sensors provide readings at a rate near 3,240 Hz. At each time step, the calculations use the most recent reading from each sensor.

The GPS provides updates at a rate of 20 Hz. As such, the Kalman filter only applies a measurement update at time steps when a new GPS observation is available. The Kalman smoother performs all of its calculations at 16,000 Hz because it depends on estimates of the state and state error covariance calculated at 16,000 Hz in the forward-running Kalman filter.

Independent Kalman filters and smoothers are applied for each of the left and right profiles. The measurement system included accelerometers (vertical and longitudinal) and height sensors on both sides of the vehicle. Profiles from each side depend on readings from the same rate gyroscopes, lateral accelerometer, optical distance encoder, and GPS. This chapter presents results for the left profile.

RESULTS

Use of the additional sensors with Kalman smoothing improved profile measurement accuracy at low speed, during braking, and at stops considerably. Three mechanisms contributed to the improvement.

First, three-dimensional measurement of acceleration and rotation rate provided a more accurate measurement of profiler vertical motion. Resolution of acceleration into the direction aligned with gravity reduced the artificial vertical curvature that appeared in the floating-reference-height signal during braking, particularly in locations where the brakes were released. However, it did not reduce the bias in the integrated accelerometer signal (v_{zp}) in the range leading to and during a stop sufficiently to avoid large levels of artificial localized roughness.

Second, use of a Kalman filter to incorporate GPS measurements of height and velocity arrested drift in the floating-reference-height signal. Similarly, incorporation of GPS measurements of pitch and roll inclination arrested drift in the estimates of pitch and roll orientation. The independent measurements by the GPS were necessary because of slowly varying bias in the inertial sensors.

Third, the use of a Kalman smoother provided necessary additional reduction in drift of the floating-reference-height signal. Use of past and future measurements to refine estimates of the system states reduced erroneous low-frequency responses to disturbances that appeared as drift. The backward pass by the Kalman smoother allowed absolute measurements by the GPS sensors to better influence the estimates of low-frequency system response, and confined the influence of the inertial sensors to the high-frequency range.

Results are provided below using: (1) three-dimensional measurement of kinematics by inertial sensors with incorporation of the GPS using Kalman filtering, and (2) additional refinement of state estimates from the Kalman filter using a Kalman smoother. Results are also provided for three additional implementations of the Kalman smoother:

1. Height-sensor reflection: When the host-vehicle speed is less than 0.1 mi/hr, this procedure uses the height-sensor signal as an independent measurement of floating reference height in place of GPS measurements. This is based on the assumption that the road surface elevation at a point is constant, and that equal and opposite fluctuations should appear in the floating-reference-height signal and the height-sensor signal.

2. Constant attitude reference: This implementation of the Kalman smoother replaces GPS measurement of pitch and roll inclination with a constant estimate of zero. This is intended to demonstrate the potential performance of the system if GPS-based attitude measurement is not present or is experiencing an outage.

3. Constant height and attitude reference: This implementation of the Kalman smoother replaces all GPS measurements with a constant estimate of zero. This is intended to demonstrate the potential performance of the system during a GPS outage. In this mode of operation, no actual measurements are provided to the Kalman smoother. Rather, the "constant reference" signals (and the associated elements of the measurement noise covariance matrix) place a limit on the absolute level of position and orientation drift, and the Kalman smoother functions as a high-pass filter.

Kalman Filter

Table 23 provides roughness and cross correlation results for profiles processed using the Kalman filter without the smoother. Peak roughness is the highest value in the short-interval roughness profile in the range from 600 ft to 750 ft from the test section start. This is the area where the host vehicle came to a stop in the stop-and-go runs or released the brakes in the braking runs without a stop. In the reference profile, the peak roughness is 152 inches/mi. The percentage error in average roughness for the 0.1-mile-long test section is provided. When a large error in peak roughness occurs, it accounts for most of the error in average roughness. Cross correlation values provide a rating of agreement to the reference profile in the waveband of interest for the IRI on a scale from –1 to 1. High cross correlation ensures that the details of the profile, as well as the overall roughness and spatial distribution of roughness, agree with the reference profile. Cross correlation of 0.92 or above is required for adequate profile agreement per AASHTO R56-14, and 0.98 is required to demonstrate reference-grade performance.[87]

113

Table 23. Results for the Kalman filter.

Run Designation	Peak Roughness (inches/mi)	Average Roughness Error (Percent)	Cross Correlation
S&G, 1.1-sec stop, 0.17 g	292	7.8	0.629
S&G, 1.1-sec stop, 0.20 g	208	3.0	0.840
S&G, 2.1-sec stop, 0.33 g	817	40.3	< 0.2
S&G, 5.8-sec stop, 0.17 g	1,379	73.0	< 0.2
S&G, 5.7-sec stop, 0.20 g	1,086	52.4	< 0.2
S&G, 5.8-sec stop, 0.20 g	994	50.6	< 0.2
S&G, 10.7-sec stop, 0.20 g	1,744	90.7	< 0.2
NS, 45–7 mi/hr, 0.20 g	174	5.5	**0.921**
Brk, 44–19 mi/hr, 0.19 g	174	8.2	0.915
Brk, 45–18 mi/hr, 0.39 g	162	4.3	**0.930**
Brk, 31–14 mi/hr, 0.16 g	163	3.7	0.915
Brk, 31–14 mi/hr, 0.18 g	151	1.8	**0.944**
Brk, 31–14 mi/hr, 0.18 g	204	7.2	0.904
Brk, 31–12 mi/hr, 0.25 g	218	6.6	0.882
Brk, 30–21 mi/hr, 0.84 g	160	6.6	0.914
10 mi/hr	150	1.5	**0.986**
3 mi/hr	152	2.7	0.855

Reference peak roughness value: 152 inches/mi. Adequate cross correlation (> 0.92) is shown in bold.

For the test runs with braking but no stop, the Kalman filter offered some improvement in road profile measurement over the basic temporal algorithm examined in Chapter 5. However, the adaptive high-pass filtering algorithm offered better performance and did not require additional sensors beyond the nominal inertial profiler design. The Kalman filter failed to produce adequate cross correlation in five of the braking runs.

Without the smoother, the Kalman filter produced large errors peak roughness and commensurately low cross correlation. This is because the Kalman filter did not suppress drift sufficiently to eliminate artificial roughness caused by drift in the floating-reference-height signal at locations where the host vehicle stops. Figure 167 provides an example for the test run with a 10.7-second-long stop. The figure compares the floating-reference-height signal produced by the Kalman filter to the GPS height observations provided to the filter as measurements. During the stop (from 15.7 to 26.4 seconds), the net change in height measured by the GPS was 0.69 inches downward. The height sensor measured a similar decrease in distance between the profiler and the road surface of 0.72 inches during this time increment.
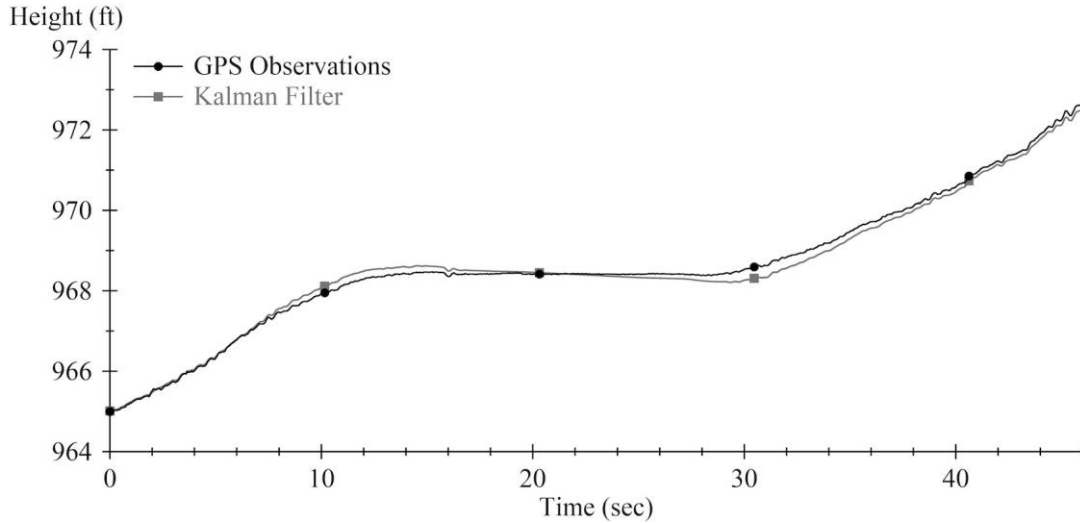
Figure 167. Graph. Drift in Kalman filter output, 10.7-second-long stop.

Braking, which began at 5.3 seconds in this test run, caused the floating-reference-height signal to drift. During the stop, the net downward change in floating reference height is 3.7 inches. The portion of this change that was not compensated by the height sensor appears in the profile as a step change in elevation at the location of the stop. The combined effects of drift at the stop and in the low-speed range near the stop caused an artificial peak in the short-interval roughness profile of 1744 inches/mi.

After the onset of drift the Kalman filter enforced abrupt corrections to the floating-reference-height signal each time it obtained a new observation from the GPS. Figure 168 provides an example using a close-up view of a portion of the traces in figure 167. In this region, the floating reference height has drifted 0.2 ft above the prevailing GPS readings. Between GPS observations, the inertial sensors and the process dynamics solely determine the progression of floating reference height. Each 0.05 seconds a GPS observation is available, and the Kalman filter imposes a correction to the floating-reference-height signal that appears as a step change. For the range shown in figure 168, these are downward step changes of approximately 0.08 ft. These step changes appear in the final profile as artificial roughness.
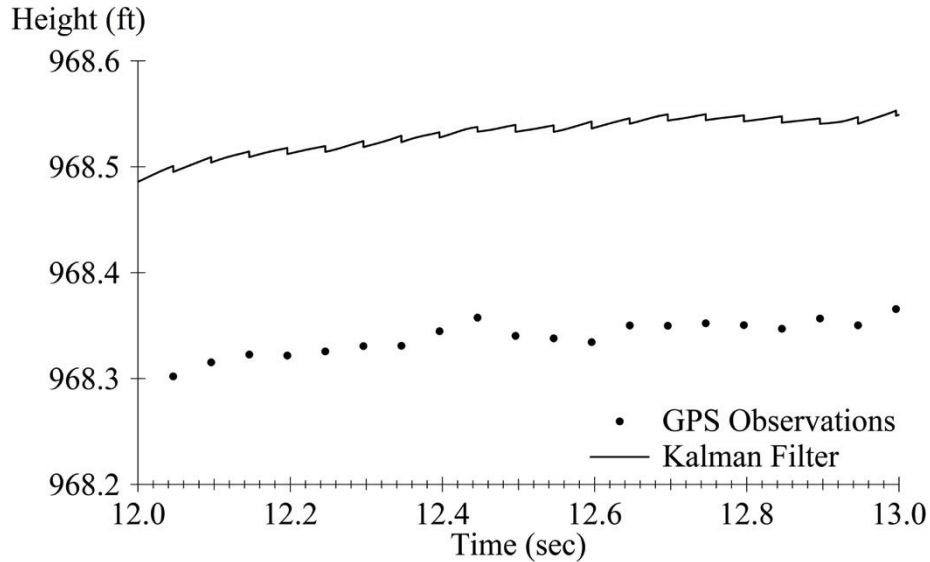
Figure 168. Graph. Kalman filter corrections during drift, 10.7-second-long stop.

Drift of the floating-reference-height signal relative to the GPS observations is attributed to the recursive nature of the Kalman filter and resulting delay in its low-frequency response. Reduction in the process noise covariance estimate associated with acceleration random walk (i.e., a reduction in the ratio of $\sigma_{a'}^2$ to sigma σ_{rz}^2) reduces this drift. However, it raises the relative influence of GPS height readings on the content of the state estimates, such as the floating-reference-height signal. This causes noise in the GPS height readings to contaminate the profile in the wavelength range of interest, particularly in areas that do not include braking and in test runs performed at constant speed.

Since the Kalman filter did not produce results as good as the best temporal or spatial error suppression algorithms described in Chapter 5, sensor augmentation with the Kalman filter (and no smoother) is not expected to provide a return on the additional sensor cost.

Kalman Smoother

Relative to Kalman filtering alone, the smoother provided additional suppression of drift in the floating-reference-height signal. For example, figure 169 compares the floating-reference-height signal produced by the Kalman smoother to the GPS height measurements for the test run with a 10.7-second-long stop. Much less drift appears relative to the output of the Kalman filter, and the artificial downward change in elevation in the profile is reduced from 2.8 inches to less than 0.1 inches.
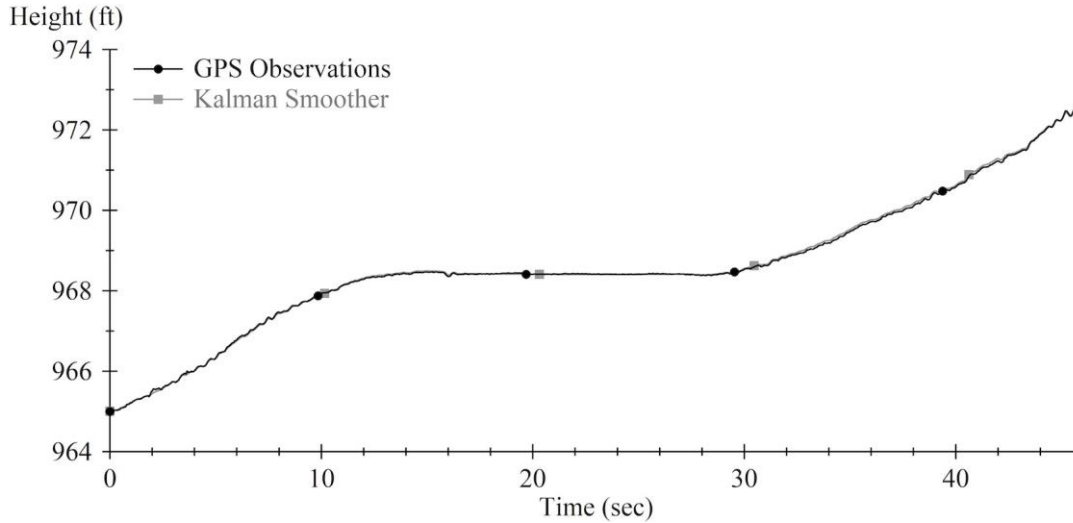
Figure 169. Graph. Drift in Kalman smoother output, 10.7-second-long stop.

Table 24 provides roughness and cross correlation results for profiles processed using the Kalman smoother. All braking test runs without a stop correlated to the reference pass with a score above the AASHTO requirement of 0.92, and many were at the "reference quality" level of 0.98.[87] Further, the error in average roughness was less than 5 percent and the upward bias in peak roughness was less than 10 percent relative to the reference pass in eight of the nine test runs. Much of the variation in peak roughness among these runs is attributed to variations in lateral tracking.

Table 24. Results for the Kalman smoother.

Run Designation	Peak Roughness (inches/mi)	Average Roughness Error (Percent)	Cross Correlation
S&G, 1.1-sec stop, 0.17 g	218	2.6	0.886
S&G, 1.1-sec stop, 0.20 g	187	0.1	**0.957**
S&G, 2.1-sec stop, 0.33 g	170	3.0	**0.963**
S&G, 5.8-sec stop, 0.17 g	189	6.2	**0.925**
S&G, 5.7-sec stop, 0.20 g	184	0.9	0.904
S&G, 5.8-sec stop, 0.20 g	149	3.0	**0.954**
S&G, 10.7-sec stop, 0.20 g	161	2.9	**0.938**
NS, 45–7 mi/hr, 0.20 g	155	2.1	**0.977**
Brk, 44–19 mi/hr, 0.19 g	155	1.7	**0.978**
Brk, 45–18 mi/hr, 0.39 g	144	−0.8	**0.975**
Brk, 31–14 mi/hr, 0.16 g	143	−0.8	**0.963**
Brk, 31–14 mi/hr, 0.18 g	145	−0.9	**0.978**
Brk, 31–14 mi/hr, 0.18 g	174	0.9	**0.981**
Brk, 31–12 mi/hr, 0.25 g	159	1.2	**0.985**
Brk, 30–21 mi/hr, 0.84 g	165	3.9	**0.942**
10 mi/hr	147	−0.6	**0.988**
3 mi/hr	151	−1.8	**0.973**

Reference peak roughness value: 152 inches/mi. Adequate cross correlation (> 0.92) is shown in bold.

Five of the seven runs with a stop produced cross correlation values above the AASHTO requirement. The largest upward bias in peak roughness compared to the reference value was 66 inches/mi. The reduction in peak roughness errors for runs with a stop demonstrates the additional removal of drift in the floating-reference-height signal offered by adding the Kalman smoother.

The run with braking from 44 mi/hr to 19 mi/hr at 0.19 g offers a good illustration of the quality in profile and roughness measurement at the cross correlation threshold levels. Figure 170 compares the short-interval roughness profiles for the reference pass to the run with braking processed using the Kalman filter only. Comparison of the two profiles produced a cross correlation level of 0.915. (See table 23.) This is near the threshold for adequate agreement. The average roughness agrees to within 8.2 percent, and many of the details of the distribution of roughness throughout the section are similar, as shown in figure 170.
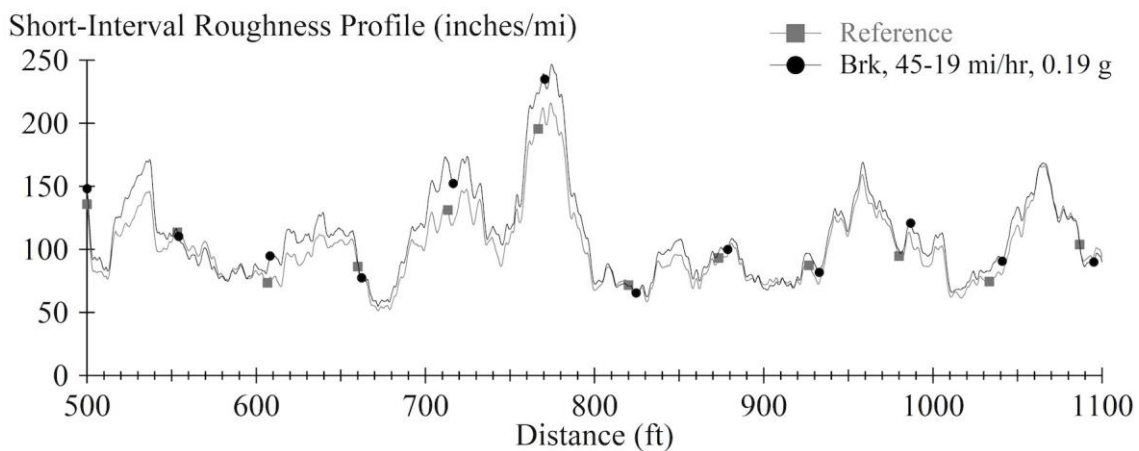
Figure 170. Short-interval roughness profile comparison, Kalman filter.

Figure 171 compares the short-interval roughness profiles for the reference pass to the run with braking processed using the Kalman smoother. Comparison of the two underlying profiles produced a cross correlation level of 0.975. (See table 24.) This is near the threshold for "reference level" agreement. In this case, the average roughness in the run with braking was within 2 percent of the average roughness in the reference pass. In addition, the details of the two short-interval roughness profiles are very similar throughout the section. (The reference trace is not visible behind the trace from the run with braking in many areas.) A high cross correlation value is only possible if agreement exists in the overall roughness, the spatial distribution of roughness, and the shape of the underlying features in the profile.
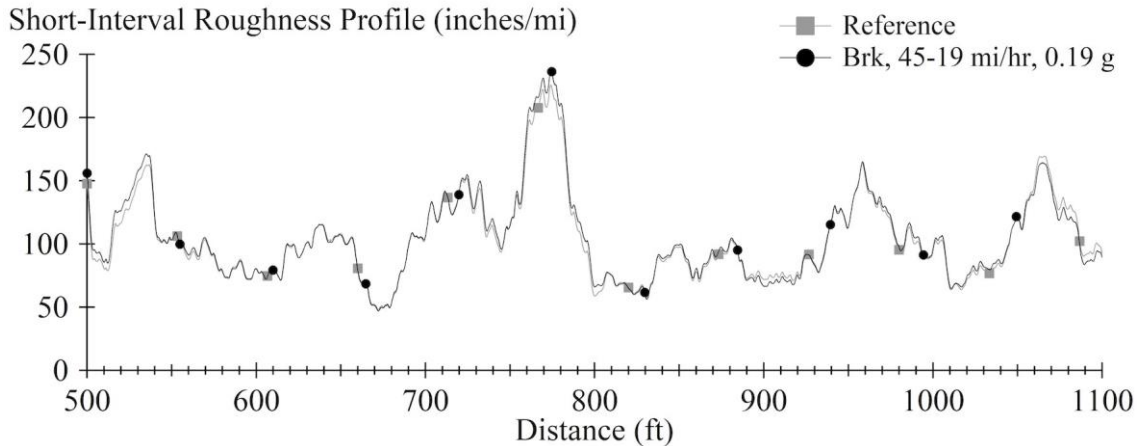
Figure 171. Short-interval roughness profile comparison, Kalman smoother.

The Kalman smoother also improved measurement of profile at low speed. As described in Chapter 5, high-pass filtering of the accelerometer signal eliminated numerical integration errors for the test run at 3 mi/hr. Application of the filters produced cross correlation to the reference pass of 0.938. The Kalman smoother offered a much greater improvement in measurement quality for this test run, due to elimination of errors associated with accelerometer alignment. As speed decreases, sensor alignment errors caused by pitch and roll dynamics of the host-vehicle sprung mass correspond to progressively shorter wavelengths. In turn, the resulting measurement error has a progressively larger effect on content within the profile that affects the IRI. The motion is exacerbated at very low speed by difficulties maintaining a consistent throttle command. Resolution of acceleration into a consistent vertical direction reduced alignment errors, and produced a cross correlation value of 0.973.

The additional sensors and Kalman smoothing algorithm proposed in this research removed most of the measurement error that was present when the test runs are processed using only elements of the basic inertial profiler design (i.e., the nominal sensor set and the basic temporal profile calculation algorithm). In addition, the system proposed here improved reproduction of the reference profile significantly over the best error suppression algorithms described in Chapter 5, which use only the nominal sensor set that appears in a typical commercial profiler. However, this system did not achieve adequate performance for all of the runs with a stop. The remaining error is caused primarily by drift in the GPS height signal that occurs while the profiler is stopped, which is introduced into the floating-reference-height signal during the measurement update in the Kalman filter. The following section describes a specialized provision that is proposed for mitigating this error source.

Kalman Smoother with Height-Sensor Reflection

Height-sensor reflection offers further reduction of profile measurement error at stops. This procedure switches to an alternate mode of operation when the host-vehicle speed is less than 0.10 mi/hr. In the "stopped" mode, the Kalman filter replaces the GPS with the height sensor as an external source of position information. This is based on the assumption that at very low speed the road surface elevation is constant and changes to the height-sensor signal are caused solely by vertical motion of the profiler reference point. This is not universally true when speed

is below 0.10 mi/hr. However, GPS readings of height are prone to drift over time intervals of several seconds or more. (See figure 163.) This is not included in the measurement error model. As such, the height sensor is considered a more accurate measure of profiler reference point movement during a stop. Height-sensor reflection is implemented using the four provisions described here.

The first provision replaces fluctuations in GPS measurements with fluctuations in height-sensor measurements in the very low speed range, as shown in figure 172.

$$y_{rz,k} = y_{rz,ref} + (y_{h,ref} - y_{h,k})$$

Figure 172. Equation. Height measurement in "stopped" mode.

In figure 172, $y_{h,k}$ is the height-sensor reading at each time step. The quantities $y_{rz,ref}$ and $y_{h,ref}$ are the last values of GPS height and height-sensor output, respectively, obtained before initiation of the stopped mode. These remain constant throughout the very low speed interval, and are included in the calculation to offset the fluctuating height-sensor signal to a level consistent with the prevailing GPS height. This changes the measurement equation for height to the expression in figure 173. In figure 173, the error term, $e_{h,k}$, represents noise in the height sensor.

$$y_{h,k} = r_{zp,k}^{n} + c_{\theta_k}(s_{\phi_k}l_y + c_{\phi_k}l_z) + y_{rz,ref} + y_{h,ref} + e_{h,k}$$

Figure 173. Equation. Height measurement model in "stopped" mode.

The second provision replaces σ_{rz}^2 with σ_h^2 in the measurement covariance matrix to account for the modified source of measurement noise, where $\sigma_h = 0.06$ inches. This value is higher than the prevailing noise level in the height sensor. Tuning of σ_h using preliminary test runs with stops was required, and the final value depended on profiler host-vehicle pitch dynamics as it approached the stop.

The third provision removes the influence of the other GPS observations. The measurements provided to the Kalman filter are replaced as shown in figure 174.

$$y_{vz,k} = y_{vz,ref}$$
$$y_{\theta,k} = 0$$
$$y_{\phi,k} = 0$$

Figure 174. Equation. Measurement model components in "stopped" mode.

In figure 174, $y_{vz,ref}$ is the last observation of GPS vertical velocity obtained before initiation of the quasi-stopped mode. Values of zero are maintained for pitch and roll inclination. Estimates of standard deviation for GPS vertical velocity and pitch inclination angle are increased by a factor of 10. This removes their influence on the state estimates throughout the stop. No factor is applied to the standard deviation for the measurement of roll inclination, because excessive drift in roll inclination introduced drift into the measurement equation for high of the profiler reference height for the right-side profiler.

The fourth provision accommodates the sampling rate of the height sensor. In this implementation, the process dynamics are updated at a rate of 16,000 Hz, whereas the height sensor provides measurements at a rate near 3,240 Hz. As such, the Kalman filter applies the measurement update when a new reading from the height sensor is available. No change to the format of the Kalman smoother is required.

Table 25 lists the roughness and cross correlation results for test runs with stops using the Kalman smoother with height-sensor reflection. All seven test runs produced cross correlation values above the AASHTO requirement and above the cross correlation produced by the Kalman smoother without height-sensor reflection. In some cases, peak roughness values were lower than the reference value. This is due in part to variations in lateral tracking of the profiler, and in part to the exclusion of actual roughness from the measurement in the area where height-sensor reflection was applied. The average roughness was within 5 percent of the reference values in all runs.

Table 25. Results for the Kalman smoother with height-sensor reflection.

Run Designation	Peak Roughness (inches/mi)	Average Roughness Error (Percent)	Cross Correlation
S&G, 1.1-sec stop, 0.17 g	134	−1.8	**0.969**
S&G, 1.1-sec stop, 0.20 g	138	−2.3	**0.963**
S&G, 2.1-sec stop, 0.33 g	154	1.9	**0.972**
S&G, 5.8-sec stop, 0.17 g	160	4.4	**0.949**
S&G, 5.7-sec stop, 0.20 g	138	−1.5	**0.952**
S&G, 5.8-sec stop, 0.20 g	141	2.3	**0.967**
S&G, 10.7-sec stop, 0.20 g	168	3.0	**0.958**

Reference peak roughness value: 152 inches/mi. Adequate cross correlation (> 0.92) is shown in bold.

Kalman Smoother with a Constant Attitude Reference

This implementation of the Kalman smoother demonstrates the potential performance of the system if GPS-based attitude measurement is not present or is experiencing an outage. GPS measurement of pitch and roll inclination are replaced with constant estimates of zero, as shown in figure 175.

$$y_{\theta,k} = 0, y_{\phi,k} = 0$$

Figure 175. Equation. Constant attitude measurement.

GPS measurements of height and velocity remain intact, and the Kalman filter applies the measurement update at 20 Hz using actual height and velocity measurements together with the artificial attitude measurements. The net effect of imposing a constant reference signal on pitch and roll rotation is removal of their low-frequency content. That is, the constant attitude reference functions within the Kalman filter as a high-pass filter on integrated outputs from the rate gyroscopes.

The specific outcome of using the constant attitude reference depends on estimates of standard deviation provided to the measurement covariance matrix. Figure 176 provides the estimates. Further, the performance of this implementation for test runs with a stop depended on application

of height-sensor reflection previsions described above. During the stopped mode, the error estimate for height measurement is increased as shown in figure 177.

$$\sigma_\theta = 5 \text{ deg}, \sigma_\phi = 2 \text{ deg}$$

Figure 176. Equation. Standard deviation estimates for attitude.

$$\sigma_h = 2.76 \text{ inches}$$

Figure 177. Equation. Standard deviation estimate for the height sensor.

Preliminary calculations showed that performance of the system was not very sensitive to these values within a "valid" range. However, a sufficiently high value was needed for each item to retain valid measurement of vehicle dynamic response within the state estimates, and a sufficiently low value was needed to mitigate the effect of drift. Tuning of the error estimates using preliminary test runs was required, and the final values were influenced by the host vehicle's propensity for dynamic motion in pitch and roll.

Table 26 lists the roughness and cross correlation results for test runs processed using the Kalman smoother with a constant attitude reference. The constant attitude reference produced results equivalent to using actual measurements of pitch and roll attitude when both options applied height-sensor reflection at stops. The lowest cross correlation value is well above the threshold of 0.92 for adequate performance. Note that reproduction of this result depends on tuning as described above, and is not guaranteed for profilers mounted to a host vehicle with a greater propensity for misalignment in pitch and roll.

Table 26. Results for the Kalman smoother with a constant attitude reference.

Run Designation	Peak Roughness (inches/mi)	Average Roughness Error (Percent)	Cross Correlation
S&G, 1.1-sec stop, 0.17 g	134	–1.6	**0.973**
S&G, 1.1-sec stop, 0.20 g	138	–2.2	**0.953**
S&G, 2.1-sec stop, 0.33 g	159	2.6	**0.968**
S&G, 5.8-sec stop, 0.17 g	149	3.7	**0.957**
S&G, 5.7-sec stop, 0.20 g	131	–1.9	**0.949**
S&G, 5.8-sec stop, 0.20 g	148	2.6	**0.964**
S&G, 10.7-sec stop, 0.20 g	157	2.4	**0.967**
NS, 45–7 mi/hr, 0.20 g	156	2.1	**0.976**
Brk, 44–19 mi/hr, 0.19 g	154	1.6	**0.980**
Brk, 45–18 mi/hr, 0.39 g	144	–0.7	**0.976**
Brk, 31–14 mi/hr, 0.16 g	142	–0.8	**0.963**
Brk, 31–14 mi/hr, 0.18 g	145	–0.7	**0.979**
Brk, 31–14 mi/hr, 0.18 g	171	0.6	**0.983**
Brk, 31–12 mi/hr, 0.25 g	153	1.0	**0.987**
Brk, 30–21 mi/hr, 0.84 g	164	4.2	**0.942**
10 mi/hr	146	–0.7	**0.987**
3 mi/hr	147	–2.5	**0.963**

Reference peak roughness value: 152 inches/mi. Adequate cross correlation (> 0.92) is shown in bold.

Kalman Smoother with a Constant Height and Attitude Reference

This implementation of the Kalman smoother demonstrates the potential performance of the system if the GPS is not present or is experiencing an outage. All GPS measurements are replaced with constant estimates of zero, as shown in figure 178.

$$y_{rz,k} = 0, y_{vz,k} = 0, y_{\theta,k} = 0, y_{\phi,k} = 0$$

Figure 178. Equation. Constant height and attitude measurement.

Since all GPS readings are simulated the Kalman filter applies the measurement update at every time step. In this implementation, the measurement model within the Kalman filter functions as a high-pass filter on estimates of height, vertical velocity, pitch, and roll produced by the process model.

In addition to the changes specified when using a constant attitude reference, error estimates for height and vertical velocity measurement are altered as shown in figure 179.

$$\sigma_{rz} = 19.7 \text{ inches}, \sigma_{vz} = 39.4 \text{ inches/sec}$$

Figure 179. Equation. Standard deviation estimates for GPS height and velocity.

Like the error estimates for orientation, these values required tuning using preliminary test runs as described above.

Table 27 provides the results for the Kalman smoother with the constant height and attitude reference in conjunction with height-sensor reflection. This implementation produced results equivalent to using actual GPS measurements. The ability to apply the Kalman smoother in areas without a sufficient sky view for accurate GPS would make this system much more robust. Eliminating the need for GPS sensors altogether reduces equipment cost. However, additional tuning of the measurement model is required. Further, verification for vehicles with diverse pitch and roll response properties and for a greater number of speed change scenarios may be needed.

Table 27. Results for the Kalman smoother with a constant height and attitude reference.

Run Designation	Peak Roughness (inches/mi)	Average Roughness Error (Percent)	Cross Correlation
S&G, 1.1-sec stop, 0.17 g	141	–0.8	**0.981**
S&G, 1.1-sec stop, 0.20 g	140	–2.3	**0.962**
S&G, 2.1-sec stop, 0.33 g	156	1.7	**0.971**
S&G, 5.8-sec stop, 0.17 g	162	4.4	**0.952**
S&G, 5.7-sec stop, 0.20 g	139	–1.4	**0.949**
S&G, 5.8-sec stop, 0.20 g	127	1.4	**0.974**
S&G, 10.7-sec stop, 0.20 g	147	1.9	**0.970**
NS, 45-7 mi/hr, 0.20 g	151	1.9	**0.977**
Brk, 44-19 mi/hr, 0.19 g	154	1.4	**0.980**
Brk, 45-18 mi/hr, 0.39 g	143	–0.7	**0.977**
Brk, 31-14 mi/hr, 0.16 g	143	–0.8	**0.963**
Brk, 31-14 mi/hr, 0.18 g	146	–0.6	**0.979**
Brk, 31-14 mi/hr, 0.18 g	170	0.3	**0.985**
Brk, 31-12 mi/hr, 0.25 g	158	1.1	**0.986**
Brk, 30-21 mi/hr, 0.84 g	164	3.7	**0.943**
10 mi/hr	147	–0.5	**0.988**
3 mi/hr	148	–2.6	**0.957**

Reference peak roughness value: 152 inches/mi. Adequate cross correlation (> 0.92) is shown in bold.

CHAPTER 7. CONCLUSIONS AND RECOMMENDATIONS

SUMMARY

Inertial profilers are limited in their ability to measure IRI during challenging operational conditions. In particular, they are prone to errors in the floating-reference-height signal when the host vehicle travels at low speed, decelerates during braking, or comes to a stop. These errors reduce the accuracy of profiles measured on urban road networks and low-speed roadways and render the measurements of IRI unusable at important locations, such as signalized intersections.

Two important mechanisms contribute to errors in the floating-reference-height signal derived from accelerometer output in typical inertial profilers.

First, the accelerometers are typically fixed in the host-vehicle body. As such, they experience dynamic changes in pitch and roll orientation as the host vehicle reacts to driver inputs, such as braking and steering. Tilt of the sensitive axis causes errors in the measurement of true vertical acceleration and contamination by components of the longitudinal and lateral acceleration. The most common example of this error source occurs when the host vehicle tilts in pitch during braking and a portion of the rearward acceleration projects onto the sensitive axis of the accelerometer. After double integration, this appears as errors in curvature in the floating-reference-height signal, which appears in the profile over the region where the braking occurred.

Accelerometer tilt also causes profile measurement error at very low travel speed because of dynamic response of the profiler host vehicle in pitch and roll to road roughness. When the host vehicle travels at progressively lower speed, the accelerometer signal is contaminated in a frequency range that increasingly corresponds to the wavelength range of interest for measuring the IRI.

Second, bias in the output of the accelerometers causes drift in the floating-reference-height signal. Causes of bias include road grade, cross slope, local variations in the acceleration due to gravity, and temperature changes. During constant-speed operation, the effects of drift are typically confined to very low frequencies and do not contaminate the wavelength range of interest within the profile. However, when the host vehicle decelerates to a very low speed or comes to a stop, the temporal drift in floating-reference-height signal appears within the measured profile over a very small distance range. Often, this manifests as a steep change in elevation. This registers as severe localized roughness and a large upward bias in the average roughness for the road section where the stop occurred.

This research developed and tested the following options for addressing these sources of profile measurement error:

> Error suppression algorithms: These algorithms use specialized numerical procedures applied at low travel speed combined with standard filtering techniques to reduce artificial roughness measured at a stop. These techniques depend only on the use of output from sensors included in the nominal profiler design. As such, they are proposed as short-term solutions for adapting the processing software in existing profilers, and for new profilers when funds are not available to support the cost of additional sensors. In these

algorithms, reduction of artificial roughness at stops comes at the cost of invalid profile measurement at very low speed.

Sensor augmentation: These designs require additional sensors to improve profile measurement at low speed, during braking, and at stops. The additional sensors include body-fixed measurement of profiler acceleration and rotation rate in three dimensions to help resolve acceleration into a consistent vertical direction. The system also includes GPS measurement of host-vehicle height, vertical velocity, pitch inclination, and roll inclination. A multi-rate extended Kalman filter combines the inertial sensors with the GPS outputs to reduce drift in the floating-reference-height signal and errors associated with host-vehicle tilt. Use of an RTS smoother improves the mitigation of drift. Sensor augmentation is proposed as a long-term solution because it requires major changes to profiler hardware and software design.

A custom measurement system was developed and built for this research to enable an experimental demonstration of profile measurement errors caused by accelerometer misalignment and an investigation of the effectiveness of the proposed solutions. The measurement system included the nominal set of sensors that appear in typical profilers, and several additional sensors to support the augmentation approach described above.

The nominal measurement system demonstrated excellent performance in three ways. First, it demonstrated accurate sensor calibration and very low system noise in stationary tests, such as the bounce test and the quiescent test. Second, it measured profile with a high degree of repeatability in the wavelength range of interest for the IRI. Third, it reproduced profiles measured by an inclinometer-based reference device accurately in the wavelength range of interest for the IRI. The system obtained cross correlation for repeatability and accuracy above the level expected for a reference device, but only under specific conditions. These include: (1) operation at a constant speed of 15 mi/hr and above, and (2) consistent lateral tracking for the two measurements under comparison to within 3 inches or less.

The relative performance of error suppression algorithms and sensor augmentation proposed in this research was evaluated using the results from several test runs collected under challenging conditions, including operation at low speed, braking, and operation through a stop. For all test runs, performance is quantified using standard measures for accuracy of longitudinal profile and IRI used by road agencies for pavement network quality assurance and pavement network management.[87,92] These include:

1. Reduction of bias in the peak value of short-interval roughness profiles relative to a reference measurement in test runs with braking and a stop. Peak values are reported in the region where braking ended or the test vehicle came to a stop. This is where the most severe bias typically occurs.

2. Agreement to a reference measurement of average IRI measured over a 0.1-mile test section.

3. Cross correlation to a reference profile measurement using the output of the IRI algorithm over a 0.1-mile test section. Cross correlation of 0.92 or higher is deemed adequate.

Unfortunately, the test runs performed at low speed, with braking, and with stops did not follow the same lateral track followed by the inclinometer-based device. To reduce the confounding effects of tracking errors, the reference profile was measured using a test run at 45 mi/hr with similar tracking to the evaluation runs.

Table 28 summarizes the performance of the suppression algorithms and sensor augmentation options examined in this research. The options appear in three groups: (1) temporal profile calculation algorithms using the nominal sensor set, (2) spatial profile calculation algorithms using the nominal sensor set, and (3) the use of an augmented sensor set and Kalman filtering. In each group, results are provided for incremental improvements on the basic option or alternative implementations.

Table 28 provides cross correlation results and percent error in roughness for selected test runs at low speed, with braking, and with stops. Text in cells with cross correlation above a threshold value of 0.92 is shown in bold. Some cells in table 28 are marked with a dash. In those instances, the results are the same as in the cell above, because the improvement to the algorithm over the one listed in the row above was not in effect for that test run.

In table 28, the basic temporal and spatial algorithms represent use of the nominal inertial profiler sensors and no improvements to the baseline profile calculation algorithm. These algorithms suffer from large errors in measured roughness at low speed, during braking, and at stops. The adaptations "with high-pass filtering" apply the high-pass filters to the accelerometer signal prior to each stage of integration. Application of high-pass filtering in this manner is recommended for both spatial and temporal profile measurement architectures. Although pre-integration high-pass filtering alone does not offer sufficient improvement, it is recommended as an error mitigation strategy.

Adaptive high-pass filtering is recommended for architectures with temporal profile calculation, and high-pass filtering with timer distortion and height sensor reflection is recommended for architectures with spatial profile calculation. Note that each of these algorithms greatly reduces (i.e., suppresses) the erroneous peak roughness for the test runs with the stop and the near stop. However, the algorithms do so by removing both valid and invalid content at low speed, and they both underestimate roughness for the test run at 3 mi/hr. These algorithms offer a short-term option for reducing the largest errors in measured roughness in cases where the funds do not exist for implementing the sensor augmentation strategy proposed in the research.

Table 28. Cross correlation to the reference test run for selected conditions.

Algorithm	Constant Speed 3 mi/hr	Constant Speed 10 mi/hr	Braking 31–14 mi/hr 0.18 g	Near Stop 45–7 mi/hr 0.20 g	Stop & Go 2.1-sec stop 0.33 g	Stop & Go 10.7-sec stop 0.20 g
Basic Temporal Algorithm (TA)	< 0.2 (1622.7)	0.863 (9.2)	0.605 (27.9)	< 0.2 (195.3)	< 0.2 (862.6)	< 0.2 (13,139.7)
TA with High-Pass Filter (HPF)	**0.940** **(−4.2)**	**0.985** **(−0.7)**	**0.963** **(0.6)**	0.578 (17.7)	0.256 (36.8)	< 0.2 (99.5)
TA with Adaptive HPF	0.322 (−51.9)	**0.985** **(−0.8)**	**0.955** **(1.0)**	0.793 (4.9)	0.581 (17.5)	0.724 (9.3)
Basic Spatial Algorithm (SA)	< 0.2 (928.5)	**0.985** **(0.2)**	0.621 (27.2)	< 0.2 (190.8)	< 0.2 (852.5)	< 0.2 (8,607.7)
SA with Spatial HPF	0.746 (14.5)	**0.927** **(−1.0)**	0.900 (1.8)	0.713 (8.1)	< 0.2 (231.3)	< 0.2 (4,946.6)
SA with HPF, Timer Distortion, and Height-Sensor Reflection (HSR)	< 0.2 (−86.6)	—	—	0.756 (3.4)	0.587 (11.7)	0.678 (11.8)
Kalman Filter (KF)	0.855 (2.7)	**0.986** **(1.5)**	0.904 (7.2)	**0.921** **(5.5)**	< 0.2 (40.3)	< 0.2 (90.7)
KF with smoother (KS)	**0.973** **(−1.8)**	**0.988** **(−0.6)**	**0.981** **(0.9)**	**0.977** **(2.1)**	**0.963** **(3.0)**	**0.938** **(2.9)**
KS with HSR	—	—	—	—	**0.972** **(1.9)**	**0.958** **(3.0)**
KS with HSR and a Constant Reference	**0.957** **(−2.6)**	**0.988** **(−0.5)**	**0.985** **(0.3)**	**0.977** **(1.9)**	**0.971** **(1.7)**	**0.970** **(1.9)**

Cells in bold correspond to cross correlation above 0.92. Percent error in roughness is shown in parentheses.

Sensor augmentation with Kalman filtering offered substantial improvement over the basic temporal and spatial algorithms but was not universally better than the error suppression algorithms. However, the Kalman smoother produced results well above the cross correlation threshold of 0.92. Values close to 0.98 imply high-quality measurement of average IRI, peak roughness, and of details within the profile in the wavelength range of interest for the IRI. Further improvement is evident using height-sensor reflection, which uses the height-sensor signal to help mitigate drift in the floating-reference-height signal during stops.

Sensor augmentation and the use of the Kalman smoother with height-sensor reflection is recommended as a long-term option for improving profile measurement at low speed, during braking, and at stops. Implementation of this option is strongly encouraged for road network survey vehicles with profilers that already include some of the additional sensors for other functions, and for any network survey vehicle that is expected to operate on urban and low-speed roads.

The "constant reference" option uses the Kalman filter and smoother but replaces GPS outputs with artificial signals. Rather than using GPS observations to correct low-frequency content in the integrated outputs from the inertial sensors, the constant reference serves as a limit on drift in the position and orientation estimates. This method is recommended as an "urban canyon" mode for systems with GPS sensors. The constant reference option also offers the possibility to reduce sensor cost and mounting complexity.

The "constant reference" option uses the Kalman filter and smoother, but replaces GPS outputs with artificial reference signals. Rather than using genuine GPS observations to correct low-frequency content in the integrated outputs from the inertial sensors, the constant reference serves as a limit on drift in the position and orientation estimates. This method is recommended as an "urban canyon" mode for systems with GPS sensors. The constant reference option also offers the possibility to reduce sensor cost and mounting complexity.

SUGGESTIONS FOR FUTURE RESEARCH

Practical Implementation

The measurement system developed for this research benefited from several advantages that may not exist in typical inertial profilers. These include: (1) mounting of the profile measurement hardware directly to the host-vehicle frame, (2) a high level of protection from electrical noise, (3) recording raw signals at a high rate, (4) redundant provisions to synchronize signals from different subsystems, and (5) the selection of a host vehicle with favorable dynamics. The field performance of a system using the techniques recommended in this research depends, to some extent, on all of these factors. To facilitate retrofit of existing inertial profilers, an examination of these issues is recommended. In particular, work is needed to determine the maximum performance that is possible using a less favorable host vehicle (e.g., shorter wheelbase, higher center of mass) and less favorable mounting practices (e.g., trailer hitch).

Three-Dimensional Surface Measurement

Commercial inertial profilers are now available that provide measurements of the road surface in three dimensions. The typical design includes replacement of the height sensors with a sweeping laser, which is mounted high above the road surface to help capture a wide transverse profile in each sweep. This increases the vulnerability of the range-to-ground measurement to alignment errors. It also places the inertial sensors in a location with a different vibration environment. The methods demonstrated in this research offer potential benefits for those three-dimensional systems. However, some additional provisions may be needed. These include: (1) consideration of the pitch and roll inclination of the sweeping laser, and (2) development of a custom tuning approach to account for the change in vibration environment.

Alternative Measurement Concepts

This research provided options to reduce or eliminate errors in measured longitudinal road profile by improving measurement of the accelerometer-established inertial platform. This approach was taken to create options for improving the performance of a large existing fleet of inertial profilers. Several other measurement concepts have the potential to measure valid profile without the use of an inertial platform.

Many alternative measurement concepts have been proposed in the classical literature but were never adapted for use on a road with live traffic. These options, and others, should be considered for two reasons. First, sufficient computing power is available to leverage data processing and fusion techniques, like those demonstrated in this research, to use multiple sensors and benefit from the strengths of each. Second, other options are available to serve as the host vehicle that may provide more favorable dynamics (e.g., drones).

Computational Efficiency

Using the Kalman filter required only a modest computational load, in part because the calculations associated with the measurement model were only needed when the GPS system provided new observations. In contrast, the RTS smoother required heavy computation at the same rate as the analog sensor outputs were digitized, and storage of more than 50 signals for processing after the completion of each test run. Additional research may reveal methods for decreasing the required storage and computational load. Substantial savings are possible if a valid method can be found to reduce the frequency at which the state error covariance and Kalman gain matrices are updated.

This research used a fixed-interval smoother to improve the state estimates from the Kalman filter. Use of a fixed-interval smoother is cumbersome for very long pavement sections or test runs that include a long stop. A fixed lag smoother offers the option to reduce demands on signal storage at the cost of an increase in computational load. A fixed-lag smoother was not used because the lag required for an accurate estimate of the floating reference height depends heavily on the host-vehicle speed profile. For example, no lag is needed at constant speed, and a lag that goes well beyond the stop is needed for stop-and-go operation. Development of an adaptive fixed-lag smoother may improve the trade-off between performance and storage demand compared to the fixed-interval smoother used in this research.

APPENDIX A. DIGITAL FILTERING TECHNICAL NOTES

This appendix describes digital filters used in support of the research. All of the filters are based on a cascaded form of the third-order Butterworth filter.

DESIGNATIONS

For the high-pass filter, the transfer function, $H(s)$, is shown in figure 180.

$$H(s) = \frac{s^3}{s^3 + 2\omega_a s^2 + 2\omega_a^2 s + \omega_a^3}$$

Figure 180. Equation. High-pass filter transfer function.

In figure 180, ω_a is the analog (angular) cut-off frequency and s is the Laplace operator. In this implementation, the filter comprises a first-order Butterworth filter, $H_1(s)$, and a complementary second-order stage, $H_2(s)$. Their transfer functions are shown in figure 181 and figure 182, respectively.

$$H_1(s) = \frac{s}{s + \omega_a}$$

Figure 181. Equation. First order Butterworth high-pass transfer function.

$$H_2(s) = \frac{s^2}{s^2 + \omega_a s + \omega_a^2}$$

Figure 182. Equation. Second order complementary high-pass transfer function.

Likewise, the cascaded form of the low-pass filter includes the transfer functions shown in figure 183 and figure 184.

$$H_1(s) = \frac{\omega_a}{s + \omega_a}$$

Figure 183. Equation. First order Butterworth low-pass transfer function.

$$H_2(s) = \frac{\omega_a^2}{s^2 + \omega_a s + \omega_a^2}$$

Figure 184. Equation. Second order complementary low-pass transfer function.

This document assigns the following designations to the filter stages:

LPF$_{B3S1}$: Low-pass filter, first-order stage.

LPF$_{B3S2}$: Low-pass filter, second-order stage.

HPF$_{B3S1}$: High-pass filter, first-order stage.

HPF_{B3S2}: High-pass filter, second-order stage.

These designations pertain to application of the filters beginning at the earliest available sample and progressing forward. In some cases, these filtering stages are applied in reverse to cancel the phase shift imposed by the forward-running stages. That is, filtering is initiated at the latest available sample and progresses backward. In such cases, the designations include an "R" at the end of the subscript (e.g., HPF_{B3S1R}).

An abbreviated designation for the high-pass filter (HPF_{B3}) and low-pass filter (LPF_{B3}) indicates that the first-order and second-order stages were applied in succession. For example, LPF_{B3} implies the application of LPF_{B3S1} followed by LPF_{B3S2}.

When both stages of the forward and reverse filters are applied without other processing steps between any of them, they are applied in a specific order to minimize initial transient responses: first-order stage, forward; second-order stage, reverse, first-order stage, reverse; and second-order stage, forward. Together, these four stages make up a sixth-order filter. The abbreviated designations for these filter sets are:

HPF_{B3x2}: HPF_{B3S1}, HPF_{B3S2R}, HPF_{B3S1R}, and HPF_{B3S2}.

LPF_{B3x2}: LPF_{B3S1}, LPF_{B3S2R}, LPF_{B3S1R}, and LPF_{B3S2}.

DIGITIZATION

The bilinear approximation recasts the transfer functions into the z-domain, as shown in figure 185. In figure 185, Δt is the sampling period of the digital signal. Using the substitution shown in figure 186 accounts for the non-linear relationship between the analog cut-off frequency and the digital cut-off frequency. In figure 186, f_c is the digital cut-off frequency in Hertz.

$$s = \frac{2}{\Delta t} \frac{1 - z^{-1}}{1 + z^{-1}}$$

Figure 185. Equation. Bilinear approximation.

$$\omega_a = \frac{2}{\Delta t} \tan(\pi f_c \Delta t)$$

Figure 186. Equation. Substitution for the cut-off frequency.

Manipulation of the z-domain transfer functions into the form shown in figure 187 provides the coefficients for the digital filtering equations.

$$H(z) = \frac{\sum_{i=0}^{n} N_i z^{-i}}{\sum_{i=0}^{n} D_i z^{-i}}$$

Figure 187. Equation. Z-domain transfer functions.

In figure 187, n is the order of the filter, z^{-i} represents a delay of i samples, and D_i and N_i are filter coefficients. Figure 188 shows the discrete equation for the forward-running filter. In figure 188, $x(t_k)$ and $y(t_k)$ are the input and output signals at discrete sample number k, and K is the number of samples in each signal. Figure 189 shows the discrete equation for the backward-running filter.

$$y(t_k) = \frac{1}{D_0}\left(\sum_{i=0}^{n} N_i x(t_{k-i}) - \sum_{i=1}^{n} D_i y(t_{k-i}) \right), \text{ for } k = n+1, n+2, \ldots, K$$

Figure 188. Equation. Forward-running filter.

$$y(t_k) = \frac{1}{D_0}\left(\sum_{i=0}^{n} N_i x(t_{k+i}) - \sum_{i=1}^{n} D_i y(t_{k+i}) \right), \text{ for } k = K-n, K-n-1, \ldots, 1$$

Figure 189. Equation. Backward-running filter.

Table 29 provides the coefficients for the four basic filtering stages. For notational simplicity, the substitution shown in figure 190 is used.

$$c = \tan(\pi f_c \Delta t)$$

Figure 190. Equation. Notational substitution.

Table 29. Filter coefficients.

Filter	D_0	D_1	D_2	N_0	N_1	N_2
LPF$_{B3S1}$	$c + 1$	$c - 1$	—	c	c	—
LPF$_{B3S2}$	$c^2 + c + 1$	$2(c^2 - 1)$	$c^2 - c + 1$	c^2	$2c^2$	c^2
HPF$_{B3S1}$	$c + 1$	$c - 1$	—	1	-1	—
HPF$_{B3S2}$	$c^2 + c + 1$	$2(c^2 - 1)$	$c^2 - c + 1$	1	-2	1

INITIALIZATION

Figure 191 through figure 194 provide the initialization equations for the forward-running filters.

$$y(t_1) = x(t_1)$$

Figure 191. Equation. Initialization of LPF$_{B3S1}$.

$$y(t_1) = x(t_1), \; y(t_2) = \frac{1}{D_0}\left(N_0 x(t_2) + (N_1 + N_2)x(t_1) - (D_1 + D_2)y(t_1) \right)$$

Figure 192. Equation. Initialization of LPF$_{B3S2}$.

$$y(t_1) = -\frac{D_1}{D_0} x(t_1)$$

Figure 193. Equation. Initialization of HPF$_{B3S1}$.

$$y(t_1) = -\frac{D_1 + D_2}{D_0} x(t_1), \ y(t_2) = \frac{1}{D_0}\left(N_0 x(t_2) + (N_1 + N_2) x(t_1) - (D_1 + D_2) y(t_1)\right)$$

Figure 194. Equation. Initialization of HPF$_{B3S2}$.

Figure 195 through figure 198 provide the initialization equations for the forward-running filters.

$$y(t_K) = x(t_K)$$

Figure 195. Equation. Initialization of LPF$_{B3S1R}$.

$$y(t_K) = x(t_K), \ y(t_{K-1}) = \frac{1}{D_0}\left(N_0 x(t_{K-1}) + (N_1 + N_2) x(t_K) - (D_1 + D_2) y(t_K)\right)$$

Figure 196. Equation. Initialization of LPF$_{B3S2R}$.

$$y(t_K) = -\frac{D_1}{D_0} x(t_K)$$

Figure 197. Equation. Initialization of HPF$_{B3S1R}$.

$$y(t_K) = -\frac{D_1 + D_2}{D_0} x(t_K), \ y(t_{K-1}) = \frac{1}{D_0}\left(N_0 x(t_K) + (N_1 + N_2) x(t_{K-1}) - (D_1 + D_2) y(t_K)\right)$$

Figure 198. Equation. Initialization of HPF$_{B3S2R}$.

CUT-OFF FREQUENCY

The cut-off frequency for these filters is expressed in terms of the cut-off frequency for the third-order filter, which is the cut-off for the combination of the first- and second-order stages. Note that the gain of the first-order stage is also reduced by 3 dB at the cut-off frequency, because it is a Butterworth filter. The gain of the second-order complementary filter is unity at the cut-off frequency. The gain of the second-order complementary high-pass filter is reduced by 3 dB at $0.78615f_c$, and the gain of the second-order complementary low-pass filter is reduced by 3 dB at $1.27202f_c$.

To obtain 3 dB gain reduction for the sixth-order combination of forward and reverse high-pass filtering stages (i.e., HPF$_{B3x2}$) at a desired frequency, f_{-3dB}, the cut-off frequency for the third-order filters must be set as shown in figure 199. Figure 200 provides the setting for the low-pass filter.

$$f_c = \left(\sqrt{2} - 1\right)^{1/6} f_{-3dB}$$

Figure 199. Equation. High-pass filter cut-off frequency.

$$f_c = \left(\sqrt{2} - 1\right)^{-1/6} f_{-3dB}$$

Figure 200. Equation. Low-pass filter cut-off frequency.

SPATIAL FILTERING

Spatial filtering is performed in the distance domain, rather than the time domain. The filters operate as described above. However, the independent variable x_k replaces t_k and the distance increment Δx replaces the time increment Δt. For convenience of interpretation, cut-off values for spatial filtering are expressed in terms of wavelength (λ_c), rather than spatial frequency. To obtain a 3 dB reduction for the sixth-order combination of forward and reverse high-pass filtering stages (i.e., HPF$_{B3x2}$) at a desired wavelength, λ_{-3dB}, the cut-off wavelength for the third-order filters must be set as shown in figure 201.

$$\lambda_c = \left(\sqrt{2} - 1\right)^{-1/6} \lambda_{-3dB}$$

Figure 201. Equation. High-pass filter cut-off wavelength.

APPENDIX B: MEASUREMENT SYSTEM PHOTOS

All images in Appendix B are provided by Steve Karamihas.

Figure 202. Image. Left side view.

Figure 203. Image. Right side view.
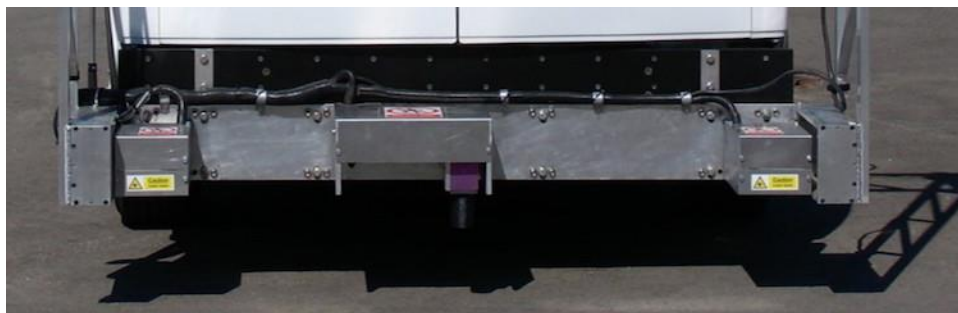
Figure 204. Image. Lower sensor rack.

Figure 205. Image. Rear view.

Figure 206. Image. Rotational encoder mounting hardware.

Figure 207. Image. Right sensor pod, underside, lower cover removed.

Figure 208. Image. Right sensor pod, upper cover removed.

Figure 209. Image. Center sensor pod, cover removed.

Figure 210. Image. Forward camera and lane tracker camera.

Figure 211. Image. Front left GPS antenna (pitch rover).

Figure 212. Image. Left front laser.

Figure 213. Image. Vehicle interior.

Figure 214. Image. DAS exterior.

Figure 215. Image. DAS, power supply, and GPS receivers.

Figure 216. Image. Vehicle interior with outer hardware stowed.

APPENDIX C: LINEARIZED SYSTEM EQUATIONS

The figures in this appendix present the linearized system equations for the extended Kalman filter described in Chapter 6. For ease of interpretation, the subscripts for time step are omitted.
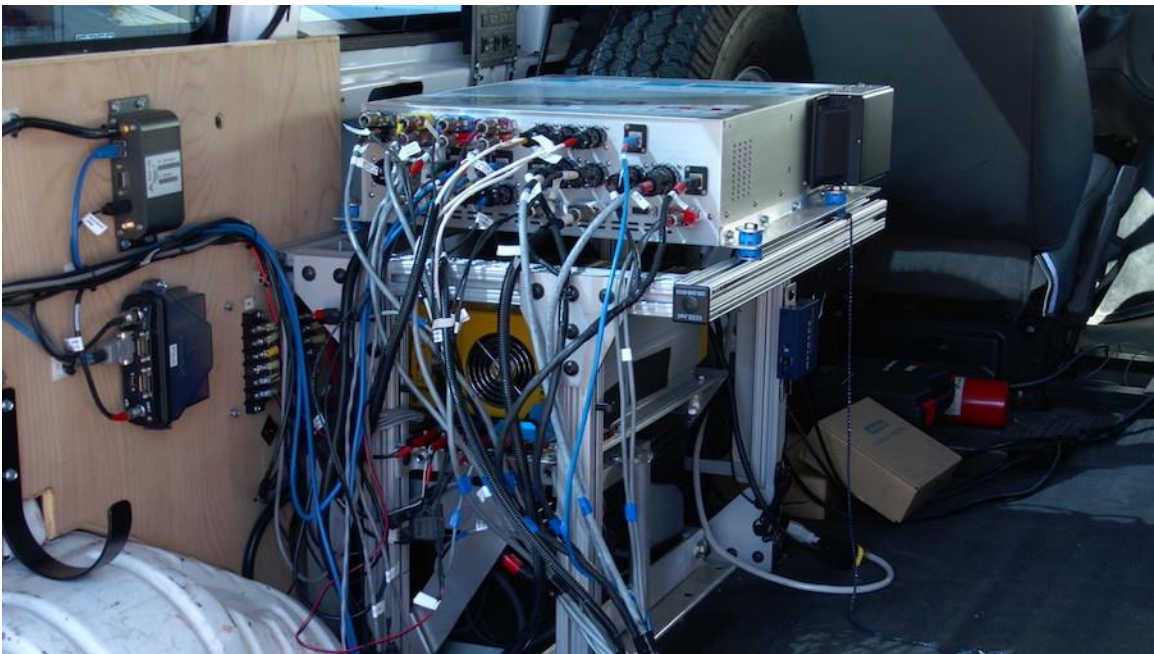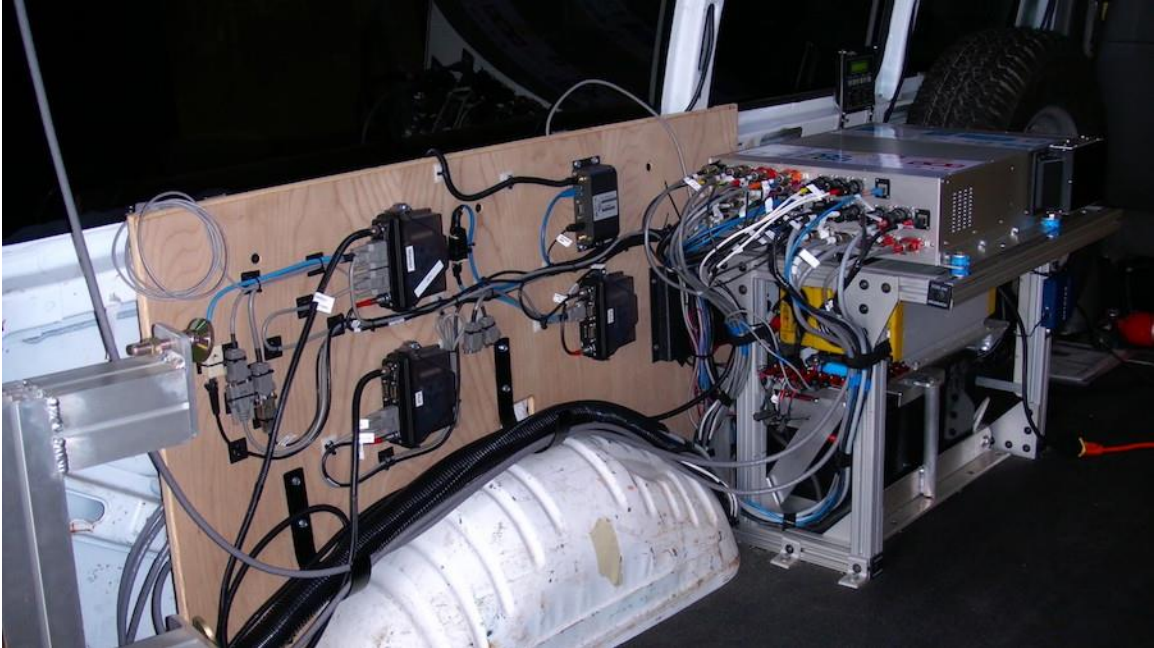
$$s_\theta = \sin(\theta),\ c_\theta = \cos(\theta),\ s_\phi = \sin(\phi),\ c_\phi = \cos(\phi)$$

Figure 217. Equation. Abbreviations for sine and cosine functions.

$$x = \left\{ r_{zp}^n, v_{zp}^n, \theta, \phi, \delta_a, \delta_{\omega_1}, \delta_{\omega_2} \right\}^T$$

Figure 218. Equation. State vector.

$$A = \begin{bmatrix}
1 & \Delta t & A[1,3] & A[1,4] & \Delta t^2/2 & 0 & 0 \\
0 & 1 & A[2,3] & A[2,4] & \Delta t & 0 & 0 \\
0 & 0 & 1 & A[3,4] & 0 & 0 & c_\phi \Delta t \\
0 & 0 & A[4,3] & A[4,4] & 0 & \Delta t & s_\theta s_\phi \Delta t / c_\theta \\
0 & 0 & 0 & 0 & 1 & 0 & 0 \\
0 & 0 & 0 & 0 & 0 & 1 & 0 \\
0 & 0 & 0 & 0 & 0 & 0 & 1
\end{bmatrix}$$

$$A[1,3] = (-c_\theta u_{ax} - s_\theta s_\phi u_{ay} - s_\theta c_\phi u_{az})\Delta t^2/2$$

$$A[1,4] = c_\theta(c_\phi u_{ay} - s_\phi u_{az})\Delta t^2/2$$

$$A[2,3] = (-c_\theta u_{ax} - s_\theta s_\phi u_{ay} - s_\theta c_\phi u_{az})\Delta t$$

$$A[2,4] = c_\theta(c_\phi u_{ay} - s_\phi u_{az})\Delta t$$

$$A[3,4] = -\Delta t\left(s_\phi(u_{\omega_2} + \delta_{\omega_2}) + c_\phi u_{\omega_3}\right)$$

$$A[4,3] = \left(c_\phi u_{\omega_3} + s_\phi(u_{\omega_2} + \delta_{\omega_2})\right)\dfrac{\Delta t}{c_\theta^2}$$

$$A[4,4] = 1 + \left(c_\phi(u_{\omega_2} + \delta_{\omega_2}) - s_\phi u_{\omega_3}\right)s_\theta \Delta t / c_\theta$$

Figure 219. Equations. Linearized state transition matrix.

$$WQW^T$$

Figure 220. Equation. Linearized process noise covariance.

$$Q = \mathrm{diag}\left(\sigma_a^2, \sigma_{\omega_1}^2, \sigma_{\omega_2}^2, \sigma_{\omega_3}^2, \sigma_{a'}^2, \sigma_{\omega_1'}^2, \sigma_{\omega_2'}^2\right)$$

Figure 221. Equations. Q matrix.

$$W = \begin{bmatrix} \Delta t^2/2 & 0 & 0 & 0 & 0 & 0 & 0 \\ \Delta t & 0 & 0 & 0 & 0 & 0 & 0 \\ 0 & 0 & c_\phi \Delta t & -s_\phi \Delta t & 0 & 0 & 0 \\ 0 & \Delta t & s_\theta s_\phi \Delta t/c_\theta & s_\theta c_\phi \Delta t/c_\theta & 0 & 0 & 0 \\ 0 & 0 & 0 & 0 & 1 & 0 & 0 \\ 0 & 0 & 0 & 0 & 0 & 1 & 0 \\ 0 & 0 & 0 & 0 & 0 & 0 & 1 \end{bmatrix}$$

Figure 222. Equation. W matrix.

$$y = \left\{ y_{rz}, y_{vz}, y_\theta, y_\phi \right\}^T$$

Figure 223. Equation. Measurement vector.

$$H = \begin{bmatrix} 1 & 0 & H[1,3] & H[1,4] & 0 & 0 & 0 \\ 0 & 1 & H[2,3] & H[2,4] & 0 & c_\theta(c_\phi l_y - s_\phi l_z) & -s_\theta l_z \\ 0 & 0 & 1 & 0 & 0 & 0 & 0 \\ 0 & 0 & -\dfrac{s_\theta s_\phi}{\sqrt{1-(c_\theta s_\phi)^2}} & \dfrac{c_\theta c_\phi}{\sqrt{1-(c_\theta s_\phi)^2}} & 0 & 0 & 0 \end{bmatrix}$$

$$H[1,3] = -s_\theta(s_\phi l_y + c_\phi l_z)$$
$$H[1,4] = c_\theta(c_\phi l_y - s_\phi l_z)$$
$$H[2,3] = -c_\theta\left((u_{\omega_2} + \delta_{\omega_2})l_z - u_{\omega_3}l_y\right) - s_\theta(u_{\omega_1} + \delta_{\omega_1})(c_\phi l_y - s_\phi l_z)$$
$$H[2,4] = -c_\theta(u_{\omega_1} + \delta_{\omega_1})(s_\phi l_y + c_\phi l_z)$$

Figure 224. Equation. Linearized measurement matrix.

$$R = \mathrm{diag}(\sigma_{rz}^2, \sigma_{vz}^2, \sigma_\theta^2, \sigma_\phi^2)$$

Figure 225. Equation. Linearized measurement noise covariance.

ACKNOWLEDGEMENTS

REFERENCES

1. *National Transportation Statistics 2021, 50th Anniversary Edition*. U.S. Department of Transportation, Bureau of Transportation Statistics (2019) 561 p.

2. "Highway Statistics." U.S. Department of Transportation, Federal Highway Administration (2016). https://www.fhwa.dot.gov/policyinformation/statistics/2016/

3. Harrison, F. and H.-A. Park, "Comparative Performance Measurement: Pavement Smoothness." National Cooperative Highway Research Program, Final Report, Project 20-24(37)(B) (2008) 53 p.

4. Choubane, B., Scott, S., Mraz, A., and J. Schiffermuller, "Pavement Smoothness Acceptance Testing: Survey of Current State Practices." *State of Florida Department of Transportation Research Report Number FL/DOT/SMO/10-533* (2010) 23 p.

5. *National Performance Management Measures; Assessing Pavement Condition for the National Highway Performance Program and Bridge Condition for the National Highway Performance Program*, U.S. Department of Transportation, Federal highway Administration, Federal Register, Vol. 82, No. 11 (2017) p. 5925.

6. "Better Data Needed to Rate the Nation's Highway Conditions." *United States General Accounting Office Report to Congressional Committees GAO/RCED-99-264* (1999) 20 p.

7. "FHWA's Model for Estimating Highway Needs Is Generally Reasonable, Despite Limitations." *United States General Accounting Office Report to Congressional Committees GAO/RCED-00-133* (2000) 38 p.

8. Sayers, M. W., "On the Calculation of International Roughness Index from Longitudinal Road Profile." *Transportation Research Record 1501* (1995) pp. 1-12.

9. Flintsch, G. and K. K. McGhee, "Quality Management of Pavement Condition Data Collection." *National Cooperative Highway Research Program Synthesis of Highway Practice 401* (2009) 144 p.

10. Dye Management Group, Inc., "Development of Levels of Service for the Interstate Highway System." *National Cooperative Highway Research Program Report 677* (2010) 40 p.

11. "MAP-21: Moving Ahead for Progress in the 21st Century Act." **§**1203; 23 USC 150.

12. "MAP-21: Moving Ahead for Progress in the 21st Century Act." **§**1104; 23 USC 103.

13. "Highway Performance Monitoring System. Field Manual." U.S. Department of Transportation, Federal Highway Administration, Office of Policy Information, December, 2016.

14. Karamihas, S. M., Gillespie, T. D., Perera, R. W., and S. D. Kohn, "Guidelines for Longitudinal Pavement Profile Measurement." *National Cooperative Highway Research Program Report 434* (2000) 75 p.

15. Walker, R. S. and E. Becker, "Collecting Stop and Go Inertial Profile Measurements." *The University of Texas at Arlington Technical Report 0-4880-1* (2006) 52 p.

16. "MAP-21: Moving Ahead for Progress in the 21st Century Act." § 1106; 23 USC 119.

17. "Highway Statistics." U.S. Department of Transportation, Federal Highway Administration (2018). https://www.fhwa.dot.gov/policyinformation/statistics/2018/

18. "The Federal Lands Highway Program, 2012 Year in Review." U.S. Department of Transportation, Federal Highway Administration, 2012, 47 p.

19. "Federal Lands Highway Project Development and Design Manual." U.S. Department of Transportation, Federal Highway Administration, 2014.

20. Spangler, E. B. and W. J. Kelly, "Servo-Seismic Method of Measuring Profile." *Highway Research Board Bulletin 328* (1962) pp. 33-51.

21. Spangler, E. B. and W. J. Kelly, "GMR Road Profilometer. A Method for Measuring Road Profile." *General Motors Corporation Research Laboratories Research Publication GMR-452* (1964) 44 p.

22. Hveem, F. N., "Devices for Recording and Evaluating Pavement Roughness." *Highway Research Board Bulletin 264* (1960) pp. 1-26.

23. Holbrook, L. F., "Prediction of Subjective Response to Road Roughness Using the General Motors-Michigan Department of State Highways Rapid Travel Profilometer." *Michigan Department of State Highways Research Report No. R-719* (1970) 65 p.

24. Houbolt, J. C., "Runway Roughness Studies in the Aeronautical Field." *Transactions of the American Society of Civil Engineers, Journal of the Air Transport Division*, Vol. 87, No. AT1 (1961) pp. 11-31.

25. Hutchinson, B. G., "Analysis of Road Roughness Records by Power Spectral Density Techniques." *Department of Highways, Ontario, Canada Report No. RR-101* (1965) 81 p.

26. Dodds, C. J. and J. D. Robson, "The Description of Road Surface Roughness." *Journal of Sound and Vibration*, Vol. 31, No. 2 (1973) pp. 175-183.

27. Spangler, E. B. and W. J. Kelly, "GMR Road Profilometer–A Method for Measuring Road Profile." *Highway Research Record No. 121* (1966) pp. 27-54.

28. Darlington, J. R. and P. Milliman, "A Progress Report on the Evaluation and Application Study of the General Motors Rapid Travel Road Profilometer." *Highway Research Record 214* (1968) pp. 50-67.

29. Walker, R. S. and W. R. Hudson, "A Road Profile Data Gathering and Analysis System." *Highway Research Record No. 311* (1970) pp. 36-54.

30. Brickman, A. D., Wambold, J. C., and J. R. Zimmerman, "An Amplitude Frequency Description of Road Roughness." *Highway Research Board Special Report 116* (1971) pp. 53-67.

31. Darlington, J. R., "High-Speed Profilometry." *Highway Research Record No. 362* (1971) pp. 98-103.

32. Burchett, J. L., Rizenbergs, R. L., and T. A. Moore, "Surface Dynamics Profilometer and Quarter-Car Simulator: Description, Evaluation, and Adaptation." *Kentucky Department of Transportation Research Report 465* (1977) p.

33. Darlington, J. R., "Evaluation and Application Study of the General Motors Corporation Rapid Travel Profilometer." *Michigan Department of State Highways Research Report No. R-731* (1970) 92 p.

34. Sayers, M. W. and S. M. Karamihas, "The Little Book of Profiling." University of Michigan Transportation Research Institute (1998) 100 p.

35. ASTM E-950/E-950M-09. *Standard Test Method for Measuring the Longitudinal Profile of Traveled Surfaces with an Accelerometer Established Inertial Profiling Reference.*

36. Huft, D. L., "South Dakota Profilometer." *Transportation Research Record No. 1000* (1984) pp. 1-8.

37. Chaka, R. J., "The Design and Development of a Highway Speed Road Profilometer." *Society of Automotive Engineers Paper No. 780064* (1978) 5 p.

38. Sayers, M. W. and T. D. Gillespie, "The Ann Arbor Road Profilometer Meeting." *Federal Highway Administration Report FHWA/RD-86/100, University of Michigan Transportation Research Institute Report UMTRI-86-19* (1986) 237 p.

39. Gillespie, T. D., Sayers, M. W., and M. R. Hagan, "Methodology for Road Roughness Profiling and Rut Depth Measurement." *Federal Highway Administration Report FHWA/RD-87/042, University of Michigan Transportation Research Institute Report UMTRI-86-54* (1987) 50 p.

40. AASHTO M328-14. *Standard Equipment Specification for Inertial Profiler*.

41. Gagarin, N., Mekemson, J., Chintakunta, S., and R. Orthmeyer, "Development of Operational Constraints of Road Profiling Equipment Based on a Single-Axis Accelerometer," Task Order 15, FHWA Contract DTFH61-06-D-00021 (2011).

42. Dembski, N., Rizzoni, G., and A. Soliman, "Development of a Terrain Severity Measurement System Utilizing Optical Lasers." Modeling and Simulation for Military Applications, *Proc of SPIE* Vol. 6228, 622805 (2006).

43. Dembski, N., Rizzoni, G., Soliman, A., Malmedahl, G., and L. Disaro, "The Development of a Terrain Severity Measurement System." *Proc of the ASME,* DSC-Vol. 75-1 (2006) pp. 217-226.

44. Demić, M., Diligenski, D., and I. Demić, "New Design of a Road Profiler." *International Journal of Automotive Technology*, Vol. 11, No. 6 (2010) pp. 801-808.

45. Hudson, W. R., "High-Speed Road Profile Equipment Evaluation." *Highway Research Record No. 189* (1967) pp. 150-165.

46. Pong, M.-F. M., "The Development of an Extensive-Range Dynamic Road Profile and Roughness Measuring System." Ph.D. Dissertation, The Pennsylvania State University College of Engineering (1992) 256 p.

47. Kern, J. V. and J. B. Ferris, "Development of a 3-D Vehicle Terrain Measurement System Part I: Equipment Setup." 2007-51-0232, *Proceedings of the International Society for Terrain-Vehicle Systems*, Fairbanks, AK (2007).

48. Wagner, S. M., Kern, J. V., Israel, W. B., and J. B. Ferris, "Development of a 3-D Vehicle Terrain Measurement System Part II: Signal Processing and Validation." 2007-51-0333, *Proceedings of the International Society for Terrain-Vehicle Systems*, Fairbanks, AK (2007).

49. Liu, F., Dembski, N., Soliman, A., Rizzoni, G., Thompson, B., and B. Vaughn, "A Kalman-Filter Based Multi-Sensor Terrain Profile Measurement System: Principle, Implementation and Validation" Modeling and Simulation for Military Applications, *Proc of SPIE* Vol. 6965, 69650J (2008).

50. Qin, Y., Guan, J., and L. Gu, "The Research of Road Profile Estimation Based on Acceleration Measurement." *Applied Mechanics and Materials*, Vols. 226-228 (2012) pp. 1614-1617.

51. Wang, Q., McDaniel, J. G., Sun, N. X., and M. L. Wang, "Road Profile Estimation of City Roads Using DTPS." Sensors and Smart Structures Technologies for Civil, Mechanical, and Aerospace Systems, *Proc of SPIE*, Vol. 8692, 86923C-1 (2013).

52. Tomiyama, K., Kawamura, A., Nakajima, S., Ishida, T., and M. Jomoto, "A Mobile Data Collection System Using Accelerometers for Pavement Maintenance and Rehabilitation." *8th International Conference on Managing Pavement Assets*, Paper ICMPA142 (2011).

53. Nguyen, S., "System Identification for a model Based Observer Road Roughness Profiler." Master's Thesis, University of Arkansas (2006).

54. Harris, N. K., Gonzalez, A., OBrien, E. J., and P. McGetrick, "Characterisation of Pavement Profile Heights Using Accelerometer Readings and a Combinatorial Optimisation Technique." *Journal of Sound and Vibration*, Vol. 329 (2010) pp. 497-508.

55. Yousefzadeh, M., Azadi, S., and A. Soltani, "Road Profile Estimation Using Neural Network Algorithm." *Journal of Mechanical Science and Technology*, Vol. 24, No. 3 (2010) pp. 743-754.

56. Solhmirzaei, A., Azadi, S., and R. Kazemi, "Road Profile Estimation Using Wavelet Neural Network and 7-DOF Vehicle Dynamic Systems." *Journal of Mechanical Science and Technology*, Vol. 26, No. 10 (2012) pp. 3029-3036.

57. Imine, H., M'Sirdi, N. K., and Y. Delanne, "Adaptive Observers and Estimation of the Road Profile." *SAE Paper 2003-01-1282* (2003) 6 p.

58. Imine, H. and Y. Delanne, "Triangular Observers for Road Profiles (sic) Inputs Estimation and Vehicle Dynamics Analysis." Proceedings of the 2005 IEEE International Conference on Robotics and Automation, Barcelona, Spain, April, 2005.

59. Imine, H., Delanne, Y., and N. K. M'Sirdi, "Road Profile Inputs for Evaluation of the Loads on the Wheels." *Vehicle System Dynamics*, Vol. 43, Supplement 1 (2005) pp. 359-369.

60. Imine, H. and L. Fridman, "Road Profile Estimation in Heavy Vehicle Dynamics Simulation." *International Journal of Vehicle Design*, Vol. 47, Nos. 1/2/3/4 (2008) pp. 234-249.

61. Rabhi, A. H., Imine, N. M., Sirdi and Y. Delanne, "Observers With Unknown Inputs to Estimate Contact Forces and Road Profile." *AVCS'04 International Conference on Advances in Vehicle Control and Safety*, Genova, Italy, October 28-31, 2004.

62. Rabhi, K. N., et al., "Second Order Sliding Mode Observer for Estimation of Road Profile." *International Conference on Variable Structure Systems*, Alghero, Italy, 2006, pp. 161-165.

63. Rabhi, K. N., M'Sirdi, N. K., Naamane, A., and B. Jaballah, "Estimation of Contact Forces and Road Profile Using High-Order Sliding Modes." *International Journal of Vehicle Autonomous Systems*, Vol. 8, No. 1 (2010) pp. 23-28.

64. Rath, J. J., Veluvolu, K. C., and M. Defoort, "Simultaneous Estimation of Road Profile and Tire Road Friction for Automotive Vehicle." IEEE Transactions on Vehicular Technology, Vol. 64, No. 10 (2015) pp. 4461-4471.

65. Still, P. B. and P. G. Jordan, "Evaluation of the TRRL High-Speed Profilometer." Transport and Road Research Laboratory Report 922 (1980) 45 p.

66. Yi, Z. and M. Rong-Gui, "A Study of Pavement Roughness Measurement System Based on Laser Ranger (sic) Finder." *International Conference on Image Analysis and Signal Processing 2009*, IASP 2009.

67. Sayers, M. W., Gillespie, T. D., and W. D. O. Paterson, "Guidelines for Conducting and Calibrating Road Roughness Measurements." *World Bank Technical Paper Number 46* (1986) 87 p.

68. Sayers, M. W., "On the Calculation of International Roughness Index from Longitudinal Road Profile." *Transportation Research Record 1501* (1995) pp. 1-12.

69. Sayers, M. W., Gillespie, T. D., and C. A. V. Queiroz, "The International Road Roughness Experiment." *World Bank Technical Paper Number 45* (1986) 453 p.

70. "1999 Status of the Nation's Highways, Bridges, and Transit: Conditions and Performance." U.S. Department of Transportation, Federal Highway Administration Report to Congress (2000).

71. Sayers, M. W., "Profiles of Roughness." *Transportation Research Record 1260* (1990) pp. 106-111.

72. Swan, M. and S. M. Karamihas, "Use of a Ride Quality Index for Construction Quality Control and Acceptance Specifications." *Transportation Research Record 1861* (2003) pp. 10-16.

73. Karamihas, S. M. and K. Senn, "Profile Analysis of Arizona Specific Pavement Studies 5 Project." *Transportation Research Record 2095* (2009) pp. 144-152.

74. AASHTO R 54-14. *Standard Practice for Accepting Pavement Ride Quality When Measured Using Inertial Profiling Systems.*

75. Karamihas, S. M., "Critical Profiler Accuracy Requirements." *University of Michigan Transportation Research Institute Report UMTRI-2005-24* (2005) 115 p.

76. Andrén, P., "Power Spectral Approximations of Longitudinal Road Profiles." *International Journal of Vehicle Design*, Vol. 40, No. 1/2/3 (2009) pp. 2-14.

77. ISO 8608:2016. *Mechanical vibration — Road surface profiles — Reporting of measured data*.

78. Kropáč, O. and P. Múčka, (2009) "Effects of Longitudinal Road Waviness on Vehicle Vibration Response." *Vehicle System Dynamics*, Vol. 47, No. 2 (2009) pp. 135-153.

79. Dodds, C. J., and J. D. Robson, "The Description of Road Surface Roughness." *Journal of Sound and Vibration*, Vol. 31, No. 2 (1973) pp. 175-183.

80. La Barre, R. P., Forbes, R. T., and S. Andrew, "The Measurement and Analysis of Road Surface Roughness." *Motor Industry Research Association, Report 1970/5* (1970) 31 p.

81. Sayers, M. W., "Characteristic Power Spectral Density Functions for Vertical and Roll Components of Road Roughness." American Society of Mechanical Engineers, *AMD-Vol. 80* (1986d) pp. 113-129.

82. Sayers, M. W., "Dynamic Terrain Inputs to Predict Structural Integrity of Ground Vehicles." *University of Michigan Transportation Research Institute Report UMTRI-88-16* (1988) 114 p.

83. Karamihas, S. M., "Golden-Car Simulation Speed and Its Implications to the Relevance of the IRI." *American Society for Testing and Materials STP 1555* (2012) pp. 248-266.

84. Janoff, M. S., "Pavement Roughness and Rideability Field Evaluation." *National Cooperative Highway Research Program Report 308* (1988) 54 p.

85. Sayers, M. W. and S. M. Karamihas, "Estimation of Rideability by Analyzing Longitudinal Road Profile." *Transportation Research Record 1536* (1996) pp. 110-116.

86. Karamihas, S. M., "Development of Cross Correlation for Objective Comparison of Profiles." *International Journal of Vehicle Design*, Vol. 36, Nos. 2/3 (2004) pp. 173-193.

87. AASHTO R 56-14. *Certification of Inertial Profiling Systems*.

88. Sayers, M. W. and S. M. Karamihas, "Interpretation of Road Roughness Profile Data." *University of Michigan Transportation Research Institute Report UMTRI-96-19* (1996) 166 p.

89. Pong, M.-F. M. and J. C. Wambold, "Evaluation of Computation Methods for Accelerometer-Established Inertial Profiling Reference Systems." *Transportation Research Record 1348* (1992) pp. 8-17.

90. Perera, R. W. and S. Kohn, "Quantification of Smoothness Index Differences Related to LTPP Equipment Type." *Federal Highway Administration Report FHWA-HRT-05-054* (2005) 157 p.

91. J670-2008. *Vehicle Dynamics Terminology*.

92. AASHTO R 57-14. *Standard Practice for Operating Inertial Profiling Systems.*

93. Karamihas, S. M. and R. W. Perera, "Evaluation of Potential Pavement Profile Reference Devices: 2013 Reference Profiler Benchmark Text Evaluation." *University of Michigan Transportation Research Institute Report UMTRI-2014-31* (2014) 246 p.

94. Swerling, P., "First-Order Error Propagation in a Stagewise Smoothing Procedure for Satellite Observations." Rand Corporation, *Research Memorandum RM-2329* (1959) 30 p.

95. Kalman, R. E. "A New Approach to Linear Filtering and Prediction Problems." Transactions of ASME – Journal of Basic Engineering, Vol. 82, Series D (March 1960) pp. 35-45.

96. Sorenson, H. W., "Least-Squares Estimation: from Gauss to Kalman." *IEEE Spectrum*, Vol. 7, Issue 7 (1970) pp. 63-68.

97. Maybeck, P. S., *Stochastic Models, Estimation, and Control. Volume I*. Academic Press (1979).

98. Welch, G. and G. Bishop, "An Introduction to the Kalman Filter." Department of Computer Science, University of North Carolina at Chapel Hill, *Technical Report TR 95-041* (2006) 16 p.

99. Goddard, J. S., "Pose and Motion Estimation from Vision Using Dual Quaternion-Based Extended Kalman Filtering." Ph.D. Dissertation, University of Tennessee, Knoxville (1997) 179 p.

100. Groves, P. D., *Principles of GNSS, Inertial, and Multisensor Integrated Navigation Systems*. Second Edition, Atech House (2008).

101. Brown, R. G. and P. Y. C. Hwang, *Introduction to Random Signals and Applied Kalman Filtering*. Fourth Edition, John Wiley and Sons, Inc. (2012).

102. Jones, R. H., "Maximum Likelihood Fitting of ARMA Models to Time Series with Missing Observations." *Technometrics*, Vol. 223, No. 3 (1980) pp. 379-395.

    Cipra, T. and R. Romera, "Kalman Filter with Outliers and Missing Observations." *Sociedad de Estadística e Investigación Operativa Test*, Vol. 6, No. 2 (1997) pp 379-395.

104. Smyth, A. and M. Wu, "Multi-rate Kalman Filtering for the Data Fusion of Displacement and Acceleration Response Measurements in Dynamic System Monitoring." *Mechanical Systems and Signal Processing*, Vol. 21, Issue 2 (2007) pp. 706-723.

105. Rauch, H. E., Tung, F., and C. T. Striebel, "Maximum Likelihood Estimates of Linear Dynamic Systems." *AIAA Journal*, Vol. 3., No. 8 (1965) pp. 1445-1450

106. Grewal, M. S. and A. P. Andrews, *Kalman Filtering: Theory and Practice Using MATLAB®*. Fourth Edition. John Wiley & Sons. Inc. (2015).

107. Meditch, J. S., *Stochastic Optimal Linear Estimation and Control*, New York: McGraw-Hill, 1969.

108. Aslan, S., Hemodynamic Model Inversion by Iterative Extended Kalman Smoother." Chapter 10, *Handbook of Neural Computation*, Eds. Samui, P., Roy, S. S., and V. E. Balas (2017) pp. 181-199.

109. Wie, B., *Space Vehicle Dynamics and Control*. 2nd Edition. American Institute of Aeronautics and Astronautics, Reston, VA (2008).

110. Hol, J. D., "Sensor Fusion and Calibration of Inertial Sensors, Vision, Ultra-Wideband and GPS." *Dissertation No. 1368*, Linkoping University, Linkoping, Sweden (2011) 143 p.

111. Kok, M., Hol, J. D., and T. B. Schön, "Using Inertial Sensors for Position and Orientation Estimation." *Foundations and Trends in Signal Processing*, Vol. 11, No. 1-2 (2017) pp. 1-153.

112. Titterton, D. H. and J. L. Weston, *Strapdown Inertial Navigation Technology*, 2nd Edition. The Institution of Electrical Engineers (2004).

113. Allan, D. W., "Statistics of Atomic Frequency Standards." *Proceeding of the IEEE*, Vol. 54, No. 2 (1966) pp. 221-230.

114. IEEE Std 952-1997 (R2008). *IEEE Standard Specification Format Guide and Test Procedure for Single-Axis Interferometric Fiber Optic Gyros*.

115. Tehrani, M. M., "Ring Laser Gyro Data Analysis with Cluster Sampling Technique." *Proceedings of SPIE*, Vol. 412 (1983) pp. 207-220.

116. El-Sheimy, N., Hou, H., and X. Niu, "Analysis and Modeling of Inertial Sensors Using Allan Variance." *IEEE Transactions on Instrumentation and Measurement*, Vol. 57, No. 1 (2008) pp. 140-149.